FLOW PATTERNS IN A CONFINED PLASMA JET

by

Finis Ewing Carleton

A dissertation submitted in partial fulfillment
of the requirements for the degree of
Doctor of Philosophy in
The University of Michigan
1970

Doctoral Committee:

Associate Professor Robert H. Kadlec, Chairman
Assistant Professor Dale E. Briggs
Professor Walter R. Debler
Associate Professor Joe D. Goddard
Professor G. Brymer Williams

elogio
UMA 1089

ACKNOWLEDGEMENTS

The author wishes to express his gratitude and appreciation to those persons who have contributed to this investigation.

The guidance and criticism offered by Professor Robert H. Kadlec, chairman of the doctoral committee, was particularly appreciated. The interest and friendship of Professor G. B. Williams and the assistance of the other members of the doctoral committee, Professors D. E. Briggs, W. R. Debler, and J. D. Goddard are gratefully acknowledged. Professors J. O. Wilkes and W. O. Winer also provided significant advice while they served on the doctoral committee.

The shop personnel of the Department of Chemical and Metallurgical Engineering, Messrs. C. Bolen, E. Darling, E. Muehlig, R. Reid, and P. Severn, were most cooperative and helpful. In particular, the author expresses his sincere gratitude to Messrs. D. Connell and J. Wurster, whose patience, suggestions, and aid made possible the experimental portion of this investigation.

Special thanks are due to the other members of the plasma laboratory, whose friendship and assistance were an invaluable contribution.

The author is also grateful for the early interest and stimulation provided by Professors John J. McKetta and Robert S. Schecter of the University of Texas.

Finally, the author is indebted to his parents for their encouragement, to his wife for her patience, support, encouragement, and cooperation in the preparation of this manuscript, and to the National Science Foundation for their financial assistance.

TABLE OF CONTENTS

TABLE OF CONTENTS (Continued)

TABLE OF CONTENTS (Continued)

LIST OF TABLES

LIST OF FIGURES

LIST OF FIGURES (Continued)

LIST OF FIGURES (Continued)

LIST OF FIGURES (Continued)

ABSTRACT

Flow patterns in a confined argon plasma jet at atmospheric pressure were investigated experimentally. Velocity and temperature profiles in the plasma jet were determined in order to establish the flow patterns as a function of the operating variables of the system. The jet was studied downstream from a direct current, constricted arc plasma generator. The effects of argon flow rate and input power to the plasma generator were investigated. The confining chamber was an uncooled quartz tube of diameter 7.5 times that of the plasma generator nozzle.

The argon flow rate was varied between 11 and 45 gm/min and the input power between 4.6 and 10.2 kw. Three distinct types of jet-laminar, transitional, and turbulent-could be obtained. At a fixed power level they occurred in the above sequence with increasing argon flow rate. To measure jet velocities directly without disturbing the flow a trace gas technique was attempted. Passage of krypton through the plasma jet could be detected spectrographically, but no meaningful information could be resolved from the data that was obtained.

Velocity profiles in the plasma jet were determined indirectly from profiles of impact pressure and temperature. Impact pressures were measured with a water-cooled probe, while temperatures were calculated from the intensity of the plasma radiation which was measured spectrographically. The plasma

proved to be in local thermodynamic equilibrium so that the electron temperature corresponding to the continuum intensity at 5330 $\mathring{A}$ was used as the plasma temperature. To calculate the plasma velocity from the impact pressure and temperature, a model was developed which considered both viscous and heat transfer effects near the stagnation point of the probe. The measured impact pressure P_o is related to the free stream pressure P_∞ and free stream plasma velocity U by

$$P_o - P_\infty = \frac{\rho_\infty U^2}{2} + \frac{\rho_\infty U^4}{8\gamma P_\infty} + \frac{2\bar{\mu}U}{R\left(1+\frac{0.5576}{\sqrt{Re}}\right)} \quad ,$$

in which R is the radius of the probe, and physical properties in the Bernoulli and compressibility terms are evaluated at the free stream temperature while those in the viscous term are evaluated at the temperature corresponding to the mean of the free stream and wall enthalpies. The model was extended to calculate stagnation point heat transfer coefficients, and the predicted values agreed with experimental values obtained in an earlier study.

Temperature and velocity profiles were obtained in both a transitional and a turbulent plasma jet at an intermediate power level (approximately 7.5 kw). A maximum velocity of 18820 cm/sec and a maximum temperature of 10920 ^oK were observed in this particular transitional jet; in the turbulent jet, the maximum

velocity was 22650 cm/sec and the maximum temperature was 11140 ^{o}K. Velocities and temperatures at a given position were greater in the turbulent jet than in the transitional jet. In each jet, the centerline velocity varied linearly with the centerline temperature. Integration of the initial velocity profile in each jet yielded a flow rate which agreed with the metered argon flow rate within 5%.

The effect of input power level on the centerline temperatures and velocities and on the operating characteristics of the plasma generator was demonstrated for the three types of plasma jet. The power level ranged from 4.6 to 10.2 kw., with three levels investigated for each mode of operation. In each jet the centerline velocity again varied linearly with the centerline temperature, which was correlated with the operating characteristics of the plasma generator.

Bulk Reynolds numbers based on the diameter of the plasma generator nozzle were calculated for the various operating conditions and exhibited a limiting range for each mode of operation. The values for the laminar plasma jets were below 160; those for the transitional jets were in the range of 170 to 210; the values for the turbulent jets were above 240.

1. INTRODUCTION

The recently acquired prominence of plasma technology has created a need for analysis of the flow processes in high temperature plasma jets. The unique interest in these jets arises from their extreme temperatures, which greatly exceed those attainable in a conventional flame by combustion of a fuel-oxidizer mixture. This source of extreme temperatures could be a valuable tool to the chemical engineer for effecting highly endothermic chemical reactions.

To characterize flow processes in a plasma jet, it is necessary to know the spatial distribution of velocity and temperature as a function of the gas flow and arc heating parameters. If the results can then be generalized, the information will greatly contribute towards solving problems encountered in chemical processing with arc jets.

This thesis is concerned with investigating experimentally the flow patterns in a confined plasma jet at atmospheric pressure. More specifically, the goals of this study were:

1. To establish flow patterns as a function of the operating variables of the system.
2. To measure velocity and temperature profiles in the plasma jet.
3. To compare the experimental data for the plasma jet with cold flow profiles to determine how arc heating and the associated extreme gradients of temperature influence the flow fields.

As a necessary part of the work, experimental techniques for the measurement of plasma velocities and temperatures had to be established and the relationships between measured and desired quantities ascertained.

The plasma jet was investigated after it emerged from the nozzle of the direct-current, constricted arc plasma generator designed and built for this study. Operation of the generator and flow patterns in the jet depend on the nature and properties of the plasma gas employed, the geometric configuration of the arc region and the jet confining chamber, the flow rate and flow orientation of the plasma gas, and the input power to the generator. During the main phases of this work, the only independent parameters which were allowed to vary were the gas flow rate and input power level. The variety of phenomena occurring in the arc region were not of primary concern although the generator voltage and current were used in correlating experimental results. The net effect of arc heating was the production of an ionized gas stream. Argon was used as the plasma gas. It was supplied axially to the arc region so as not to complicate the flow geometry. The jet was confined since this sytem would be of more interest in future applications to plasma chemical reactors.

To measure jet velocities directly without disturbing the flow, a trace gas technique was proposed and evaluated.

A small amount of tracer gas was injected cocurrently into the main stream argon just upstream of the arc. Time variations of the trace gas concentration were observed spectroscopically at various positions in the plasma jet as the trace gas passed through, in an attempt to measure the time delays incurred in passing from one position to another. No previous experience with this technique has been reported in the literature. Velocities in the jet were determined indirectly from point measurements of impact pressures with a water-cooled probe. These data and the corresponding temperatures which were measured spectrographically permit calculation of velocities. This technique has been used previously as will be discussed later, but without correction for the effect of the boundary layer around the probe. Such a correction was derived and applied in this investigation. The boundary layer model for the cool probe in a hot ionized gas considers both viscous and heat transfer effects. For purposes of verification the model was extended and applied to resolve data on stagnation point heat transfer coefficients in a plasma which were obtained with a water-cooled probe during an earlier investigation (15). Heat transfer due to ion diffusion-recombination was included. In establishing a spectrographic method of temperature measurement, a check of the thermal condition of the plasma

was made to determine if equilibrium conditions prevailed. The waveforms of voltage and current fluctuations were analyzed as an aid in characterizing flow patterns.

Before presenting and discussing the results of this study, background information on electric arc phenomena and plasma generators is presented, previous related work is surveyed, pertinent theory is developed or explained, and the experimental apparatus and operating procedures are described.

2. BACKGROUND

A plasma jet is generated by physical rather than chemical methods, and can be achieved by combining the high temperature characteristics of a d.c. electric arc with an independent steady-state gas flow to create the continuous, high velocity jet flame at an extremely high temperature. Although plasma jet technology itself is a relatively new field, the characteristics of the arc have been under investigation for many years.

The electric arc is a self-sustained discharge of electricity between two separated electrodes through a gas or vapor capable of ionization. In the discharge, there is a relatively high degree of breakdown of the individual atoms or molecules into free electrons and positive ions. At atmospheric pressures or higher the arc is characterized by a well defined boundary, within which the temperature is extremely high (higher than that of either electrode) so as to sustain ionization of the gas or vapor, and from which bright visible radiation is emitted. The predominant mechanism of energy transfer in the arc is elastic collisions between heavy particles and electrons, and as a result the hot ionized gas - the arc plasma - is in approximate thermodynamic equilibrium (51). This concept will be

discussed in more detail in a later chapter.

The arc can be either free or confined. The free or unconfined arc has no solid boundaries in close proximity to central part of the arc (termed the arc column) so that the gas is not restrained to remain in the arc path. The arc is then subject to free convection currents and recirculation phenomena. Usually, there is no externally imposed flow. In contrast, the column of the confined arc is physically surrounded by solid boundaries and usually subjected to forced convection through an externally imposed gas flow. Such arcs exhibit accurate positioning of the arc column and reduced column fluctuations (51). This is achieved by one of several possible means of stabilization to be explained below. Confinement of the arc increases the current density, the voltage gradient, and the temperature in the column. This results in an increase in energy transferred to the gas. A confined arc is generally employed in plasma jet generating equipment.

Several methods exist for stabilizing the position of the arc column in the confining channel of a plasma generator. The arc can be wall stabilized by making it pass through confining walls so narrow that the arc fills the entire space. Liquid stabilization occurs when the arc passes through the vortex core of a rotating or tangentially flowing liquid.

If the arc is confined and rotated within an externally imposed magnetic field, field stabilization results. To study flow patterns in a plasma jet, gas or convection stabilization is the most desirable means of arc stabilization. This is achieved by either swirling gas at high speed around the arc or passing gas at high speed along the arc. If the gas is introduced tangentially into the arc region producing a vortex flow, the radial pressure gradient combined with the low density of the high temperature arc column achieves positioning of the column along the axis of the confining channel. If the gas is introduced parallel to the arc column, a cool gas sheath surrounds the column and positions it along the channel axis (51).

Many possible configurations have been devised for incorporating gas stabilization into the plasma generator itself. The geometry of any configuration and the sense of the gas flow have a strong influence on the operation of the generator. For this study a constricted nozzle configuration with gas sheath stabilization was chosen. Figure 1 is a general diagram of this configuration. The "stick" electrode is the cathode (negative electrode) and in most cases its position is changeable. The geometry is such that the gas flows as a hollow sheath into the narrow nozzle channel with the axial velocity of the gas in this passage being greater as the radial distance from the

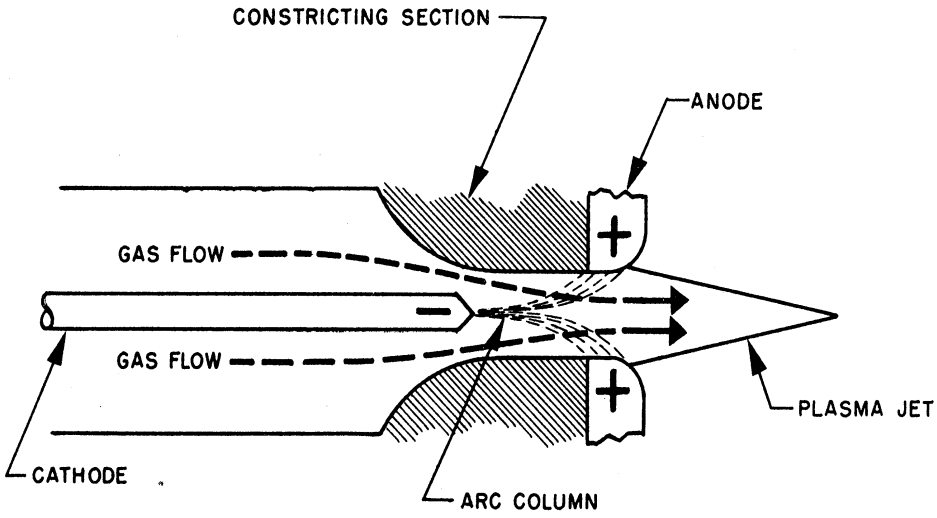

FIG. I. CONSTRICTED ARC PLASMA GENERATOR CONFIGURATION

axis increases. A low velocity core exists beyond the cathode tip and extends into the channel (10). The arc is positioned within this core and the momentum of the gas stream stretches the arc as the arc transfers heat to the gas. The exit section of the nozzle is the anode, where the arc terminates. A portion of the nozzle is insulated from both the anode and the cathode, and forms the constricting section. In many cases the exit section of the nozzle is made diverging, so that the constricting section corresponds to the nozzle throat. For the current study, however, the exit section was cylindrical, so as to form a tube in conjunction with the constrictor. This kept the geometry simple. As noted previously, the gas was fed to the nozzle without any swirling motion to keep from complicating the flow patterns. It must also be noted that the anode section of the nozzle was sufficiently long so as to contain the arc within its length — that is, no current filaments extended past the nozzle exit. The luminous, high velocity gas stream emerging from the nozzle is the plasma jet. Although the jet overall is electrically neutral, the gas itself is still partially ionized so that the jet would be affected when in a region of imposed electric and/or magnetic fields. For this particular study the plasma jet was confined in a field free region at atmospheric pressure. As stated previously, argon was used as the plasma gas. It

was selected because it is inert, it has a reasonable ionization potential, it results in a stable operation, and because its thermodynamic, transport, and spectral properties are known. The flow patterns occurring in the jet under different operating conditions of input power and flow rate are the subject of this investigation.

To complete the discussion, it is worthwhile to mention some of the operating characteristics of a constricted arc plasma generator. Once the configuration and geometry of the plasma generator, the sense of the gas flow, and the specific gas to be used have been established, operation depends on the distance of the cathode tip from the nozzle inlet, the gas flow rate, and the current of the arc. The voltage of the arc cannot be controlled or specified, but depends on the three independent variables cited above. Usually, the electrode separation is not varied during operation, so that only two independent parameters remain. In general, the arc voltage will increase with increasing gas flow rate at a fixed arc current, and can either increase or decrease with an increase in current at a fixed flow rate. The arc voltage increases with electrode separation (32). Since the efficiency of energy transfer to the gas increases with increasing voltage, it would seem desirable to operate the generator at as large an electrode separation and as high a gas flow rate as possible. However, increased separation and/or gas flow rate can affect

the stability of the arc, so that desirable operating conditions cannot be predicted and must be obtained through actual operation of the generator.

3. SURVEY OF PREVIOUS WORK

An abundance of information pertaining to plasmas and plasma jets has appeared in the technical literature in the last few years. The majority of studies dealing with plasma flow problems have been done in connection with missile re-entry simulation or magnetohydrodynamic accelerator and thrustor development, and have no direct bearing on this investigation. The works which are reviewed here were, unless noted, concerned with field-free, subsonic, plasmas or plasma jets. Strong emphasis is placed on the techniques employed.

Reed (44) and Kimura and Kanzawa (36) have determined profiles of streaming velocities in unconfined electric arcs. Reed measured the distribution of impact pressures at the anode by employing a moveable flat plate anode with a built-in pressure tap. Correcting the measured impact pressures for the pressure generated by the arc's self-magnetic field, the streaming pressures and the corresponding temperatures obtained spectroscopically were used to calculate velocity profiles at several current levels. Kimura and Kanzawa measured the drag on a small square plate swept rapidly through the arc normal to the arc axis. The streaming velocity was then calculated from the net drag at any point. In computing the drag coefficients, the Reynolds number was evaluated at the arithmetic mean of the plasma temperature, measured spectroscopically, and the

estimated plate temperature.

By measuring the thrust of an unconfined plasma jet against a cantilever, Kasahara et al. (34) determined average jet velocities as a function of argon flow rate and input power. Gottschlich et al. (25) calculated the velocity profiles in a laminar plasma jet from the temperature profiles using a simplified form of the energy equation. The temperature profiles, which were determined spectroscopically, were graphically differentiated to obtain first and second partial derivatives with respect to the spatial coordinates, and the velocities calculated from the appropriate combinations of these derivatives and transport properties. Incropera and Leppert (31) studied flow transitions in a free plasma jet as a function of argon flow rate, input power, and nozzle exit diameter by measuring the jet noise level (accoustic power) and the jet length. Results were correlated using a Reynolds number based on bulk jet properties. The bulk temperature was determined from the average jet enthalpy, which in turn had been obtained from an overall energy balance.

Freeman et al. (22) measured the propagation times between two axial positions of spark induced luminous fluctuations in a confined, vortex stabilized plasma jet. By comparing signals from photomultiplier tubes located at the two positions, two types of fluctuations were observed — one apparently traveling

with the speed of the jet, thought to be due to temperature fluctuations, and the other traveling much faster, thought to be due to pressure fluctuations. The intermingling of these two fluctuations prevented resolution of the gas velocity. In a similar manner, Beasley et al. (5) used photomultiplier tubes to measure propagation times between axial positions of luminous fluctuations induced in a supersonic plasma jet by discharging a small capacitor across the generator electrodes. Bulk velocities determined as a function of arc current at fixed flow rates agreed well with computed velocities based on heating and expanding the gas, although in some cases, arc instabilities due to the capacitor discharge were observed. The technique was checked by comparing cold flow measurements for the induced spark with conventional impact pressure measurements, and agreement was found to be good. Jordan and King (33) in conjunction with an investigation of arc mechanisms in a plasma generator studied natural fluctuations in an unconfined plasma jet using a high speed streak camera. Mean velocities deduced from photographs of the jet were somewhat greater than those calculated by an energy balance. Merrifield and Esker (40) also used photomultiplier tubes to measure propagation times between two axial positions of random light fluctuations in a vortex stabilized supersonic plasma jet. The velocities

obtained exhibited a frequency dependence, and these propagation velocities were higher than average exhaust velocities determined from specific impulse measurements. The exact relationship between propagation velocity and the stream velocity could not be resolved.

Cabannes et al. (11) working with an unconfined plasma jet measured the propagation time between two axial positions of a weak light pulse, and the axial distribution of impact pressure with a cooled pitot tube. The calculated propagation velocity and the impact pressure were used to calculate the density and the density in turn used to determine the temperature along the axis. No correction was made for the boundary layer effects around the pitot tube. Cabannes, Joubert, and Sy (12) observed visually the laminar to turbulent transition in an unconfined plasma jet, and calculated the velocity profile in the laminar case from measured distributions of temperature and impact pressure. No consideration was given to the cool boundary layer around the pitot tube. Detailed studies have been made by Grey et al. (26, 27, 48, 49) of unconfined mixing of coolant streams with both laminar and turbulent plasma jets. Impact pressures and temperatures were both measured with a water cooled sampling probe, and these data used to obtain velocity profiles. Again, the calculation did not take into account the boundary layer around the cooled probe. The

investigations of Smith (52) and Chludzinski (15) have raised some extreme doubts about the validity of probe techniques for temperature measurements in plasmas. The results of Chludzinski who studied heat transfer to solids immersed in plasmas generated by induction heating will be discussed later. Smith studied confined mixing of a coolant gas with a turbulent plasma jet. Temperature profiles were obtained spectroscopically, and impact pressures were measured with a water cooled probe. In calculating the velocity profiles, an attempt was made to correct for heat transfer through the cool boundary layer around the probe, but the correction actually over-compensated for the boundary layer effects. Sprengel (53) used the probe techniques of Grey to obtain velocity profiles in a plasma jet.

Finally, Whitman and Barkan (55) designed an uncooled, rapid response probe for measuring impact pressures in an unconfined, high velocity (M near 1.0) arc plasma. The probe was swept through the blown arc, and the expendable probe tip allowed to ablate. True impact pressures were evaluated from the transient response of the pressure transducer employed in conjunction with the probe. The necessity for a viscous correction in low velocity plasma flows ($M < 0.1$) was noted, although no correction was made in calculating the distribution of Mach numbers in the arc.

4. THEORY

The theory of stagnation streamline flow, stagnation point heat transfer, and thermal radiation for plasmas will be developed and discussed in order to relate the measureable quantities of impact pressure and radiation intensity to the desired distributions of velocity and temperature in the plasma jet. Stagnation point heat transfer is considered to justify the method of solution employed for stagnation streamline flow, with the relationship obtained being compared to previously reported experimental data. The assumptions involved in each specific development are introduced as necessary.

Stagnation Streamline Flow

For isentropic, inviscid deceleration of an incompressible fluid along a stagnation streamline, the stagnation pressure P_o as measured with an impact (Pitot) tube is given in terms of the free stream quantities — static pressure P_∞, density ρ_∞, and velocity U — by the Bernoulli equation

$$P_o = P_\infty + \frac{\rho_\infty U^2}{2} \quad . \qquad (4\text{-}1)$$

If the fluid is compressible, the equation for isentropic, inviscid deceleration becomes

$$P_o = P_\infty \left(1 + \frac{\gamma-1}{2} M_\infty^2\right)^{\frac{\gamma-1}{\gamma}} \quad , \qquad (4\text{-}2)$$

where M_∞ is the free stream Mach number and γ is the ratio of specific heats, C_p/C_v.

For viscous fluids flowing at Reynolds numbers above 100 (the characteristic length chosen to be the radius of the impact tube), the viscous forces acting on the fluid are very small in comparison to the inertia forces and the above equations are valid. As the Reynolds number is decreased below 100, however, the measured impact pressure departs from the true stagnation pressure based on isentropic, inviscid deceleration, and it is no longer possible to ignore the effects of viscosity. This departure of the impact pressure from the stagnation pressure is known as the Barker effect (3), and has been observed experimentally (30, 38, 46, 47). It shows itself in the form of an additional pressure which can be calculated for simple geometries (i.e. cylinders, spheres), so that the measured impact pressure is greater than the ideal stagnation pressure.

Since high temperature gas flows in general and plasma jets in particular characteristically involve low Reynolds numbers (due to low densities and high viscosities), the viscous effect must be included in any relationship between impact pressure and free stream velocity. For a water-cooled impact probe immersed in a plasma jet so that the probe axis

is parallel to the axis of the jet, this relationship will be deduced. The stagnation streamline is divided into two regions. The pressure recovery in the region farthest from the stagnation point, which extends to free stream conditions, is considered to occur as in isentropic, inviscid, compressible flow. In the region nearest the probe, the pressure recovery is considered to occur under conditions of viscous, incompressible, laminar flow. Although there is a temperature gradient across the boundary region, a constant mean value of viscosity is assumed in this layer to obtain a solution and the effect of variable viscosity compensated for in a manner to be discussed later. Solutions for the two regions are matched at the point where the regions meet. The probe is assumed to be spherical half body, and a cylindrical coordinate system is used, with the z direction parallel to the axis of the probe and hence, the stagnation streamline. The r direction is normal to stagnation streamline, as shown below.

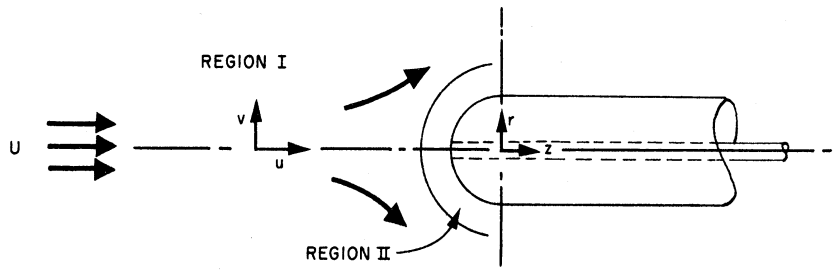

FIG. 2. STAGNATION STREAMLINE FLOW NEAR AN IMPACT PROBE

Region I (Inviscid, Compressible)

Along the stagnation streamline, the equation of motion in the z direction reduces to ($v = 0, \frac{\partial}{\partial r} = 0$)

$$\rho u \frac{\partial u}{\partial z} = - \frac{\partial P}{\partial z} \quad . \qquad (4\text{-}3)$$

Integrating equation (4-3) with respect to z, from $z = -\infty$ to $z = -\delta$,

$$U^2 - u_{-\delta}^2 = 2 \int_{-\infty}^{-\delta} \frac{dP}{\rho} \quad . \qquad (4\text{-}4)$$

For isentropic compressible flow,

$$\frac{1}{\rho} = \left(\frac{\text{constant}}{P} \right)^{\frac{1}{\gamma}} \quad , \qquad (4\text{-}5)$$

and the right hand side of equation (4-4) becomes

$$U^2 - u_{-\delta}^2 = \frac{2\gamma}{\gamma - 1} \left(\frac{P_{-\delta}}{\rho_{-\delta}} - \frac{P_\infty}{\rho_\infty} \right) \quad . \qquad (4\text{-}6)$$

(Note that ∞ has been used instead of $-\infty$.)

For use later, equation (4-6) is rearranged to give

$$P_{-\delta} + \frac{\rho_{-\delta} u_{-\delta}^2}{2} = \frac{\rho_{-\delta} U^2}{2} + \frac{\gamma}{\gamma - 1} P_\infty \left(\frac{\rho_{-\delta}}{\rho_\infty} \right) - \frac{P_{-\delta}}{\gamma - 1} \quad . \qquad (4\text{-}7)$$

Were there no viscous boundary layer, $u_{-\delta}$ would be 0 and the pressure $P_{-\delta}$ and density $\rho_{-\delta}$ would correspond to the pressure and density at stagnation conditions. Thus, the left hand side of equation (4-7) is equal to the ideal stagnation pressure P_o^*. This can be easily verified. For isentropic flow (37)

$$\frac{\rho_{-\delta}}{\rho_\infty} = \left(1 + \frac{\gamma-1}{2} M^2\right)^{\frac{1}{\gamma-1}} \quad , \qquad (4\text{-}8)$$

and

$$\frac{P_{-\delta}}{P_\infty} = \left(1 + \frac{\gamma-1}{2} M^2\right)^{\frac{\gamma}{\gamma-1}} \quad . \qquad (4\text{-}9)$$

Substituting these expressions into the right hand side of equation (4-7) and rearranging,

$$P_{-\delta} + \frac{\rho_{-\delta} u_{-\delta}^2}{2} = \left(\frac{\rho_\infty U^2}{2} + \frac{\gamma P_\infty}{\gamma-1}\right)\left(1 + \frac{\gamma-1}{2} M^2\right) - \frac{P_\infty}{\gamma-1}\left(1 + \frac{\gamma-1}{2} M^2\right)^{\frac{\gamma}{\gamma-1}} \quad . \qquad (4\text{-}10)$$

Noting that

$$\frac{\rho_\infty U^2}{2} = \frac{\gamma P_\infty M^2}{2} \quad , \qquad (4\text{-}11)$$

equation (4-10) can be simplified to

$$P_{-\delta} + \frac{\rho_{-\delta} u_{-\delta}^2}{2} = \frac{P_\infty}{\gamma-1}\left[\gamma\left(1 + \frac{\gamma-1}{2} M^2\right)\left(1 + \frac{\gamma-1}{2} M^2\right)^{\frac{1}{\gamma-1}} - \left(1 + \frac{\gamma-1}{2} M^2\right)^{\frac{\gamma}{\gamma-1}}\right] \quad , \qquad (4\text{-}12)$$

and finally

$$P_{-\delta} + \frac{\rho_\delta u_{-\delta}^2}{2} = P_\infty \left(1 + \frac{\gamma-1}{2} M^2\right)^{\frac{\gamma}{\gamma-1}} \quad . \tag{4-13}$$

The right hand side of equation (4-13) is the ideal stagnation pressure, as postulated above. Applying the binomial expansion and neglecting powers higher than M^4,

$$P_{-\delta} + \frac{\rho_\delta u_{-\delta}^2}{2} = P_\infty + \frac{\gamma M^2}{2} + \frac{\gamma M^4}{8} \quad , \tag{4-14}$$

and thus

$$P_{-\delta} + \frac{\rho_\delta u_{-\delta}^2}{2} = P_\infty + \frac{\rho_\infty U^2}{2} + \frac{\rho_\infty U^4}{8 \gamma P_\infty} \quad . \tag{4-15}$$

Region II (Viscous, Incompressible, Laminar)

On the stagnation streamline in the boundary layer, the equation of motion in the z direction reduces to ($v = 0, \frac{\partial}{\partial r} = 0$)

$$\rho u \frac{\partial u}{\partial z} = -\frac{\partial P}{\partial z} + \mu \frac{\partial^2 u}{\partial z^2} \quad , \tag{4-16}$$

making the assumption in the boundary layer that $\frac{\partial^2 u}{\partial r^2} << \frac{\partial^2 u}{\partial z^2}$. Since the flow has been assumed incompressible, the density is equal to $\rho_{-\delta}$. The viscosity varies through the boundary layer because of the temperature gradient. To integrate the

viscous term, the temperature distribution in the boundary layer must be known or a constant mean value $\bar{\mu}$ must be assumed. The temperature distribution is not known so that the latter approach is taken. Selection of the mean value will be discussed later. With these restrictions, equation (4-16) is integrated with respect to z, from $z = -\delta$ to $z = -R$ to yield

$$-\rho_{-\delta} u_{-\delta}^2 = P_{-\delta} - P_o - \bar{\mu} \frac{\partial u}{\partial z}\Big|_{z=-\delta} \quad , \qquad (4\text{-}17)$$

where P_o is the measured impact pressure. At $z = -R$, $u = 0$ and the derivative $\frac{\partial u}{\partial z}$ vanishes by the continuity equation. Rearranging,

$$P_{-\delta} + \frac{\rho_{-\delta} u_{-\delta}^2}{2} = P_o + \bar{\mu} \frac{\partial u}{\partial z}\Big|_{z=-\delta} \quad . \qquad (4\text{-}18)$$

The quantity $\frac{\partial u}{\partial z}\Big|_{z=-\delta}$ is evaluated for an ideal potential flow field around the boundary layer surface surrounding the probe, since the flow outside the boundary layer was treated as inviscid. The potential function ϕ for a uniform free stream flow in the +z direction around a spherical half body oriented so that the stagnation streamline is the -z coordinate axis is given by (54)

$$\phi = -Uz + \frac{Ua^2}{\sqrt{r^2+z^2}} \quad , \qquad (4\text{-}19)$$

where U is the free stream velocity and a is the radius of curvature of the body. It follows then that

$$\frac{\partial u}{\partial z} = -\frac{\partial^2 \Phi}{\partial z^2} \quad , \qquad (4\text{-}20)$$

and hence

$$\frac{\partial u}{\partial z} = \frac{U a^2}{(r^2+z^2)^{\frac{3}{2}}} \left[1 - \frac{3z^2}{(r^2+z^2)}\right] \quad . \qquad (4\text{-}21)$$

For the stagnation streamline, r = 0 and the radius of curvature of the boundary layer surface is δ. The desired term is

$$\frac{\partial u}{\partial z}\Big|_{z=-\delta} = -\frac{2U}{\delta} \quad . \qquad (4\text{-}22)$$

Substituting into equation (4-18),

$$P_{-\delta} + \frac{\rho_{-\delta} u_{-\delta}^2}{2} = P_0 - \frac{2\bar{\nu} U}{\delta} \quad . \qquad (4\text{-}23)$$

To match the solutions for the two regions, the left hand side of the above equation is replaced with its equivalent obtained in equation (4-15), and after rearrangement, becomes

$$P_0 - P_\infty = \frac{\rho_\infty U^2}{2} + \frac{\rho_\infty^2 U^4}{8\gamma P_\infty} + \frac{2\bar{\nu} U}{\delta} \quad . \qquad (4\text{-}24)$$

The last term in equation (4-24) requires further consideration. The radius of curvature of the boundary layer surface on the stagnation streamline, δ , can be written

$$\delta = R + \delta^* \quad , \qquad (4\text{-}25)$$

where R is the radius of curvature of the spherical half body (the radius of the probe since the probe tip is nearly hemispherical) and δ^*, the displacement thickness. The displacement thickness for flow around an object indicates the amount that the streamlines for ideal flow are shifted due to the formation of a boundary layer. For flow around an axisymmetric body of revolution the displacement thickness determined in Homann's solution of the momentum equation near the stagnation point (29) is

$$\delta^* = 0.5576\sqrt{\frac{\nu}{\rho\beta}} \quad , \qquad (4\text{-}26)$$

where

$$\beta = \frac{\partial v}{\partial r} \quad . \qquad (4\text{-}27)$$

β is evaluated at the stagnation point in a potential flow field around the body. Then,

$$\beta = -\frac{\partial^2 \Phi}{\partial r^2} \quad , \qquad (4\text{-}28)$$

and at z = -R, r = 0, becomes

$$\beta = \frac{U}{R} \quad . \qquad (4\text{-}29)$$

Substituting into equation (4-26) and rearranging,

$$\delta^* = 0.5576\sqrt{\frac{R\mu}{\rho U}} \quad , \qquad (4\text{-}30)$$

or

$$\delta^* = \frac{0.5576\,R}{\sqrt{Re}} \quad . \qquad (4\text{-}31)$$

In equation (4-31) Re is the Reynolds number for flow around the probe. Thus, equation (4-25) can be written

$$\delta = R\left(1 + \frac{0.5576}{\sqrt{Re}}\right) \quad . \qquad (4\text{-}32)$$

Replacing δ in equation (4-24)

$$P_o - P_\infty = \frac{\rho_\infty U^2}{2} + \frac{\rho_\infty^2 U^4}{8\gamma P_\infty} + \frac{2\bar{\mu} U}{R\left(1 + \frac{0.5576}{\sqrt{Re}}\right)} \quad . \qquad (4\text{-}33)$$

Therefore, the difference between the measured impact pressure and the free stream pressure, $P_o - P_\infty$, for a plasma flowing around a hemispherical tipped cylindrical body is expressed by a Bernoulli term, a compressibility term, and a viscous term.

Physical properties in the first two terms are evaluated at free stream conditions of temperature and pressure. In order to select $\bar{\mu}$ and evaluate Re in the third term, a characteristic temperature of the boundary layer is chosen. This characteristic or reference temperature is a temperature at which constant property results will closely approximate true variable property behavior. The appropriate values of $\bar{\mu}$ and Re are those corresponding to the reference temperature. Although no prior basis for the use of this technique in a plasma boundary layer has been established, it is a method which does compensate for the temperature gradient near the probe (35). Further discussion and justification is deferred until the following section where heat transfer is considered. In this particular application, the characteristic temperature selected is the temperature corresponding to the arithmetic mean of the wall and free stream enthalpies (21). It will become apparent later that this reference temperature is primarily a function of the free stream temperature since the probe is water cooled. Hence, if T_∞ and (P_0-P_∞) are known at any point in a plasma flow field, a reference temperature can be obtained so that all physical properties in equation (4-33) can be evaluated. The equation is then implicit in U and can be solved by an iterative method. Chambre and Smith in a similar manner developed an expression for a high velocity, low density gas stream which differs somewhat from equation (4-33) in the

viscous term because flow around a spherical body was assumed (14). The effect of the viscous term in equation (4-33) on the difference between the measured impact pressure and the free stream pressure, neglecting the compressibility term, is shown in dimensionless form as a function of Reynolds number in Figure 3. As postulated, it results in a measured impact pressure increased over the ideal stagnation pressure.

Stagnation Point Heat Transfer

The validity of using the reference temperature technique in plasma flow calculations is established by considering heat transfer to an object immersed in a plasma stream and applying the resulting theoretical expression to previously unresolved experimental data. In order to determine heat transfer rates at the stagnation point of the object, the equations describing the flow in the boundary layer surrounding the object must be analyzed. As before, the object is taken to be a spherical half body and a cylindrical coordinate system employed. Although use of this system is different than choosing one based on the distance along the surface of the body from the stagnation point and the distance normal to the surface, the results will be the same since the equations in either system are identical in the immediate vicinity of the stagnation streamline. In the boundary layer, it is assumed that the ion-electron-

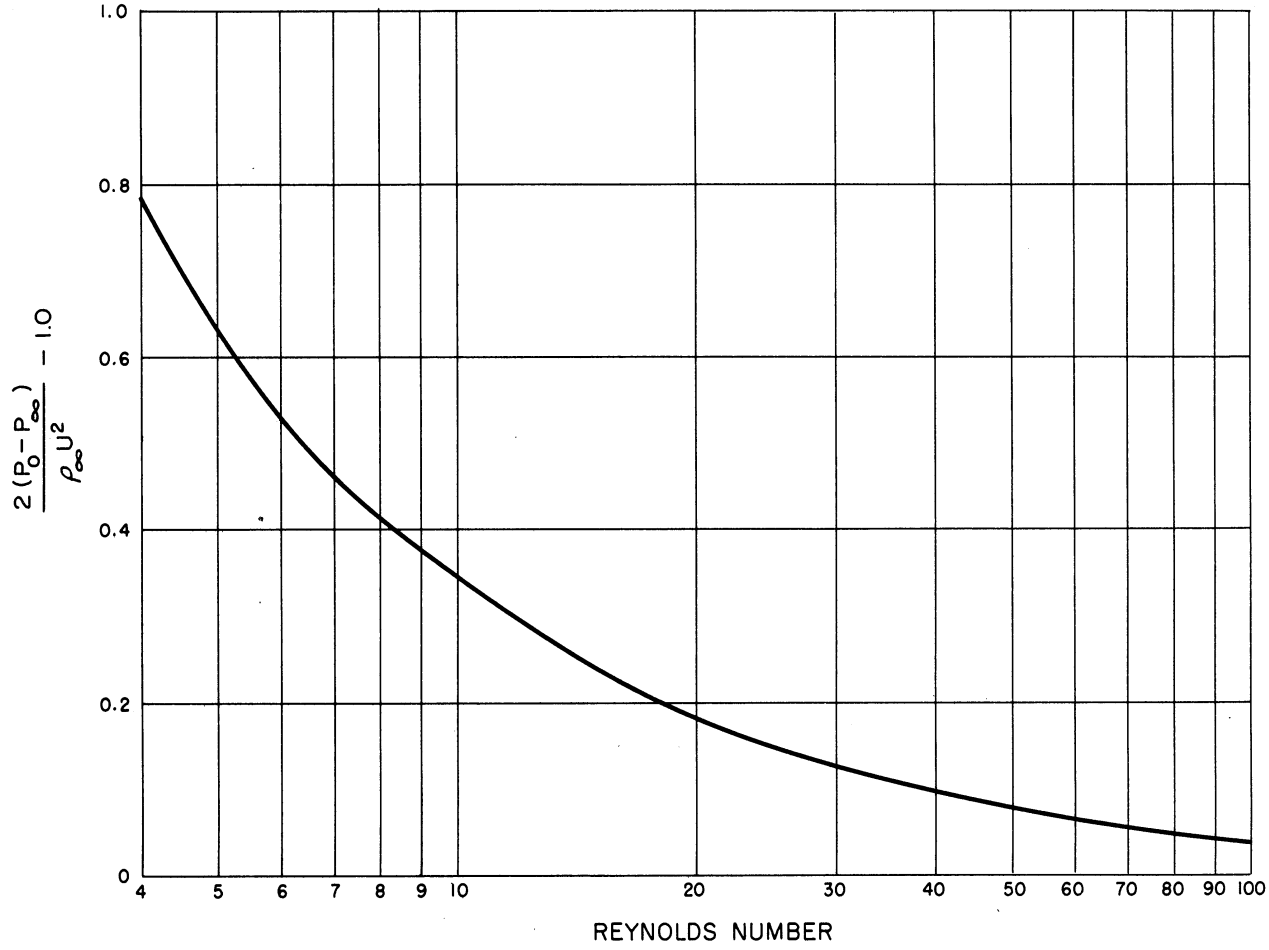

FIG. 3. CHANGE IN THE DIMENSIONLESS PRESSURE DIFFERENCE DUE TO THE VISCOUS EFFECT AS A FUNCTION OF REYNOLDS NUMBER

atom system is in equilibrium, and that only single ions are present. The diffusion of ions and electrons is taken to be ambipolar -- that is, ions and electrons moving together so that there is no net current flow and no net charge density at any point. This concept is analyzed in more detail in Appendix A. The thermal diffusion effect is ignored. Sherman (49) has shown that this is valid. Viscous dissipation and the pressure gradient are ignored in the energy equation. In final form, the effect of ion diffusion-recombination will appear as a reactive heat capacity and a reactive thermal conductivity.

With the above restrictions the boundary layer equations are:

1. Continuity

$$\frac{\partial}{\partial z}(\rho u) + \frac{1}{r}\frac{\partial}{\partial r}(\rho v r) = 0 \quad . \qquad (4\text{-}34)$$

2. Momentum

$$\rho\left(v\frac{\partial v}{\partial r} + u\frac{\partial v}{\partial z}\right) = -\frac{\partial P}{\partial r} + \frac{\partial}{\partial z}\left(\mu\frac{\partial v}{\partial z}\right) \quad . \qquad (4\text{-}35)$$

3. Energy

$$\rho\left(v\frac{\partial h}{\partial r} + u\frac{\partial h}{\partial z}\right) + \frac{\partial}{\partial z}\left(\sum_k h_k J_k\right) = -\frac{\partial}{\partial z}\left(-K\frac{\partial T}{\partial z}\right) \quad . \qquad (4\text{-}36)$$

The transport properties K and μ are those of the ion-electron-atom system. In the energy equation, h is the specific enthalpy of the system, defined by

$$h = \sum_k c_k h_k \quad , \tag{4-37}$$

where h_k = specific enthalpy of species k

c_k = weight fraction of species k;

and J_k is the mass diffusion flux of species k in the z direction and satifies at any point

$$\sum_k J_k = 0 \quad . \tag{4-38}$$

In the boundary layer, the diffusion fluxes for ambipolar diffusion which are derived in Appendix A become:

$$J_a = \frac{P(1+\alpha)}{kT} m_a (2 D_{ia}) \frac{\partial x_i}{\partial z} \quad , \tag{4-39a}$$

$$J_i = \frac{P(1+\alpha)}{kT} m_i (-2 D_{ia}) \frac{\partial x_i}{\partial z} \quad , \tag{4-39b}$$

and

$$J_e = \frac{P(1+\alpha)}{kT} m_e (-2 D_{ia}) \frac{\partial x_i}{\partial z} \quad . \tag{4-39c}$$

The subscripts a, i, and e refer respectively to atom, ion, and electron. To evaluate the specific enthalpy of each species, the ionization energy is assumed to reside in the electron (49). Thus:

$$h_a = \frac{5kT}{2m_a} \quad , \qquad (4\text{-}40a)$$

$$h_i = \frac{5kT}{2m_i} \quad , \qquad (4\text{-}40b)$$

and

$$h_e = \frac{5kT}{2m_e} + \frac{I}{m_e} \quad , \qquad (4\text{-}40c)$$

where I is the ionization energy. Using equations (4-39) and (4-40),

$$\sum_k h_k J_k = -\frac{P(1+\alpha)}{kT}(2D_{ia})\left(\frac{5}{2}kT + I\right)\frac{\partial x_i}{\partial z} \quad . \qquad (4\text{-}41)$$

At constant pressure, equation (4-41) can be written

$$\sum_k h_k J_k = f(T)\frac{\partial x_i}{\partial z} \quad , \qquad (4\text{-}42)$$

and since pressure variations are small compared to temperature

variations in the plasma boundary layer,

$$\sum_k h_k J_k = f(T) \frac{\partial x_i}{\partial T} \frac{\partial T}{\partial z} \quad . \qquad (4\text{-}43)$$

The reactive thermal conductivity at constant pressure due to ion diffusion - recombination is defined by

$$\sum_k h_k J_k = -K_r \frac{\partial T}{\partial z} \quad , \qquad (4\text{-}44)$$

and hence

$$K_r = \frac{P(1+\alpha)}{kT} (2 D_{ia}) \left(\frac{5kT}{2} + I \right) \frac{\partial x_i}{\partial T} \quad . \qquad (4\text{-}45)$$

To evaluate $\frac{\partial x_i}{\partial T}$, consider the equilibrium constant for the ion-atom-electron system at constant pressure, and its variation with temperature (39):

$$K_p = \frac{x_i^2}{1-2x_i} \quad , \qquad (4\text{-}46)$$

and

$$\frac{\partial (\ln K_p)}{\partial T} = \frac{\Delta h}{kT^2} \quad . \qquad (4\text{-}47)$$

Using equations (4-46) and (4-47)

$$\frac{\partial x_i}{\partial T} = \frac{\Delta h}{kT^2} \frac{x_i(1-2x_i)}{2(1-x_i)} \quad . \tag{4-48}$$

However,

$$\Delta h = \frac{5kT}{2} + I \quad , \tag{4-49}$$

and from Appendix A

$$x_i = \frac{\alpha}{1+\alpha} \quad . \tag{4-50}$$

Substituting into equation (4-48) and simplifying

$$\frac{\partial x_i}{\partial T} = \frac{\alpha(1-\alpha)}{2(1+\alpha)} \frac{\left(\frac{5kT}{2}+I\right)}{kT^2} \quad , \tag{4-51}$$

and finally,

$$K_r = \frac{P D_{ia} \alpha (1-\alpha)}{k^2 T^3} \left(\frac{5kT}{2} + I\right)^2 \quad . \tag{4-52}$$

Devoto (17) also deduced this expression for K_r. The energy equation in the boundary layer now becomes

$$\rho\left(v\frac{\partial h}{\partial r} + u\frac{\partial h}{\partial z}\right) = \frac{\partial}{\partial z}\left[(K+K_r)\frac{\partial T}{\partial z}\right] \quad . \tag{4-53}$$

Next, it is necessary to write h as a function of temperature. Recalling equation (4-37),

$$h = \sum_k c_k h_k \quad , \tag{4-37}$$

and the differential of h is

$$dh = \sum_k c_k dh_k + \sum_k h_k dc_k \quad . \tag{4-54}$$

Since pressure changes are small as noted previously, h_k is essentially a function of temperature:

$$dh_k = C_{pk} dT \quad . \tag{4-55}$$

Then

$$dh = C_p dT + \sum_k h_k dc_k \quad , \tag{4-56}$$

where C_p is the heat capacity at constant pressure of the system, given by

$$C_p = \sum_k c_k C_{pk} \quad . \tag{4-57}$$

The weight fractions c_k can be expressed in terms of x_i as follows:

$$c_a = \frac{1-2x_i}{1-x_i} \quad , \tag{4-58a}$$

$$c_i = \frac{m_i}{m_a} \frac{x_i}{(1-x_i)} \quad , \tag{4-58b}$$

and

$$c_e = \frac{m_e}{m_a} \frac{x_i}{(1-x_i)} \quad . \tag{4-58c}$$

Taking differentials of equations (4-58) and using equations (4-40), equation (4-56) becomes after simplification

$$dh = C_p\, dT + \frac{dx_i}{m_a (1-x_i)^2}\left(\frac{5kT}{2} + I\right) . \tag{4-59}$$

But at constant pressure

$$dx_i = \frac{\partial x_i}{\partial T}\, dT \quad , \tag{4-60}$$

so that

$$dh = C_p\, dT + \frac{x_i(1-2x_i)\left(\frac{5kT}{2} + I\right)^2}{2 m_a (1-x_i)^3 kT^2}\, dT \quad . \tag{4-61}$$

Substituting for x_i using equation (4-50) and rearranging

$$dh = C_p dT + \frac{\alpha(1-\alpha^2)(\frac{5kT}{2}+I)^2}{2m_a kT^2} dT \quad . \qquad (4\text{-}62)$$

Or, defining the reactive heat capacity at constant pressure as follows

$$dh = (C_p + C_{pr})dT \quad , \qquad (4\text{-}63)$$

where

$$C_{Pr} = \frac{\alpha(1-\alpha^2)(\frac{5kT}{2}+I)^2}{2m_a kT^2} \quad , \qquad (4\text{-}64)$$

the energy equation reduces to

$$\rho(C_p + C_{pr})(v\frac{\partial T}{\partial r} + u\frac{\partial T}{\partial z}) = \frac{\partial}{\partial z}\left[(K+K_r)\frac{\partial T}{\partial z}\right] \quad . \qquad (4\text{-}65)$$

The properties ρ, μ, C_p, C_{pr}, and K, and K_r in equations (4-34), (4-35), and (4-65) are strongly dependent on temperature. Because of the large temperature gradient across the boundary layer, these properties are not constant, and a forthright analytical solution to the system of equations is not easily obtained. A numerical solution would be cumbersome and most likely, quite restrictive because of the necessity of assuming

arbitrary temperature dependencies of the transport properties. Thus, the reference temperature technique is both useful and practical in accounting for variable fluid properties. A characteristic (reference) temperature is chosen, at which fluid properties are evaluated, such that constant property results at this temperature can be used to represent true variable property behavior (35). If the heat capacity does not vary significantly through the boundary layer, the mean boundary layer temperature can be used as the reference temperature. If, however, there are large temperature differences across the boundary layer as would be encountered in plasma flow, the heat capacity can no longer be considered constant and the temperature corresponding to the mean boundary layer enthalpy is selected as the reference temperature (21). The mean enthalpy is referred to as the reference enthalpy.

Thus, by assuming the fluid properties constant, evaluated at the reference conditions, the system of boundary layer equations becomes:

1. Continuity

$$r\frac{\partial u}{\partial z} + \frac{\partial}{\partial r}(rv) = 0 \quad . \qquad (4\text{-}66)$$

2. Momentum

$$\rho^*\left(v\frac{\partial v}{\partial r} + u\frac{\partial v}{\partial z}\right) = -\frac{\partial P}{\partial r} + \mu^*\frac{\partial^2 v}{\partial z^2} \quad . \qquad (4\text{-}67)$$

3. Energy

$$\rho^{*}(C_p+C_{pr})^{*}\left(v\frac{\partial T}{\partial r}+u\frac{\partial T}{\partial z}\right)=(K+K_r)^{*}\frac{\partial^2 T}{\partial z^2} \quad . \quad (4\text{-}68)$$

In the above equations * denotes reference conditions. Sibulkin (50), following the method of Squire (24) and using Homann's stagnation point solution of the momentum equation (29), obtained a solution to the above system of equations. In dimensionless form the heat transfer coefficient is given by

$$\frac{hR}{K}=0.763\left(\frac{C_p\mu}{K}\right)^{0.4}\left(\frac{R^2\beta\rho}{\mu}\right)^{0.5} . \quad (4\text{-}69)$$

As in the stagnation streamline development

$$\beta=\frac{\partial v}{\partial r} \quad , \quad (4\text{-}27)$$

and is evaluated at the stagnation point in a potential flow field. Substituting for β using equation (4-29) and including both the kinetic and reactive contributions to the heat capacity and thermal conductivity, the stagnation point heat coefficient is

$$h=\frac{0.763(K+K_r)^{*}}{R}\left[\frac{(C_p+C_{pr})^{*}\mu^{*}}{(K+K_r)^{*}}\right]^{0.4}\left[\frac{\rho^{*}RU}{\mu^{*}}\right]^{0.5} . \quad (4\text{-}70)$$

where R is the radius of the half body, U the free stream

approach velocity, and all fluid properties are evaluated at the reference temperature.

Equation (4-70) was used to resolve the data of Chludzinski (15) to demonstrate the applicability of the reference temperature method to plasma flow problems. As noted previously, Chludzinski studied heat transfer to solids immersed in an r.f. generated plasma. Heat transfer coefficients were determined from the dynamic response of shielded thermocouples exposed to an argon plasma for time periods of approximately 0.1 sec. The thermocouple was housed within a water-cooled probe, and was advanced to the probe stagnation point and retracted by means of solenoids mounted above the cooling water jacket. Three diameters were used, and for each, data were obtained at several plasma temperatures. The results were presented as a function of free stream ion concentration. The measured heat transfer coefficients exhibited a negative half power dependence on the probe diameter which indicates that a convective model should describe the heat transport process, but the experimental values were significantly higher than those calculated from the conventional stagnation point correlation. Reactive contributions to the heat capacity and thermal conductivity were not considered in the calculations. An attempt was made to separate the contribution of the ion-electron recombination reaction occurring near the probe wall from the measured values of the heat transfer

coefficients. An empirical relationship for this contribution was obtained, but the information was judged insufficient to formulate an analytical model for describing the effect of the ion-electron recombination reaction on the overall energy transfer process.

For the flow rate employed during the Chludzinski measurements, heat transfer coefficients were calculated from equation (4-70) as a function of plasma temperature for the three probe diameters used in the experiments — 0.020 in., 0.040 in., and 0.0625 in. The plasma temperature was varied from 8500 ^{o}K to 10,500 ^{o}K which corresponds to the temperature range of the measurements. The physical properties ρ and $(C_p + C_{pr})$ for argon were obtained from the tabulated values of Drellishak et. al. (20). The tabulated values of heat capacity are actually the sum $(C_p + C_{pr})$ of kinetic and reactive contributions. The values used for the transport properties K and μ were those calculated by Sherman (48), which include the effects of electron excitation and ionization. The reactive contribution to the thermal conductivity is not included, however, so that K_r must be calculated as a function of temperature from equation (4-52). In applying this equation, α was obtained from the Saha equation (to be discussed in the following section) and the values taken for D_{ia} were also those of Sherman. The contribution of K_r to the total thermal conductivity becomes significant at temperatures above 9000 ^{o}K.

The reference temperature, at which all quantities in equation (4-70) must be evaluated, was obtained for a given free stream temperature from the reference enthalpy, previously defined as

$$h^* \equiv h_w + 0.5(h_\infty - h_w) \quad , \qquad (4\text{-}71)$$

where * denotes reference conditions

w denotes wall conditions

∞ denotes free stream conditions.

The reference enthalpy was converted to temperature by means of the Drellishak tables. In equation (4-71) the enthalpy at the wall temperature for the water-cooled probe is so small compared to the free stream enthalpy that the reference enthalpy and hence, the reference temperature, are essentially functions of the free stream temperature. The relationship is not linear because the heat capacity varies. For these calculations, the wall temperature was estimated to be 560 ^{o}K (550 ^{o}F). The insensitivity of reference temperature to wall temperature is illustrated by the fact that had 800^{o}K (980 ^{o}F) been chosen as the wall temperature, an increase of less than 2.5% in the reference temperature would have resulted.

The theoretical predictions of h obtained by using equation (4-70) for the three probe sizes are plotted in Figure 4 as a function of the free stream value of α,

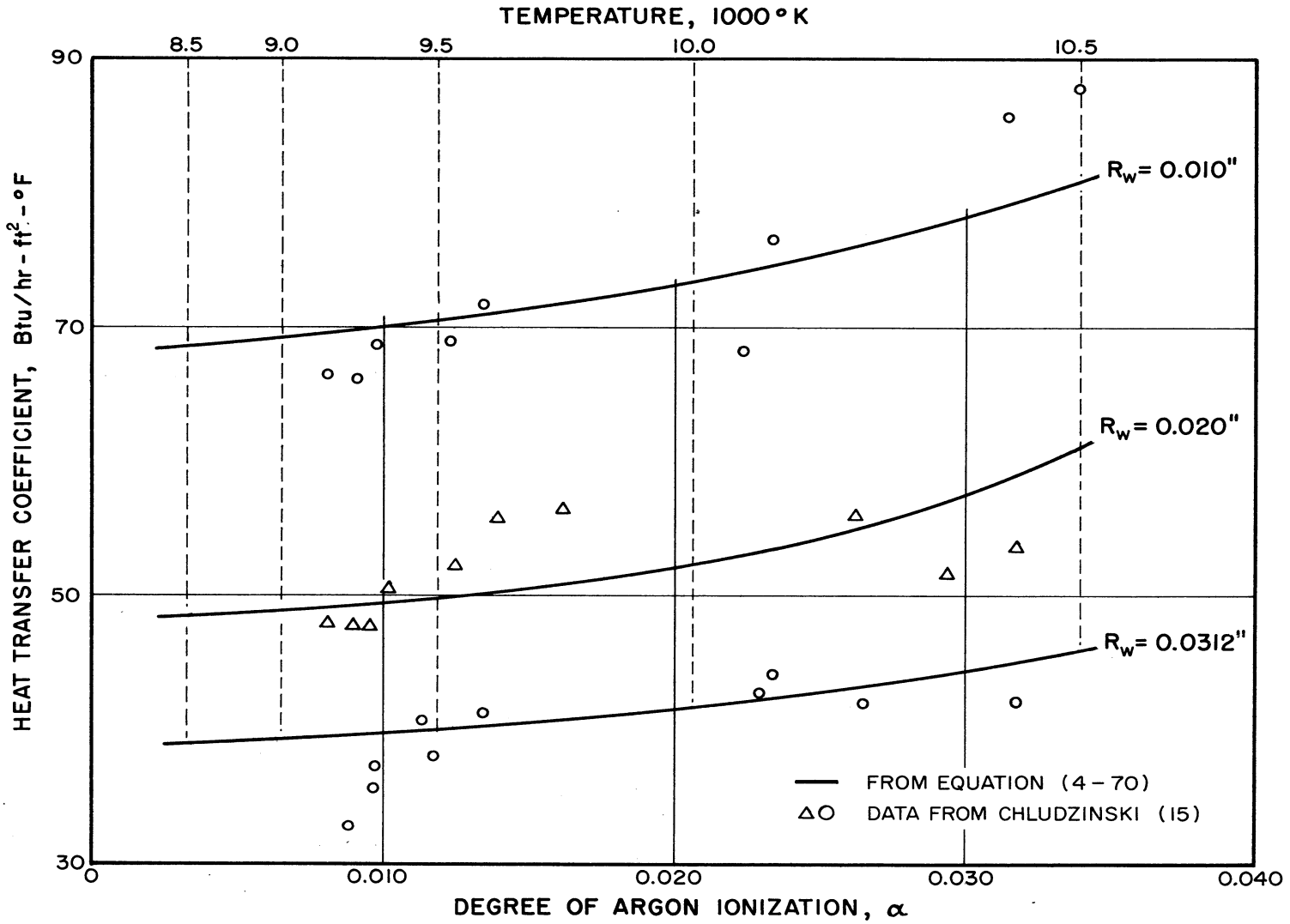

FIG. 4. CALCULATED AND OBSERVED HEAT TRANSFER COEFFICIENTS AS A FUNCTION OF THE DEGREE OF ARGON IONIZATION

the degree of argon ionization. The range of α corresponds to the free stream temperature range of 8500 ^{o}K to 10,500 ^{o}K. The temperature scale, which is not linear, is indicated. Experimental values are also shown in Figure 4. In light of the scatter in the data, the agreement between experiment and prediction is considered excellent. It is concluded therefore, that the reference temperature technique is justified for plasma flow problems.

Plasma Radiation

To make calculations dealing with stagnation streamline flow and stagnation point heat transfer in a plasma jet, a knowledge of the plasma temperature is required. The temperature of a plasma can be determined indirectly by analyzing the radiation it emits. Before attempting to relate temperature to the intensity of radiation emitted, however, it is first necessary to discuss the concept of equilibrium in a plasma. It is assumed that the plasma consists of atoms, single ions, and electrons. The possibility of multiple ionization is not considered, although it would be handled in the same manner. All species have translational energy, atoms can possess excitation energy, and ions possess ionization energy.

Equilibrium True thermodynamic equilibrium can exist in a system of particles only when the system is isolated and does not exchange mass, momentum, or energy with the surroundings. In such a system, the total energy content is constant and the energy distributions for the various states, involving degrees of freedom of translation, excitation, radiation, and species composition, are determined by a unique parameter independent of time or position called temperature. Each mechanism of energy exchange in the system is exactly balanced by its inverse (2). A plasma jet exchanges energy with the surroundings by emitting radiation, and hence, cannot be in complete thermodynamic equilibrium. It is then necessary to turn to the concept of local thermodynamic equilibrium.

Local thermodynamic equilibrium exists in a system of particles if the distribution functions for the kinetic (translational) states of the particles and the excited states, and the chemical composition are the same as in a system at complete thermodynamic equilibrium, but at a single local temperature (9). Thus, for a plasma exhibiting local thermodynamic equilibrium, the velocity distribution of the atoms, ions, and electrons, is Maxwellian, the distribution of population densities of excited atomic states is Boltzmannian, and the distribution of atoms and ions obeys the Saha equation at each point in the system (19). The radiation field, however, is not black body (given

by the Planck function), but is a line spectrum characteristic of the element and is determined by the Einstein relation. A gradient in the local temperature may exist, but the relative change must be small so that a particle moving from one position to another has sufficient time to equilibrate. Then, steady-state distributions are established at each location in the plasma, and the local temperature specifying these distributions has meaning. The change in temperature, in effect, is continuous. Thus, the system can be subjected to a directional flow of energy, although at each point, the average energy being transferred must be small in comparison to the total energy content of the system. In plasmas, local thermodynamic equilibrium will prevail as long as collisional rate processes among particles not directly connected with radiation energy transfer are predominant, the radiation rate processes being small in comparison. Then, the distribution functions will be determined by particle collisions which tend to equilibrate the various forms of energy distribution (45).

In systems where local thermodynamic equilibrium does not exist, the situation becomes somewhat more complicated. It becomes necessary to differentiate among the temperatures corresponding to the various degrees of freedom because it could be possible to assign a separate temperature to the distribution function for each degree of freedom. For a plasma, there could be a Boltzmann temperature characterizing the distribution of excited atomic states, a heavy particle

temperature describing the distribution of the translational energy of atoms and ions, a Saha temperature specifying the degree of ionization, and an electron temperature associated with the kinetic energy of the free electrons. Fortunately however, most plasmas at atmospheric pressure or above are very close to being in local thermodynamic equilibrium so that approximately the same temperature can be assigned to the translation, excitation, and ionization degrees of freedom.

Line Emission The excited atomic states mentioned above are discrete (quantized) and arise from a gain in potential energy through collisions which causes an orbital electron of the atom to be relocated in an orbit of higher energy value. This electron can make a spontaneous transition to an orbit of lower energy value by emitting radiation. Such a process between quantized states results in a characteristic spectral line. The volume emission coefficient for this line depends upon the energy associated with the particular transition, which is related to the wavelength λ by

$$E_u - E_l = \frac{hc}{\lambda} \quad , \qquad (4\text{-}72)$$

where E_u, E_l = energy of the upper and lower levels respectively

h = Planck's constant

c = speed of light ,

and upon the number of downward transitions per second, which is expressed in terms of the concentration of atoms in the higher excited energy level n_u and the probability per second for the transition of interest A_{ul} , known as the Einstein transition probability. The Einstein relation then for the line emission coefficient is

$$\mathcal{E}_{line} = \frac{hc}{4\pi\lambda} n_u A_{ul} \quad . \qquad (4\text{-}73)$$

Equation (4-73) involves only constants of the particular species and does not depend on the existence of any equilibrium conditions. If local thermal equilibrium does prevail, a Boltzmann distribution can be assigned to the populations of the excited states, and the number density of atoms in the upper state n_u is related to that of atoms in the lower state n_l by

$$\frac{n_u}{n_l} = \frac{g_u}{g_l} e^{-\frac{(E_u - E_l)}{kT}} \quad , \qquad (4\text{-}74)$$

where g_u, g_l = statistical weight of the upper and lower energy levels

k = Boltzmann's constant

T = temperature .

Summing over all of the discrete energy levels of the excited atomic states up to the ionization energy, with the energy of the lowest level taken to be zero, the Boltzmann distribution becomes

$$\frac{n_u}{n_a} = \frac{g_u}{Z_a} e^{-\frac{E_u}{kT}} \quad , \qquad (4\text{-}75)$$

where n_a is the total number density of atoms and Z_a is the internal partition function of the atom, defined by

$$Z_a = \sum_r g_r e^{-\frac{E_r}{kT}} \quad . \qquad (4\text{-}76)$$

The atomic number density is obtained from the Saha equation and the ideal gas law. The Saha equation is the equilibrium relationship for the ionization reaction at temperature T, and is

$$\frac{n_i n_e}{n_a} = \frac{2Z_i}{Z_a} \left(\frac{2\pi m_e kT}{h^2}\right)^{\frac{3}{2}} e^{-\frac{I}{kT}} \quad , \qquad (4\text{-}77)$$

where n_i, n_e, n_a = number density of ions, electrons, and atoms respectively

Z_i = internal partition function of the first ion

m_e = electron mass

I = ionization energy .

Assuming that the ion-electron-atom system behaves as an ideal gas

$$(n_a + n_i + n_e) = \frac{P}{kT} \quad , \qquad (4\text{-}78)$$

with P being the system pressure. Since by definition (from Appendix A)

$$\alpha = \frac{n_i}{n_i + n_a} \quad , \qquad (4\text{-}79)$$

the Saha equation (4-77) can be combined with equation (4-78) and written in its familiar form

$$\frac{\alpha^2}{1-\alpha^2} = \left(\frac{\pi m_e}{h^2}\right)^{\frac{3}{2}} \frac{(2kT)^{\frac{5}{2}}}{P} \frac{Z_i}{Z_a} e^{-\frac{I}{kT}} \quad . \qquad (4\text{-}80)$$

The partition functions Z_i and Z_a are functions of pressure and temperature, and have been tabulated (20). Thus equations (4-78), (4-79), and (4-80) are used to determine n_a, and the line emission coefficient becomes

$$\mathcal{E}_{line} = \frac{hc}{4\pi\lambda} \frac{g_u A_{ul}}{Z_a} n_a e^{-\frac{E_u}{kT}} \quad . \qquad (4\text{-}81)$$

Because a line has finite width, the emission coefficient is actually the integral of the line profile $\mathcal{E}_\lambda$, so that

$$\mathcal{E}_{line} = \int_{line} \mathcal{E}_\lambda \, d\lambda \quad . \qquad (4\text{-}82)$$

Working with a single line for which the required constants are known, equation (4-81) can be used to determine the temperature of a plasma in local thermal equilibrium at a given pressure if ε_{line} is known. The calculation is trial and error, however, because Z_a and n_a are functions of temperature. In practice, it is somewhat easier to use tabulated values of Z_a and n_a at the desired pressure and prepare a plot of ε_{line} as a function of temperature. Figure 40 in Appendix B shows these plots at atmospheric pressure for the 4158, 4181, 4259, 4300, and 4510 $\overset{o}{A}$ argon lines which were used during the course of this work. Also found in Appendix B is Table VIII, containing the required atomic constants for the lines mentioned above.

Continuum Emission The discrete spectral lines in the radiation emitted by a plasma are superimposed on a continuous spectrum. Continuum emission results from transitions involving free electrons whose energy is unquantized. There are two types of electron transitions - free-free and free-bound. A free-free transition is simply a change in energy from one unquantized state to another, and in general, occurs when the electron undergoes an acceleration in the field of another charged particle. A free-bound transition is the recombination of a free electron - a change from an unquantized (free) state to an quantized (bound) state. The continuum volume emission coefficient represents the sum of free-free and free-bound transitions of electrons in the field of

ions having an effective average charge z^2, and is given by (8)

$$\epsilon_\lambda = \frac{32c\pi^2e^6}{(6\pi m_e)^{\frac{3}{2}}} \frac{\bar{g}z^2 n_i n_e}{\lambda^2 (kT)^{\frac{1}{2}}} \quad , \qquad (4\text{-}83)$$

where e = electron charge

λ = wavelength .

Equation (4-83) is not, strictly speaking, valid for argon since it was obtained by assuming dense, hydrogen-like electron energy levels in the treatment of the contribution of free-bound transitions. However, its temperature and number density dependence are correct, and the quantuum mechanical correction factor $\bar{g}$ compensates for non-hydrogen like behavior. The temperature dependence of $\bar{g}$ is negligible for argon, as is the wavelength dependence in the range 4500 $\mathring{A}$ to 5600 $\mathring{A}$ (41). It has been measured experimentally at 5330 $\mathring{A}$ and found to be 2.3 (8). The electron temperature T is the temperature which specified a Maxwell-Boltzmann distribution of the energies of the free electrons. In general, z is given by

$$z = \frac{n_e}{n_i} \quad , \qquad (4\text{-}84)$$

where n_i is the number density of all ions. Since only single ions are assumed present in this development, z is one.

If ϵ_λ is known in the range 4500 $\mathring{A}$ to 5600 $\mathring{A}$, equation (4-83)

can be used along with the Saha equation to obtain the temperature of a plasma in local thermal equilibrium. As before the calculation is trial and error, so that it is again expedient to use tabulated values of n_i and n_e at the desired pressure and prepare a plot of ϵ_λ as a function of temperature. Figure 41 in Appendix B shows the argon continuum emission coefficient at 5330 $\overset{o}{A}$ as a function of temperature at atmospheric pressure.

Equilibrium Determination The expressions presented above relating line and continuum emission coefficients to the plasma temperature are restricted to plasmas exhibiting local thermal equilibrium. While it was stated previously that for a plasma at atmospheric pressure or higher, the assumption of local thermal equilibrium is usually valid, it is worthwhile at this point to briefly note how to ascertain if in fact equilibrium does prevail. To verify its existence, the temperatures specifying the energy distributions for different degrees of freedom must be obtained and compared. In this case the emission coefficients for lines resulting from different upper energy levels are plotted in such a way as to show if a Boltzmann distribution can be assigned to the populations of the excited states. Then, the temperature characterizing the Boltzmann distribution, if one exists, is used to obtain number densities from the Saha equation, and these number densities employed to calculate the electron temperature from the continuum emission coefficient. If a Boltzmann distribution exists and if the electron temperature compares

favorably with the heavy particle (Boltzmann) temperature, local thermodynamic equilibrium does prevail.

The existence of a Boltzmann distribution for the population densities of the excited atomic states is demonstrated in the following manner. For a specific line, equation (4-81), can be written

$$\frac{\varepsilon_{line}\,\lambda}{g_u A_{ul}} = C_1 \frac{n_a}{Z_a} e^{\frac{-E_u}{kT}} \quad , \qquad (4\text{-}85)$$

where C_1 is a constant. Assuming that a local temperature can be assigned at a given point, equation (4-85) at this particular point becomes

$$\frac{\varepsilon_{line}\,\lambda}{g_u A_{ul}} = C_2 e^{\frac{-E_u}{kT}} \quad , \qquad (4\text{-}86)$$

where C_2 is another constant. Taking logarithms of equation (4-86)

$$\ln\left[\frac{\varepsilon_{line}\,\lambda}{g_u A_{ul}}\right] = \ln C_2 - \frac{E_u}{kT} \quad . \qquad (4\text{-}87)$$

Then, if $\frac{\varepsilon_{line}\,\lambda}{g_u A_{ul}}$ is plotted against E_u on semi-log paper for the discrete energy levels corresponding to several spectral lines, a straight line of slope $-\frac{1}{kT}$ will result provided there is a Boltzmann distribution at the point in question. The technique must be applied at different locations in the radiation field to see if a Boltzmann distribution prevails throughout. The plot is referred to as a Boltzmann plot.

Intensity-Emission Relationship The specific intensity of a radiation source at wavelength λ that would be observed

experimentally, I_λ, is related to emission coefficient of the source at the wavelength, ϵ_λ or $\mathcal{E}_\lambda$, by

$$I_\lambda = \int (\epsilon_\lambda \text{ or } \mathcal{E}_\lambda)\, dl \quad , \qquad (4\text{-}88)$$

where dl is the incremental length in the direction of observation through the source. Equation (4-88) is based on the assumption that the radiation source is optically thin; that is, the self-absorption of radiation emitted by the source is negligible. In this case, the radiation source is a round, symmetrical plasma jet. The geometry associated with this jet is depicted below.

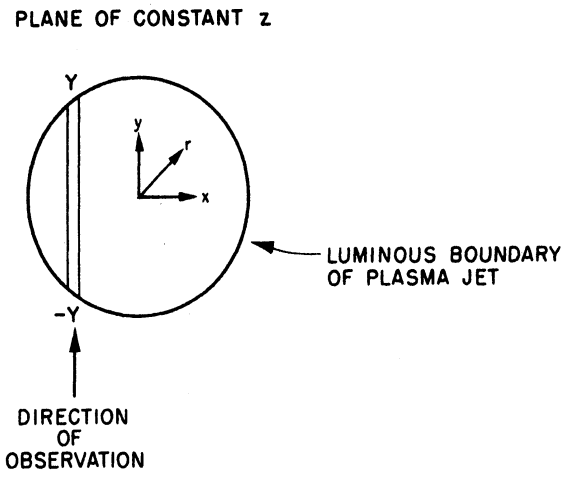

FIG. 5. GEOMETRY OF THE SPECTOGRAPHIC OBSERVATIONS

Introducing a new notation, the specific intensity expressed in equation (4-88) can be written at any chord position x in a plane of constant z as

$$I_\lambda(x,z) = \int_{-Y}^{Y} \epsilon_\lambda(r,z)\, dy \quad , \qquad (4\text{-}89)$$

with the integral taken along the chord of constant x. The observed specific intensity $I_\lambda(x,z)$ represents a cumulative emission through the plasma because there may be a gradient in ϵ_λ along the axis of observation due to the variation in radial position r and hence, a variation in temperature. At constant x,

$$dy = \frac{rdr}{y} \quad , \tag{4-90}$$

and since

$$y = (r^2 - x^2)^{\frac{1}{2}} \quad , \tag{4-91}$$

equation (4-89) for the symmetrical source becomes

$$I_\lambda(x,z) = 2\int_x^R \frac{\epsilon_\lambda(r,z)\, rdr}{(r^2-x^2)^{\frac{1}{2}}} \quad . \tag{4-92}$$

The upper limit R is the radius beyond which $\epsilon_\lambda(r,z)$ vanishes. If a spectral line is observed, the intensity profile of the line must be integrated. Thus

$$\int_{\text{line}} I_\lambda(x,z)\, d\lambda = 2\int_{\text{line}} \int_x^R \frac{\epsilon_\lambda(r,z)\, rdr\, d\lambda}{(r^2-x^2)^{\frac{1}{2}}} \quad . \tag{4-93}$$

Interchanging the order of integration on the right hand side of equation (4-93) and performing the integration with respect to

wavelength at a given point,

$$I_{line}(x,z) = 2\int_{x}^{R} \frac{\varepsilon_{line}(r,z)\,r\,dr}{(r^2-x^2)^{\frac{1}{2}}} \quad , \qquad (4\text{-}94)$$

where the integrated intensity $I_{line}(x,z)$ is defined by

$$I_{line}(x,z) = \int_{line} I_{\lambda}(x,z)\,d\lambda \quad . \qquad (4\text{-}95)$$

Equations (4-92) and (4-94) are a form of the Abel equation and can be inverted analytically to yield (6)

$$\epsilon_{\lambda}(r,z) = -\frac{1}{\pi}\int_{r}^{R} \frac{\left(\frac{dI_{\lambda}}{dx}\right)dx}{(x^2-r^2)^{\frac{1}{2}}} \quad , \qquad (4\text{-}96)$$

and

$$\varepsilon_{line}(r,z) = -\frac{1}{\pi}\int_{r}^{R} \frac{\left(\frac{dI_{line}}{dx}\right)dx}{(x^2-r^2)^{\frac{1}{2}}} \quad . \qquad (4\text{-}97)$$

Since I_{λ} and I_{line} are obtained as sets of numerical data which may not be conveniently expressed as analytic functions, a numerical technique is used to perform the above inversion. Several numerical solutions have been developed (4, 7, 42). The method of Barr (4) was used in this investigation and is described in Appendix C. Briefly, the method requires that the

radius and the x axis be divided into N equal increments, with values $\epsilon_{\lambda k}$ or $\mathcal{E}_{\text{line k}}$ and $I_{\lambda n}$ or $I_{\text{line n}}$ corresponding to each position 0, 1, ...N on the r and x axes respectively. For equation (4-97) the result becomes

$$\mathcal{E}_{\text{line k}}(z) = \frac{N}{\pi R} \sum_{n=k-2}^{N} \beta_{kn} I_{\text{line n}}(z) \quad k>2 \ , \tag{4-98}$$

and

$$\mathcal{E}_{\text{line k}}(z) = \frac{N}{\pi R} \sum_{n=0}^{N} \beta_{kn} I_{\text{line n}}(z) \quad k\leq 2 \ . \tag{4-99}$$

The β_{kn} are numerical constants which have been tabulated (4). The same relationship holds for ϵ_{λ} and I_{λ} .

Thus, a set of chord line intensities $I_{\text{line}}(x,z)$ or a set of chord continuum intensities $I_{\lambda}(x,z)$ obtained experimentally at a level z in the plasma can be resolved into a radial distribution of line or continuum emission coefficients, from which the temperature profile can be calculated.

5. EXPERIMENTAL APPARATUS

The experimental system used in this study consisted of a plasma generator; support equipment to supply and monitor power, cooling water, and plasma gas; a spectrograph and associated readout equipment for analysis of the radiation emitted by the plasma; a water-cooled pressure sensing probe to measure and record impact pressures in the plasma jet; and a trace gas injection system. A schematic diagram of the overall system is shown in Figure 6. Each component of the overall system is discussed in detail below.

Plasma Generator

The direct-current, constricted arc plasma generator constructed for this study is shown in Figure 7. It was designed to permit flexibility in its operation, and was fabricated in the machine shop of the Department of Chemical and Metallurgical Engineering. The main body consisted of three sections and was mounted vertically with the plasma jet exhausting upward. The middle Micarta section insulated the upper anode section (brass) from the lower cathode section (also brass). The "O"-rings in the cathode section not only sealed the arc chamber from the surroundings, but helped center the cathode holder. A

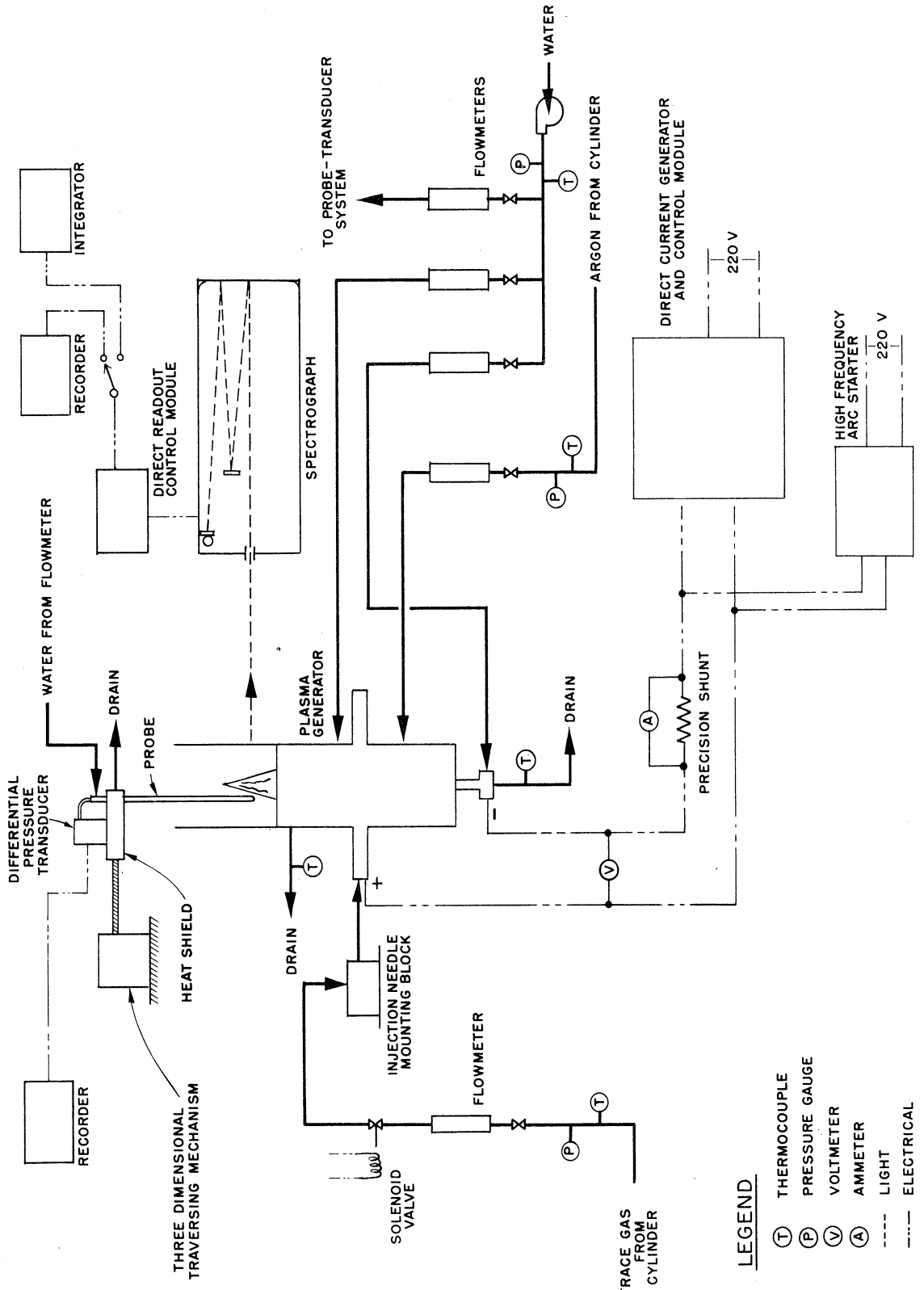

FIG. 6. SCHEMATIC DIAGRAM OF THE EXPERIMENTAL SYSTEM

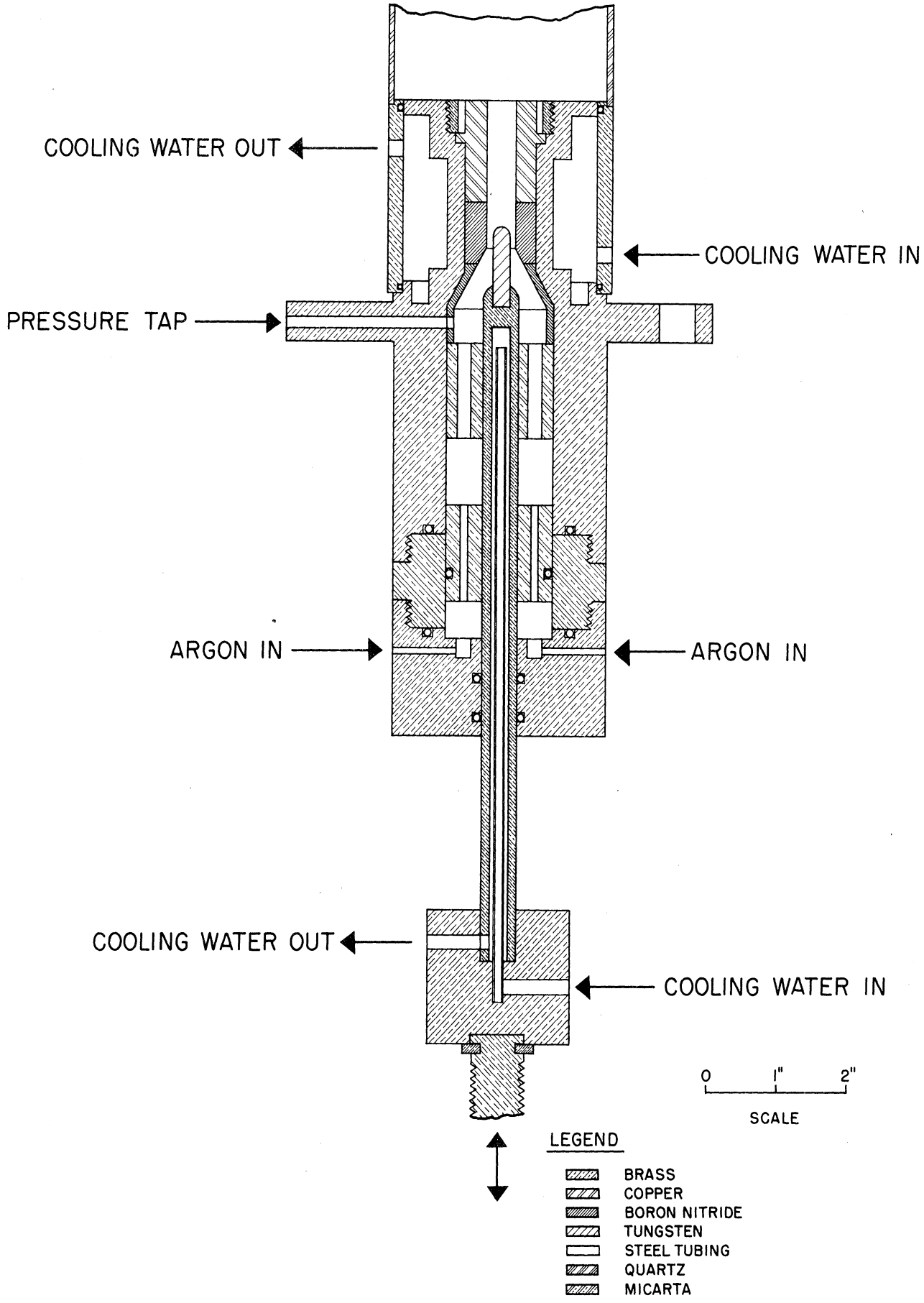

FIG. 7. INTERNAL CONSTRUCTION OF THE CONSTRICTED ARC PLASMA GENERATOR

Micarta gas distribution ring held in the insulating section by an "O"-ring and set screws provided a uniform axial argon flow. A boron nitride insulating sleeve in the converging area of the anode section prevented arcing from the tungsten rod to the brass body. A second Micarta ring to straighten the argon flow was held just below the boron nitride sleeve in the anode section. The two Micarta rings were the primary elements for centering the cathode holder. The boron nitride arc constrictor and the copper anode were both removeable, and were held in place by a brass retaining ring. The annular brass anode sleeve provided a cooling water jacket for the anode section. A cooling water passage also was built into the cathode holder. The shoulder on the top of the anode sleeve supported the concentric quartz tube confining chamber, which was uncooled. The 1% thoriated tungsten rod cathode in the brass cathode holder was removeable. The position of the cathode holder relative to the main body (and thus the electrode separation) could be adjusted by a brass rod threaded through a plexiglass plate held stationary underneath the main body. This rod was attached to the cathode holder with a small collar. The 1/8" hole drilled through the mounting flange (which was welded to the anode section of the main body), the main body, and the boron nitride sleeve into the arc chamber could be used as a pressure tap or for trace gas injection. The power leads

were attached to the mounting flange (positive) and the base of the cathode holder (negative).

Support Equipment

Power was supplied to the plasma generator by a Plasmadyne power system. This unit was essentially a three phase transformer with three phase full-wave bridge rectification, and utilized a saturable reactor current control device. The system was rated at 40 kw with a maximum current load of 1000 amp. The control console monitored the voltage and current, and included safety interlocks which shut off the generator automatically in case of a drop in cooling water pressure or arc gas pressure.

The plasma arc column was initiated between the tungsten rod and the copper anode by a high-frequency arc starter which effected partial ionization of the arc gas.

Argon for the plasma generator was supplied through a calibrated micrometer metering valve. Tap water was used to cool the electrodes and other key areas. It was supplied to the cooling channels by a positive displacement gear pump and monitored with calibrated rotameters. Water and gas temperatures were measured with iron-constantan thermocouples and recorded by a twelve point strip chart recorder calibrated for $0^{o}F$ to $200^{o}F$ operation.

The actual electrode voltage was monitored with a d.c.

digital voltmeter, and the arc current obtained with a precision shunt and a calibrated millivolt meter. Voltage and current fluctuations were observed with a dual trace storage oscilloscope.

Spectrograph

The radiation from the luminous plasma jet was analyzed with an Ebert Mark IV plane grating spectrograph manufactured by the Jarrell Ash Company. The spectrograph, which was equipped with a direct reading head, had a focal length of 3.4 meters. The grating was ruled with 15,000 lines per inch, giving a first order linear dispersion of 5.1 Å per millimeter at the focal plane. It had a useful range of 2100 to 7500 Å. The entrance slit of the spectrograph could be adjusted in width from 4 to 400 microns and in height from 1 to 15 millimeters.

A scanning and condensing system was used to focus selected areas of the extended plasma source on the spectrograph slit. This system consisted of six front surfaced mirrors and two quartz-lithium flouride acromatic lenses, and for any position in the source, automatically maintained focus and alignment with the optical axis of the spectrograph. A manual screw drive mechanism which moved the assembly of six mirrors horizontally permitted horizontal scanning of the plasma jet (perpendicular

to the axis of the jet) at a fixed vertical position. This allowed accurate positioning along chords passing through the jet, with a chord spacing as small as 0.03 cm. The plasma could be scanned vertically (parallel to the axis of the jet) at a fixed horizontal position by pivoting one of the mirrors with a vernier device. The spectrograph and plasma generator were located so that the spectrograph slit and the axis of the plasma jet were parallel.

The spectrograph had a sine bar wavelength drive which rotated the grating in such a way that the wavelength indicated by a counter was seen at the center of the focal plane. The wavelength drive also permitted scanning over intervals of the spectrum at a fixed position in the plasma by switch selection of one of twelve scanning rates ranging from 1 to 500 $\mathring{A}$/min.

Spectra were obtained directly with an RCA 1P28 multiplier phototube placed in the direct reading head at the center of the focal plane. The tube was operated at 1000 volts d.c. provided by a d.c. power supply unit having an output voltage continuously adjustable from 250 to 1500 volts. The tube voltage was monitored with a d.c. digital voltmeter. The output current of the phototube, ranging from 10^{-10} to 10^{-6} amps, was passed through a variable precision resistance and the

resulting voltage amplified by a variable range (50 to 2000 volt) stabilized d.c. microvolt amplifier. The output of the amplifier, 0 to 10 mv or 0 to 1 volt, could be recorded or integrated respectively. To record the amplified photomultiplier signal, a strip chart recorder adjusted to a 0 to 10 mv span was employed. To integrate a spectral line profile, the 0 to 1 volt signal from the microvolt amplifier was fed to a CEC dynamic response function module. This function module employed operational amplifier circuits so that any undesired portion of the signal could be subtracted and the remaining portion integrated with respect to time. The integrator output voltage was also indicated by a d.c. digital voltmeter. Using this system only the line contribution above the continuum was integrated, while the line contribution was superimposed on continuum when the signal was recorded. The photomultiplier-amplifier-recorder system and the photomultiplier-amplifier-integrator system were both calibrated with a ribbon filament tungsten lamp as explained in Appendix D.

Probe

The probe used to measure impact pressures in the plasma jet was essentially a water-jacketed pitot tube. It consisted of three concentric beryllium copper hypodermic tubes held in a brass manifold. At the tip, the annulus between the outer

and inner tubes was sealed to form the jacket by a small copper ring silver-soldered into place. The center tube was the pressure sensing tube, while cooling water circulated through the inner annulus, around the tip, and exited through the outer annulus. The internal construction of the probe is shown in Figure 8. The brass manifold was mounted on a water-cooled copper disc which served as a heat sink. The probe passed through the copper disc and a thick walled steel reinforcing tube attached to the bottom of the heat sink. The pressure sensing tube of the probe passed through the manifold, going directly to a strain gauge differential pressure transducer. The transducer was also mounted on the copper heat shield, in order to cut down dead volume between the probe tip and the sensing element. The pressure tube was sealed to the transducer with a modified thermocouple gland. The combined probe-heat shield-transducer assembly was mounted on a three-dimensional traversing mechanism, and counter-balanced by an overhead system of pulleys and weights. Figure 9 shows the overall probe system and traversing mechanism in relation to the plasma generator. The horizontal drive of the traversing mechanism which controlled lateral movement (movement in the direction parallel to the horizontal scan of the spectrograph) was equipped with a 5.6 rpm. electric motor and belt drive so that the probe could be continuously moved through the plasma

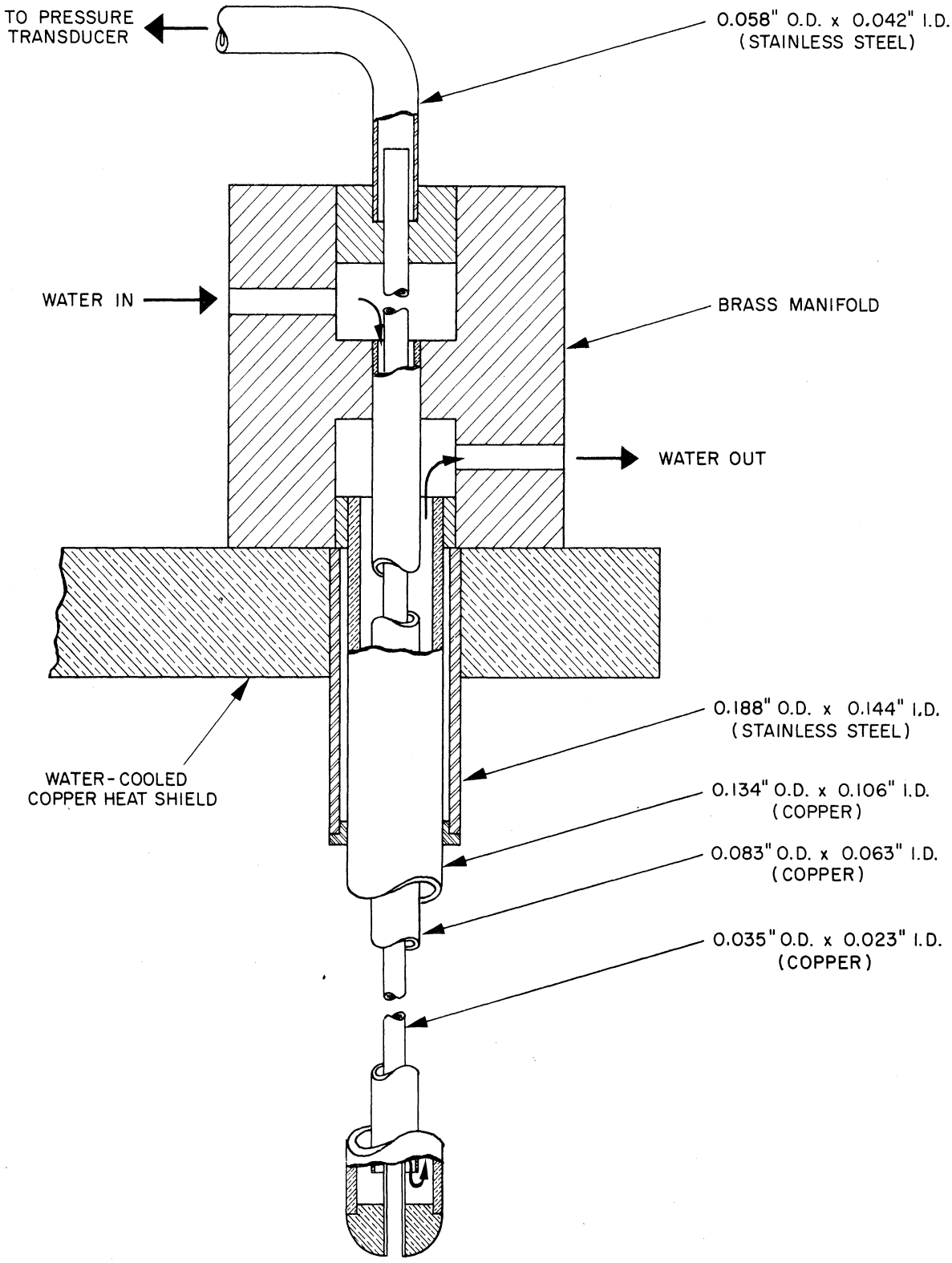

FIG. 8 INTERNAL CONSTRUCTION OF THE WATER-COOLED IMPACT PROBE

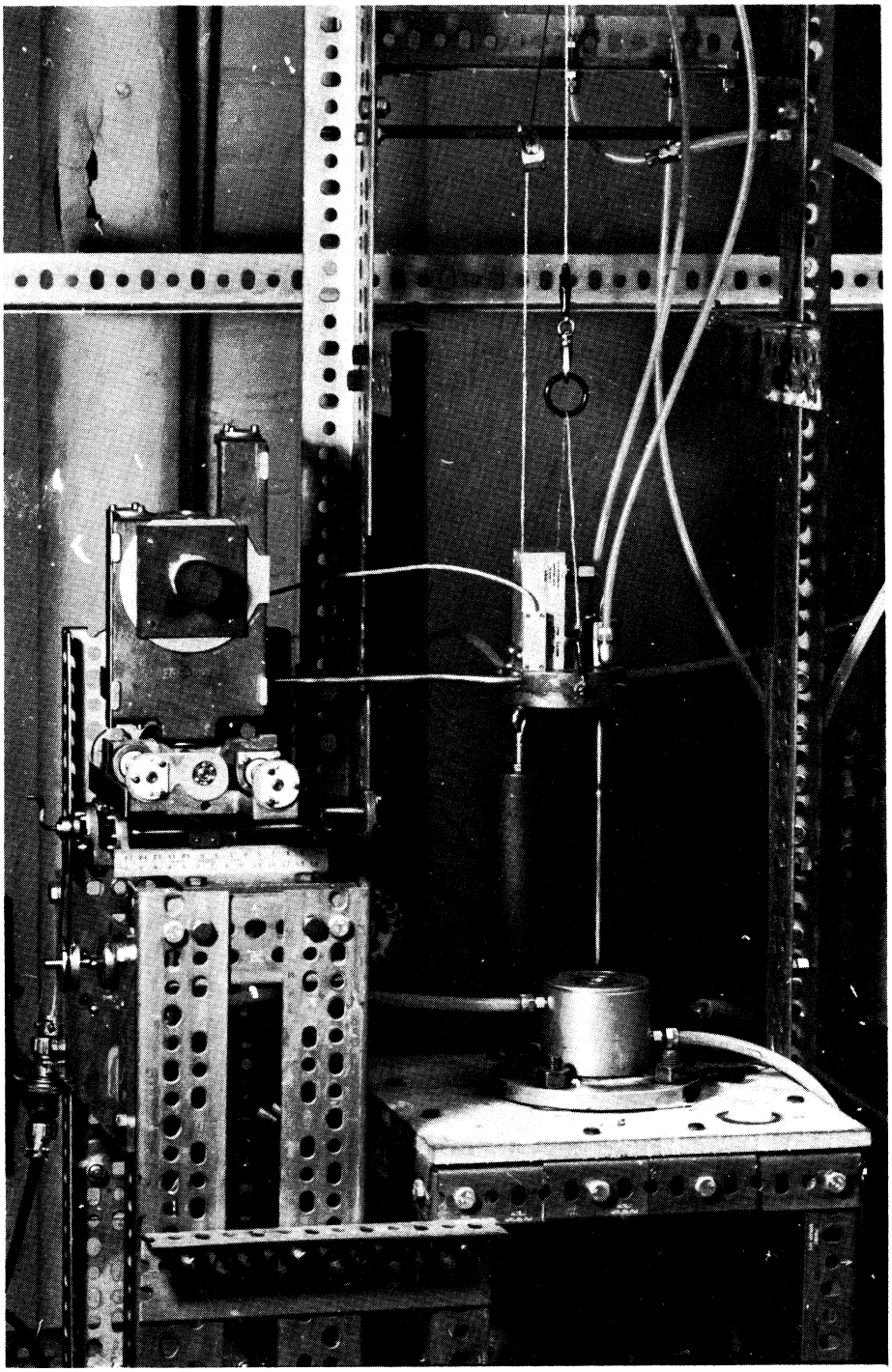

FIG. 9. IMPACT PROBE SYSTEM AND ASSOCIATED EQUIPMENT

jet, or positioned manually. The horizontal drive which controlled depth movement could be set so that the continuous movement corresponded to either a chord or diametrical traverse at a fixed vertical position. The traversing mechanism permitted positioning of the probe tip in the plasma with an accuracy of $\pm$ 0.01 cm. The pulley system restricted movement in any horizontal plane to the jet confining area, but allowed complete freedom of movement along any vertical axis. The pressure transducer could measure a maximum pressure difference of $\pm$ 1 psi with a corresponding maximum output of $\pm$ 30 mv. The excitation voltage, 10 volts d.c., was supplied by two, six-volt dry cells in conjunction with a voltage dividing circuit. The input voltage was monitored and could be maintained within $\pm$ 0.01 volts of the desired value. The transducer output voltage was recorded with a strip chart recorder. The overall probe-transducer-recorder system was calibrated with a water manometer, as explained in Appendix E. Cooling water for the probe cooling jacket was supplied by a gear pump and was fed to the brass manifold through high pressure plastic tubing. The use of plastic tubing permitted the freedom of movement noted previously.

Trace Injection System

Trace gas was injected into the plasma gas by means of a 10 inch, 18 gauge hypodermic needle. The needle was inserted

into the arc chamber horizontally, through the pressure tap in the plasma generator. A thermocouple gland was used to seal the pressure tap and the arc chamber from the surroundings. The tip of the needle was closed and a small hole drilled just back of the tip to permit injection of trace gas parallel to the direction of the argon flow. The entire length of the needle up to the hole was insulated from the thermocouple gland and the brass by a piece of plastic electrical spaghetti. The external needle mounting block was built with a screw drive mechanism, so that the needle could be moved in a direction parallel to its own axis and hence the axis of the pressure tap. Within the arc chamber, this movement was transverse to the direction of the gas flow, and permitted accurate positioning of the needle tip at any point in the annular region between the inner wall of the plasma generator main body and the outer wall of the cathode holder. Figure 10 shows the external mounting block alone, and in relation to the plasma generator with the insulated needle inserted in the thermocouple gland. The fixed vertical position of injection corresponded to a point slightly upstream of the arc itself.

Trace gas was supplied through a micrometer metering valve and a three-way solenoid valve. The solenoid valve was opened for trace gas injection with a toggle switch. This switch also triggered the time base of the dual trace oscilloscope which was used to monitor the time dependence

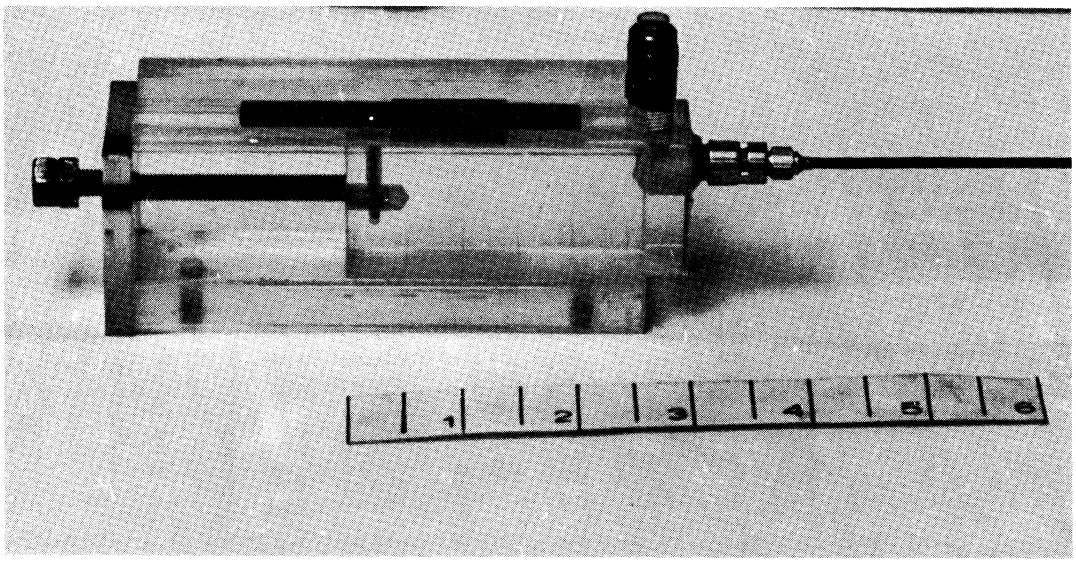

EXTERNAL MOUNTING BLOCK
WITH NEEDLE

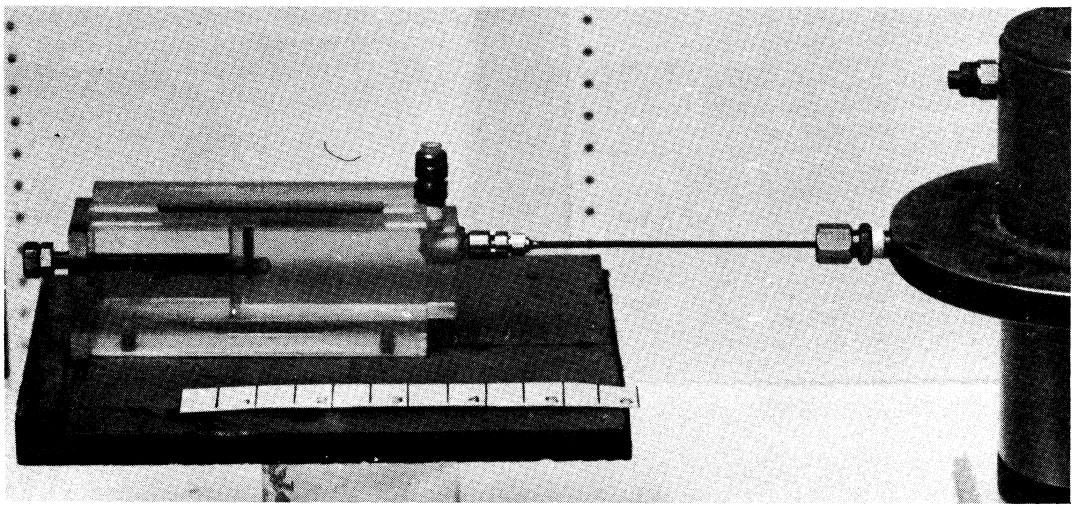

EXTERNAL MOUNTING BLOCK
AND PLASMA GENERATOR

FIG. 10. TRACE GAS INJECTION SYSTEM

of the photomultiplier voltage from the variable precision resistor. The photomultiplier signal was taken from the terminals of the precision resistor in order to bypass the microvolt amplifier because of its 3 second response time.

6. EXPERIMENTAL OPERATING PROCEDURES

The procedures involved in operating the experimental system described in the previous chapter are explained. Included in this discussion are operation of the plasma generator, precautionary safety measures, measurement of generator voltage and current fluctuations, trace gas measurement techniques, spectrographic measurement techniques, and the procedure for impact pressure measurements.

Plasma Generator Startup and Operation

Prior to each run, the copper anode was removed from the main body, and its inside wall cleaned with fine emery cloth. With the anode removed, a brass insert was used to fix the electrode separation at 5/16" and center the cathode tip, as shown below in Figure 11.

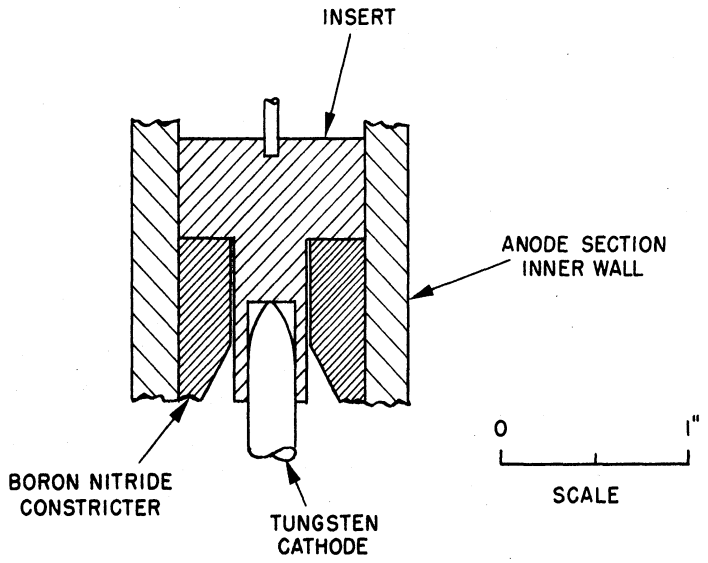

FIG. 11. ELECTRODE SPACING INSERT

After the anode was replaced and the retaining ring tightened, the quartz confining chamber was slipped into place and the cooling water turned on. The desired flow rates to the various channels were set and recorded. The argon flow was then begun, and the arc starter turned on to initiate the plasma. The main power supply was engaged and the arc starter immediately turned off. The argon flow rate was increased to an arbitrary maximum operating rate, which resulted in a highly diffuse flame. The power level as determined by the arc current was then adjusted and finally, the argon flow rate decreased to the desired value. Except in the early stages of this study, the flow rate and power level (current) were the only independent variables whose effects were investigated. If during a run a different operating condition was desired (i.e. - a new flow rate or power level or both), a change was achieved by first increasing the argon flow to obtain a diffuse flame, adjusting the current control if necessary, and then decreasing the flow to the desired value. This sequence of steps provided sufficient reproducibility of the torch operation and insured stability in the operation as indicated by the torch current and voltage. In most cases, these characteristics did not drift appreciably for the duration of a run, which sometimes was as long as two hours. The voltage and current, and the various cooling water flow rates and temperatures were recorded at intermediate times during the course of a run.

It should be mentioned that the terms power level and current are used interchangeably during much of this work. This requires some clarification. It was noted previously that the arc voltage could not be specified, but depended on the argon flow rate and the arc current for a given electrode separation. The arc current could be specified within the power capabilities of the power supply unit. The power supply unit had been adapted so that up to 500 amps could be delivered at a maximum potential of 80 volts. However, a fixed setting of the current control implied a fixed power level, and any change in voltage, accomplished for instance by adjusting the argon flow rate, was compensated for by a change in current of the opposite sign. Thus, a power level was specified when a current was selected for a given operating condition, and if the current control was not changed, the power level remained essentially constant.

Precautionary Safety Measures

Because of the high intensity radiation emitted by the plasma flame, several precautionary measures were required. The plasma jet was sufficiently bright to cause eye damage if viewed without eye protection. Welding goggles were worn during a run, and the plasma flame was observed directly only through an electrical welding helmet. Warning lights which

automatically turned on when the main power supply was engaged were installed at the laboratory entrances to prevent persons from entering without proper eye protection. During operation of the plasma generator, a buildup of ozone in the laboratory due to the ultraviolet radiation emitted by the plasma could be detected. An exhaust fan was used to aleviate this problem.

Voltage-Current Fluctuations

The a.c. variations in both plasma generator voltage and current were observed with the dual trace oscilloscope. The voltage fluctuation monitored was that between the two power cable terminals on the plasma generator (the mounting flange and the cathode holder) while the current fluctuation was monitored as the voltage variation across the terminals of the precision shunt. After initiation of the plasma, the desired power level was set with the argon flow rate at its arbitrary maximum value. An individual waveform or an x-y display was observed at the fixed current control setting while slowly decreasing the flow rate until a change was detected. The oscilloscope was then readied in the storage mode and a single sweep made of the fluctuation trace. A picture was taken of the stored waveform for permanent record and the corresponding operating conditions recorded. The argon flow rate was again decreased until another change was noted, and the sweep procedure repeated. In this

manner, three or four different waveforms were obtained while reducing the flow rate to the point where nozzle burnout occurred. The entire process was performed at several power levels, observing both voltage and current variations and an x-y display of voltage fluctuation vs current.

Trace Gas Measurements

As noted previously, trace gas was injected cocurrently into the plasma gas by means of a hypodermic needle inserted into the arc chamber through the pressure tap. Spectral lines of the trace gas were observed with the photomultiplier signal being monitored by the dual trace oscilloscope. Prior to plasma generator startup, the hypodermic needle was positioned well back in the pressure tap, completely removed from the chamber. After startup and achievement of the desired operation, the needle tip was inserted into the arc chamber to the required position. Injection of trace gas was initiated and the flow rate set at the maximum allowable value which would not affect the torch voltage or current. Next, the spectrograph wavelength setting was adjusted to observe the proper line of the trace gas, and the desired horizontal position of observation obtained. The injection of trace gas was discontinued, and the oscilloscope readied in in the storage mode. The solenoid valve was switched open,

simultaneously triggering the oscilloscope time base, which stored the time variation of the photomultiplier signal on the screen. Again, injection of the trace gas was discontinued. The vertical level of observation of the plasma was raised by changing the vertical vernier of the spectrograph scanning-condensing system. The position of trace on the oscilloscope screen was also changed. As above, the time variation of the photomultiplier signal was recorded at the new observation level as trace gas injection was initiated. Continuing in this manner, time variations of the photomultiplier signal at four or five vertical positions in the jet could be recorded on the screen and compared, to observe the passage of the trace gas through the jet. Pictures were taken of stored displays for a permanent record.

Spectrographic Measurements

It will be recalled from the description of the spectrographic system, that the photomultiplier current was passed through a precision resistor, the output voltage amplified, and the resulting signal either recorded or integrated. It was also noted that in analyzing the radiation at any position in the plasma, a region of the spectrum could be scanned at rates ranging from 1 to 500 Å/min. In practice, however, the scanning rate was limited by the time lag of the microvolt

amplifier. The argon lines observed for these measurements were approximately 7 to 8 Å in width, so that even moderate scanning rates would result in considerable attenuation of the true photomultiplier signal. An earlier calibration had shown that the percent attenuation of the input signal was appreciable at scanning rates greater than 10 Å/min (43). Although a check established that the value of the integral of a line profile is not as seriously affected by the scanning rate as is the actual shape of the profile, the limiting value of 10 Å was used for the spectral line measurements to be described below. The effect of scanning rate does not occur in obtaining continuum measurements, which are also described below. For all spectral measurements in this investigation, a slit height of 2.0 mm and a slit width of 20μ were used.

Line Measurements Line measurements were made in the following manner. After startup, the plasma was scanned horizontally at the desired vertical position with the wavelength set at the peak of the 4300 Å argon line. The photomultiplier signal indicated by the microvolt amplifier was observed during the scan to determine both the diameter of the luminous region and the position of maximum intensity. In nearly every case, the position of maximum intensity coincided with the centerline of the plasma generator to within $\pm$ 0.06 cm. From this information, the chord positions

were determined for each zone of the Abel inversion. The total number of steps to be used in the inversion was established prior to startup. Integrated line intensities could then be obtained at each of these chord positions.

With the wavelength drive set at the lower wavelength limit of the given line, the photomultiplier signal consisting of both plasma continuum and photomultiplier dark current contributions was integrated; simultaneously an integrator potentiometer was adjusted until the output voltage did not change with time. This meant that the net input signal to the integrator amplifier was zero and hence, the continuum-dark current signal was offset exactly. The integrator was reset and then, the wavelength drive and integrator initiated simultaneously. The integration was performed for the time required for the wavelength drive to advance to the upper limit of the given line at the 10 $\mathring{A}$/min scan rate. The integration times were approximately 45 seconds, and could be controlled to $\pm$ 0.1 sec. The integrator was then disengaged and the output voltage recorded. This voltage could be related to the integrated line intensity as explained in Appendix D. The horizontal drive of the scanning and condensing system was advanced to the next chord position, the integrator reset, and the wavelength drive set back to the lower limit of the line. The procedure was duplicated in the above manner at all chord positions to obtain the lateral

distribution of the spectral line intensities at the given vertical position. The lateral distribution of line intensity was then inverted to a radial emission distribution using the numerical technique presented previously and explained in detail in Appendix C.

Continuum Measurements Continuum intensities could have been recorded at each chord position where integrated intensities were obtained and then inverted. A slightly different technique was employed, however. Using the horizontal screw drive and beginning with a known reference position outside the luminous region, a lateral profile of the luminous region at a fixed vertical position was recorded by advancing the screw drive in small fixed steps until a final reference position also outside the luminous region on the opposite side was reached. From the sequence of step changes, the continuous profile of the argon continuum intensity at 5330 $\mathring{A}$ was constructed, and from this profile, the radius of the luminous zone determined. The profile was then folded about a center corresponding to the point of maximum lateral intensity, and the lateral intensity for each inversion zone determined. The advantage of such a technique lies not only in the simpler mechanics and shorter time required to obtain the data, but also in the fact that the number of inversion zones is not fixed in

advance. Thus in analyzing a profile, if an inversion of fewer zones proved inadequate, a more detailed inversion could be performed using the same data without having to make new measurements. As for lateral line intensities, the numerical inversion technique was used to transform the lateral continuum intensity distribution into a radial emission distribution.

Impact Pressure Measurements

Since the lateral drive of the three-dimensional probe traversing mechanism was equipped with an electric motor and belt drive, a continuous impact pressure profile could be obtained in the plasma jet along the diameter or any chord of the confining chamber at a given vertical level. Prior to obtaining profiles, the pressure near the confining chamber wall on the diameter was recorded for the vertical position of interest after the desired operation of the plasma generator had been achieved. Next the lateral position of the probe was manually advanced to a reference point just outside the plasma flame. Early runs had shown that the pressure measurements could be restricted to a region near the centerline of the nozzle and confining chamber. The continuous drive was engaged, and initiated through an electric timer. The probe passed through the flame until it

reached a point equally removed from the centerline on the opposite side. A 1.5 minute traverse was required. The timer shut off the probe drive automatically. The chart drive on the strip chart recorder was started and stopped simultaneously with the probe drive, so that a continuous impact pressure profile was recorded for the diametrical traverse. Following this traverse, the continuous drive was disengaged and the lateral position of the probe returned to its starting position. If a chord traverse was desired, an adjustment in depth position was made so that the desired traverse could be achieved. The continuous drive was again engaged and the traverse procedure repeated. When chord traverses were made, a predetermined spacing about the diameter was used such that an equal number of profiles were obtained on each side of the diameter.

As the probe moved through the flame on the diametrical traverse, the probe tip was focused on the top of the spectrograph slit. In this way, the vertical position for spectrographic measurements corresponded to the region just upstream of the probe tip. After the pressure traverses had been completed, the probe was removed from the vicinity of the flame and the required spectrographic measurements were made using procedures described previously. The probe was then placed at a new vertical position, the wall pressure measured,

and the entire process of recording impact pressure profiles and making spectrographic measurements repeated. During the course of a run, measurements were made at several vertical positions in the luminous region of the plasma jet. Usually, pressure profiles were also obtained at one position above the luminous region of the jet.

7. EXPERIMENTAL RESULTS AND ANALYSIS

The results of the experimental program are presented and analyzed. General observations on the operation of the plasma generator are indicated first. Voltage and current fluctuations associated with the plasma generator are considered as a possible aid for characterizing flow patterns. The trace gas technique for direct measurement of plasma jet velocities is evaluated. Measurements made to determine the thermal condition of the plasma are analyzed. Velocity profiles obtained from detailed sets of impact pressure measurements at a fixed power level are presented. The effect of input power level on the operation of the plasma generator and on the centerline velocities and temperatures in the jet is shown. Finally, a Reynolds number correlation for distinguishing flow patterns in the plasma jet is given.

General Observations

Before presenting specific details on the outcome of the various phases of this study, it is worthwhile to indicate some general observations on the operation of the plasma generator. Such observations could be most valuable to future researchers in this field.

Anode Configuration In the initial phases of development of the plasma generator nozzle configuration, the exit section

of the anode was made diverging. With such a configuration, the portion of the anode adjacent to the boron nitride constrictor was made straight, which forced the arc to terminate in this region. The anode then diverged to the exit diameter. Using an anode of this geometry having a restricted arc termination area, the effect was that of a gas flowing through a converging-diverging nozzle with the arc coincidentally terminating in the nozzle throat. Various tapers for the diverging section were experimented with. The same general effect was observed with this type of anode, regardless of the taper. The plasma generator could be operated at slightly greater electrode separations than with the eventual straight bore anode. As a result of the increased separation, the generator voltage increased and hence, higher efficiency for the transfer of electrical energy to the argon was achieved. For example, efficiencies in the range of 48% to 52% were attained at electrode separations of 7/16 to 1/2 inch for an argon flow rate of approximately 35 gm/min. It should be noted that these efficiencies are based on electrode cooling water temperature rises. This method of evaluating plasma generator efficiency had been checked, and yielded total gas energy contents which agreed to within 3% when the total gas calorimeter employed by Chludzinski (15) and Smith (52) was used to measure the argon

energy content. Despite the favorable energy transfer efficiency, the plasma flame was quite difficult to center and control when the diverging anode was used. Not only did the axis of the flame deviate from the nozzle axis, but operating conditions at the same current-control setting, separation, and argon flow rate could not be duplicated from one run to the next. For this reason, the diverging anode was replaced with the simpler, straight-bore anode. Using this type of anode, the electrode separation had to be reduced to maintain flame stability, and for the duration of this study, was held constant at 5/16 inch. Because of the reduced separation, efficiencies ranging from only 34% to 40% could be attained at the previously noted 35 gm/min argon flow rate. However, the plasma flame remained generally on center and the operating conditions were more nearly reproducible from run to run.

Also during the early phases of the investigation, the inner diameter of the constrictor and anode was varied. Diameters from 0.312" to 0.500" were tested. The smaller diameter anodes and constrictors resulted in more stable plasma flames, but sustained greater damage in the area where the arc attached. The larger diameter inserts sustained less damage, but yielded plasmas that were more difficult to center and control. The 0.406" diameter finally selected represented an optimum

between dependable operation and reduced electrode wear. Inserts of this diameter could withstand approximately 5 to 6 hours of cumulative operating time before damage significant to necessitate replacement was incurred. Use of the 0.406" anodes resulted in a confining chamber diameter to jet diameter ratio of approximately 7.5.

Cathode Geometry Initially the tungsten cathode was ground to a hemispherical tip. Later a blunt, ballistic tip was tried, and finally a blunt point configuration was used. The blunt point provided the most reliable operation. After several hours of operation, the point became heavily frosted and required polishing. A tantalum cathode was used once, but this did not prove fruitful because the tantalum overheated and melted.

Electrode Concentricity The electrode concentricity was found to be very critical to the operation of the plasma generator. Before the "spacer-insert" was used to gap and center the cathode, it had been found that very poor gas distribution was being obtained at the exit plane of the nozzle in cold argon flow. This channeling of the flow caused non-uniform heating of the gas and preferential attachment of the arc to one spot at the anode upon plasma startup. As a result, the center of the luminous region did not coincide with

the geometric center of the jet and the anode lifetime was sharply reduced. On occasion the flame made sporadic jumps from one position to another. After use of the "spacer insert" was begun, this problem was eliminated so that the position of maximum spectral intensity in the jet, as noted previously, coincided with the center axis of the plasma generator in most cases to within $\pm$ 0.06 cm.

Characteristic Operating Modes By proper adjustment of the argon flow rate and the arc current, three distinct types of jet flame could be exhausted by the plasma generator. These three types of jet were labeled laminar, transitional, and turbulent, and the geometrical shape of each is sketched below in Figure 12. From left to right respectively, they occurred as the argon flow rate was increased above the minimum value required to prevent anode burnout at a given current, although in actual practice, they were obtained by starting with a turbulent flame at a high flow rate and then gradually reducing the argon flow.

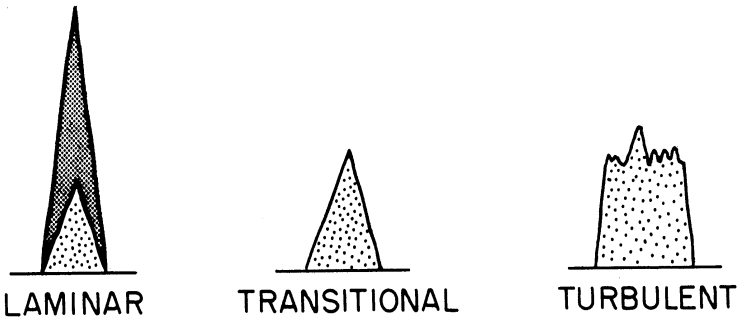

FIG. 12. GEOMETRICAL SHAPE OF EACH TYPE OF PLASMA JET

The laminar jet was characterized by an intensely bright, well defined conical core and a long diffuse plume or tail flame. The transitional jet had a bright well defined core somewhat larger than that of the laminar flame, but without a plume. The turbulent jet had a diffuse, ill-defined structure. Luminous fluctuations existed in each of these jets but were most pronounced in the turbulent case. The turbulent jet was also quite noisy, while the laminar and transitional jets were relatively quiet. Similar indentifying characteristics for the laminar and turbulent modes have been reported by Smith (52), Sherman (49), Incropera (31), and Cabannes (11). While these and other investigators were familiar with the laminar and turbulent jets, only Incropera noted observing the transitional jet. No other qualitative or quantitative data on this regime were found in the literature.

At low currents a laminar jet could not always be obtained because in decreasing the argon flow rate, the transition from the transitional regime to anode burnout occurred over a very narrow range in flow rate. Cabannes (12) observed somewhat similar behavior. Nozzle burnout was considered to occur when traces of copper green appeared in the plasma flame. Severe anode damage in the form of pits or shiny molten spots was observed following shutdown after the appearance

of the green flame coloration.

At lower argon flow rates, a very unstable operating mode occasionally arose. This behavior was characterized by a diffuse flame and a very intense screech. It occurred at nearly isolated flow rates. It was not reproducible, and was most likely due to blowing and restriking of the arc.

Overall Performance The plasma generator performed in the manner to be anticipated of one employing a constricted arc configuration. The arc voltage increased with argon flow rate at a fixed power level, and also increased with current (power level) at a fixed argon flow rate. As noted previously, the arc voltage increased with electrode separation when this variable was investigated during the initial runs. As would be expected, the efficiency of transfer of electrical energy to the argon also followed the above pattern of behavior. The pressure in the arc chamber was essentially atmospheric when cold argon was flowing through the generator prior to startup, and increased to about 0.1 psig after the arc had been initiated. This indicates that the arc in effect, acted as a pump.

For the experimental results to be presented, the plasma generator was operated at arc currents corresponding to an input power range of 4.6 to 13.2 kw, with argon flow rates of 11 to 45 gm/min. The energy transfer efficiency

varied between 20 and 44% over this range of operating conditions. At the lower input power levels, the argon flow rate could actually be reduced to less than 10 gm/min without reaching anode burnout. No results were obtained at this low flow rate because prolonged operation under these conditions was not deemed desireable. Stable operation of the plasma generator generally was more difficult to maintain at the lower flow rates, where conditions could not always be reproduced.

Voltage-Current Fluctuations

The a.c. components of voltage and current were observed with the dual trace oscilloscope as noted previously while operating the plasma generator in each of the three characteristic modes. It will be recalled that the voltage fluctuation was that taken from the power cable terminals on the plasma generator and the current fluctuation was monitored as the voltage variation across the precision shunt. Voltage fluctuations were compared to the open circuit voltage ripple of the power supply, which was found to be a 360 cycle/sec ripple with a peak to peak rms variation of 9.5 volts at an open circuit voltage of 83.3 volts. A picture of this waveform as stored on the oscilloscope screen is shown in Figure 13. The scale of the superimposed grid is noted. The 360 cycle/sec

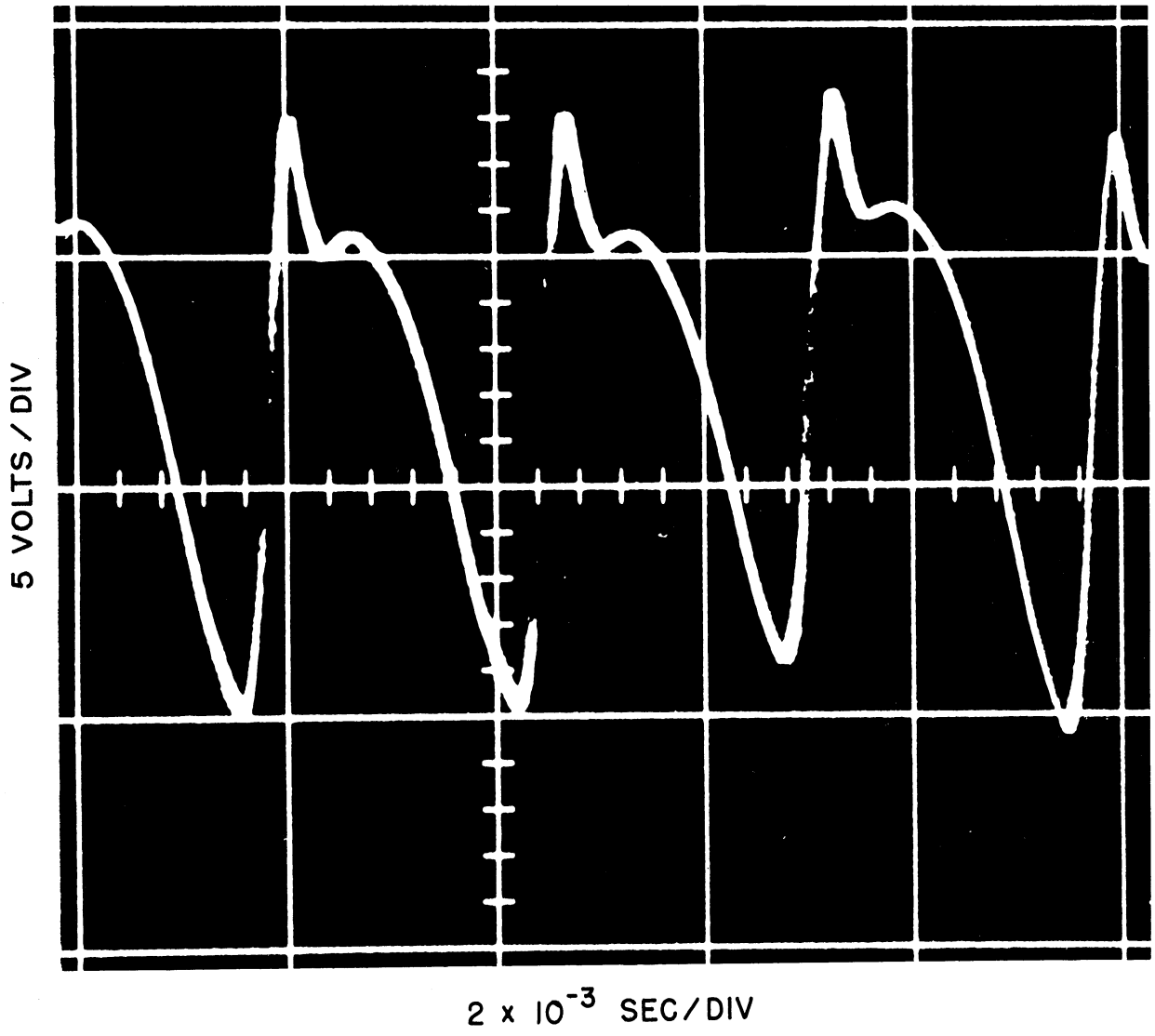

OPEN CIRCUIT VOLTAGE : 83.3 VOLTS

FIG. 13. OPEN CIRCUIT VOLTAGE FLUCTUATION OF THE POWER SUPPLY UNIT

ripple is that expected in the output of a three phase full wave rectifier. The distortion on the ascending portion of the waveform is due to the saturable reactor current control.

Results It was found that each of the characteristic types of plasma jets exhibited its own distinct voltage ripple. A picture of each waveform taken from the oscilloscope screen is shown in Figure 14. These results were obtained as a function of flow rate at a fixed input power level. The actual operating conditions corresponding to each waveform are indicated, as is the grid scale. In each case, the frequency of the predominant waveform is 360 cycle/sec but the magnitude of the distortion and the position of this irregularity on the waveform is different. Also included in Figure 14 is a picture of the waveform observed for the unstable operating mode. Current fluctuations were found to be the same for each characteristic jet. The x-y a.c. voltage component versus current pattern was observed to differ for each mode, and pictures of these patterns are shown in Figure 15. As before, the actual plasma generator operating conditions are indicated for each waveform. The pattern for the unstable mode is not included in Figure 15.

Because each operating mode exhibited its own characteristic voltage ripple and x-y voltage variation-current pattern, the possibility of using these fluctuations to define the operating limits of each mode was investigated. The

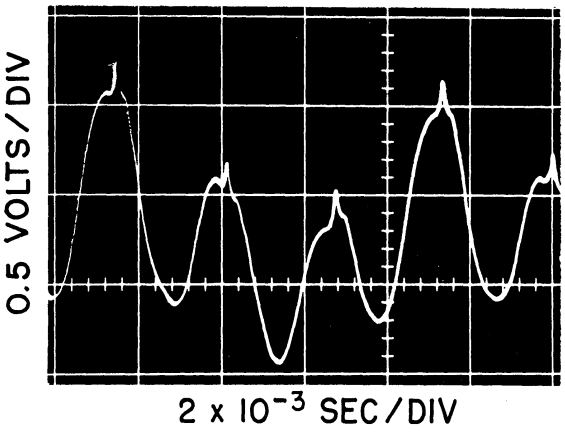

LAMINAR MODE

15.7 gm/min
26.8 volts
492 amps

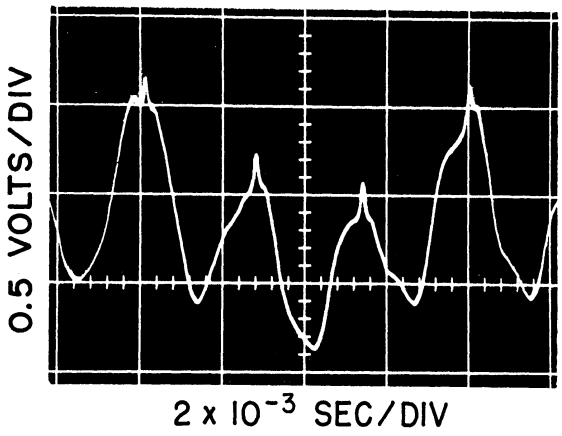

TRANSITIONAL MODE

26.2 gm/min
27.7 volts
465 amps

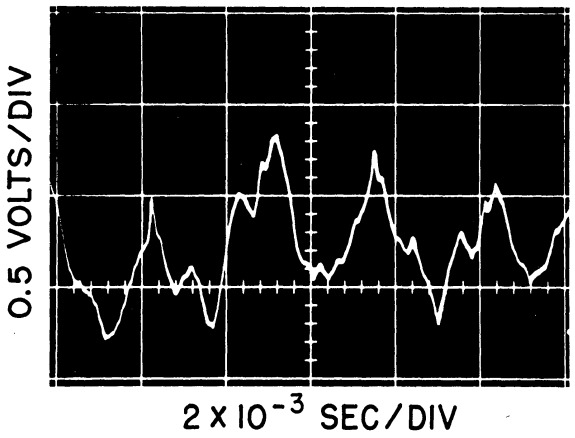

TURBULENT MODE

44.8 gm/min
30.0 volts
432 amps

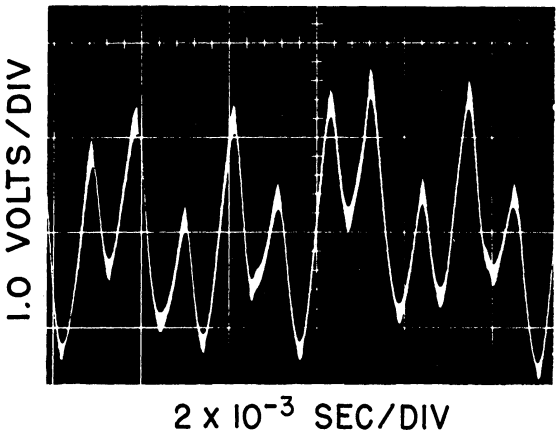

UNSTABLE MODE

18.7 gm/min
23.8 volts
322 amps

FIG. 14. PLASMA GENERATOR VOLTAGE FLUCTUATIONS FOR THE VARIOUS OPERATING MODES

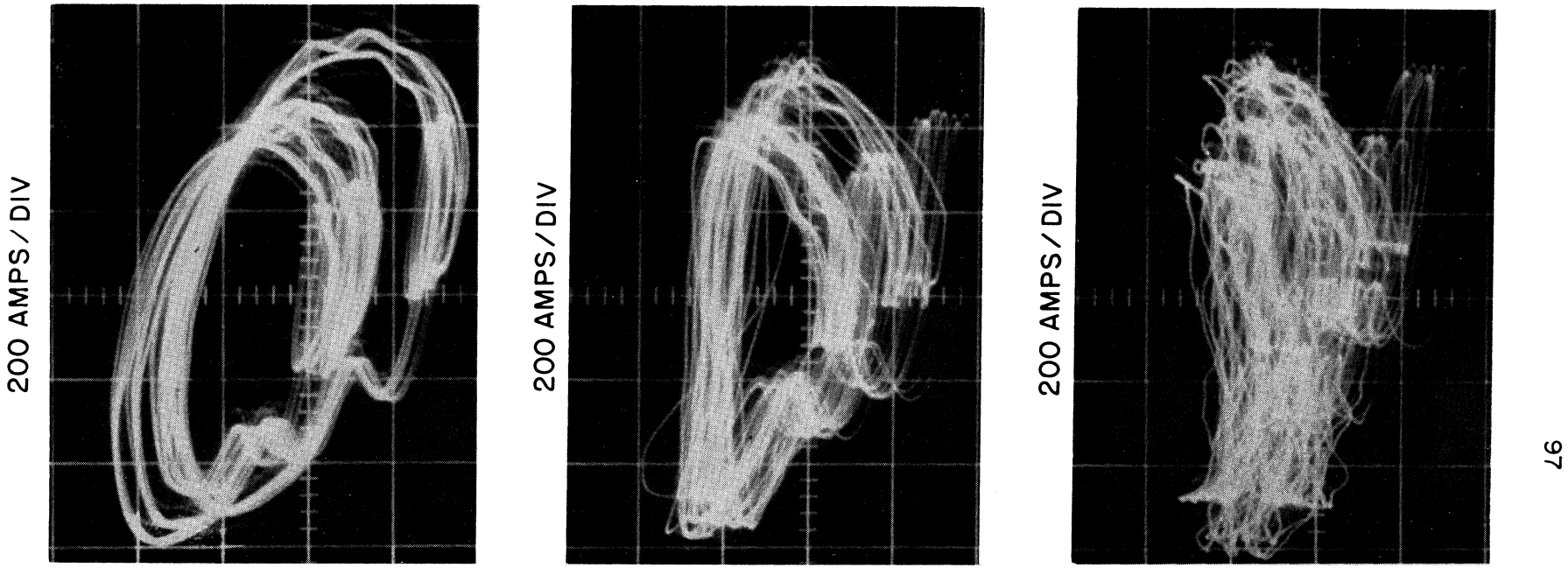

LAMINAR MODE
11.2 gm/min
24.7 volts
360 amps

TRANSITIONAL MODE
28.0 gm/min
26.3 volts
328 amps

TURBULENT MODE
44.8 gm/min
28.1 volts
296 amps

FIG. 15. PLASMA GENERATOR VOLTAGE FLUCTUATION–CURRENT PATTERNS FOR THE VARIOUS OPERATING MODES

voltage fluctuation and x-y pattern were obtained as a function of decreasing argon flow rate at three input power levels using the procedure previously described. It was found that in progressing from one operating mode to another, there was only a very gradual transition in the voltage waveform or the x-y voltage variation-current plot. It was concluded that while the voltage fluctuation waveform or the voltage-current pattern could be used to differentiate one mode of operation from another, this type of measurement was not capable of defining the transition point between two operating modes. The transitions, therefore, had to be determined visually.

Trace Gas Technique

Trace gas was injected into the main stream argon in an attempt to spectroscopically measure time delays as the trace gas passed from one level to another through the plasma jet. If these time delays could be resolved, a direct measure of the plasma velocity would be available without disturbing the jet flow. It will be recalled that the trace gas was injected cocurrently into the plasma gas just upstream of the arc by means of a hypodermic needle inserted through the pressure tap. The needle tip was in the annulus between the plasma generator inner wall and the cathode holder. Injection was begun or discontinued with a solenoid valve, and the injection rate controlled with a micrometer metering valve.

Gas Selection It was first necessary to find a trace gas whose spectral lines were strong enough to be detected at the low concentrations required to prevent disturbing the overall operation of the plasma generator. Helium, hydrogen, nitrogen, and a nitrogen-argon mixture proved unsuccessful. Krypton was found to be satisfactory.

Injection of helium did not affect the plasma jet at injection rates up to approximately 5% of the argon flow. However, when the spectrum was scanned in the vicinity of three wavelengths corresponding to strong helium lines - 4471 Å, 5016 Å, and 5876 Å - none of these lines were detected at any position in the plasma jet. In retrospect, this was to be expected. The helium would not have been sufficiently excited because its lowest excitation energy levels are considerably greater than those of excited argon ions, and no lines of excited argon ions could be detected.

Injection of both hydrogen and nitrogen was unsatisfactory because even the lowest injection rates of either of these gases caused drastic disturbances in the operation of the plasma generator. Only immeasurably low injection rates could be used. While injecting hydrogen, the $H\beta$ line (4861 Å) was detected, but the jet began to exhibit the blue-green copper

coloration associated with anode burnout after only a short period of operation. After shutdown, the anode showed significant damage. When nitrogen was injected, a spectrum could not be obtained before the flame turned blue-green. After shutdown the electrode damage was found to be even more severe than when hydrogen was injected.

To alleviate the problems of plasma jet disturbances and electrode damage, a 60%-40% mixture of argon and nitrogen was tried as the trace gas. A somewhat higher injection rate than used for helium injection could be achieved before the plasma flame was altered. However, when segments of the spectrum in the 3350 Å to 4250 Å range were scanned at various positions in the jet, none of the lines of either the 0,0 band of the second positive system of N_2 or the 0,0 band of the first negative system of N_2^+ were observed.

After the unsuccessful experiences with the gases cited above, krypton was used as the trace gas. Krypton was chosen because its excitation energies and ionization potential are lower than those of argon, and because several small cylinders were available. Krypton could be injected at rates sufficiently high that three krypton lines could be observed in the plasma jet without affecting the operation of the plasma generator. The 4274 Å and 5570 Å krypton lines were in close proximity to stronger argon lines, 4272 Å and 5572 Å respectively,

so that use of these lines was not considered further. The 5870 Å krypton line had no neighboring argon lines, and was used for the remainder of these experiments.

Point of Injection After the trace gas had been chosen and its spectral line to be observed, selected, it was necessary to investigate the effect of the position of the hypodermic needle in the arc chamber annulus on the horizontal distribution of krypton line intensity at a fixed vertical level in the plasma jet. The 5870 Å krypton line was not scanned, but rather, the wavelength adjustment of the spectrograph was set so that the maximum signal at the line peak was continuously observed. The krypton injection rate was fixed at the maximum allowable value which would not disturb the plasma generator operating conditions. This injection rate was less than 5% of the main stream argon flow rate. The position of the needle tip was varied over a range of 0.275", to within 1/16" of each wall of the annulus. (The inner and outer diameters of the annulus at the point of injection were 0.500" and 1.300 respectively.) At each position of the needle tip in the annulus, the plasma jet was scanned horizontally to locate the position of maximum krypton intensity. Regardless of the position of the needle tip, the position of maximum intensity was essentially constant, and coincided with the position of maximum argon continuum intensity to within

$\pm$ 0.01 cm. As a result of this, the position of the needle tip was then fixed in the center of the annulus, and the horizontal point of observation fixed at the position of maximum argon continuum intensity.

Results Having defined all parameters associated with the method, measurements were made in the manner described previously. Time variations of the photomultiplier signal from the instant trace gas injection began were observed with the dual trace oscilloscope at four or five vertical positions in the plasma flame. A photograph of typical stored traces for a transitional flame is shown in Figure 16. The top trace was observed at the nozzle exit plane, and each succeeding downward trace corresponds to an upward vertical step in the plasma jet. The superimposed x and y grids correspond to 20×10^{-3} sec and 200×10^{-6} volts per major division respectively. On each trace the initial signal is that of argon continuum at 5870 $\mathring{A}$, and this signal increases (shifts downward) from its initial (or base) value as the krypton reaches the level of observation in the plasma. The overall magnitude of the signal shift increases as the level of observation moves upward through the plasma flame. Traces 3 and 4 correspond to the vertical positions of maximum radiation intensity. The results are quite disappointing, however, for it can be seen that

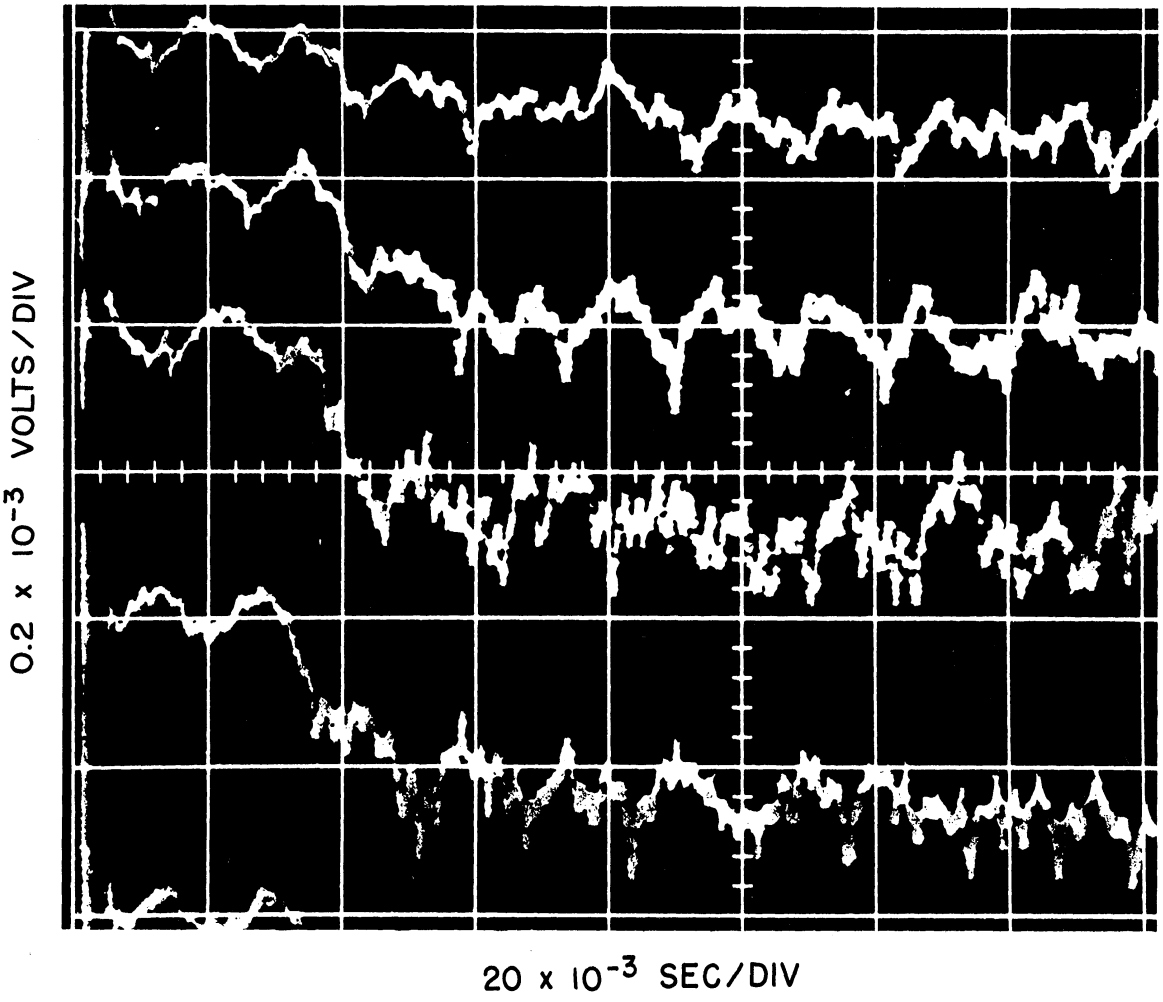

FIG. 16. PHOTOMULTIPLIER SIGNAL FLUCTUATIONS DUE TO THE KRYPTON MOVEMENT THROUGH THE TRANSITIONAL PLASMA JET

the photomultiplier signal was of such low magnitude that inherent random photomultiplier noise prevents resolution of the intensity variations into time delays.

Possible modifications to the system to improve the signal quality were investigated, but proved unsatisfactory. The krypton concentration could not be increased because the injection rate used was the maximum allowable value which would not alter the operation of the plasma generator. The value of the precision resistor through which the multiplier phototube current passed, could have been increased, but both the noise and the signal would have been amplified to the same extent. A capacitor had been installed in parallel with the precision resistor to eliminate the high frequency contribution to the noise. The most sensitive oscilloscope scale (100×10^{-6} volts/div) was tried, but the noise interference was even more severe. All cables had been checked, and were properly shielded to ground. Finally, use of an 1P21 multiplier phototube rather than an 1P28 was tried, but the 1P28 was found to yield a stronger signal with less noise when a standard source was observed at 5870 Å. Thus, the results presented represent the optimum operation of the system. It was concluded then that while passage of the krypton through the plasma jet could be observed qualitatively, no meaningful information could be obtained from the data. For this reason, the trace gas technique was

abandoned and the problem of relating time delays to velocities in the jet was not considered. Thus, the plasma jet velocities had to be determined indirectly by measuring impact pressures.

Plasma Temperature Analysis

The temperature distribution in the plasma must be known in order to calculate velocities from measured impact pressures. Temperatures in a plasma jet can be obtained by spectroscopically analyzing radiation emitted by the jet. The theory associated with several methods of relating temperature to the intensity of observed radiation was presented in Chapter 4. Not only was it necessary to select a specific spectrographic technique, but in the process of choosing this technique, the thermal condition of the plasma had to be considered. It will be recalled from the earlier discussion of thermodynamic equilibrium in a plasma that the possibility exists of there being several different temperatures in the plasma if it is not in local thermodynamic equilibrium. While plasmas at atmospheric pressure are often assumed to exhibit this characteristic, in this investigation its existence was ascertained experimentally by measuring and comparing several excitation temperatures and the electron temperature. From these comparisons, the technique to be used during

the remainder of the study was also selected.

Scope of Measurements The experimental procedure to obtain a complete set of necessary data was quite lengthy. A run of 2½ hours duration was required. For this reason, the measurements were made only at the nozzle exit plane while operating the plasma generator in the transitional mode at an intermediate input power level. Excitation temperatures corresponding to five argon lines and the electron temperature corresponding to the continuum radiation were obtained at five radial positions in the jet by measuring and inverting chord intensities using the procedures previously described. At each position the temperatures were compared and Boltzmann plots were constructed. The argon lines employed were the 4158 Å, 4181 Å, 4259 Å, 4300 Å, and 4510 Å lines. These lines were used because they were of sufficient strength that they could be observed throughout the entire plasma jet. The spectral constants for these lines are tabulated in Appendix B. The continuum emission was observed at 5330 Å.

Prior to obtaining the set of data, an attempt was made to reduce the experimental run time by measuring a series of peak heights and areas for each of the argon lines. It was hoped that only peak heights would need to be observed and integrations of the lines would not be necessary. However a meaningful correlation between peak height and line area

could not be resolved for any of the lines, so that integrations had to be performed for each line at each radial position during the run.

Results The temperature corresponding to each line and the continuum, and the average of these temperatures is presented for each radial position in Table I. The characteristic length for the dimensionless radius is the anode radius, 0.516 cm. The maximum radial position corresponds to the point where the chord intensity of the 4300 Å argon line had decreased to 1% of its maximum value. At each position, the temperatures are seen to agree quite well, the maximum deviation from the average being less than 2%. Based on fluctuations of the integrated photomultiplier signal (± 9%), possible errors in the integrator calibration using the tungsten filament lamp as an absolute intensity reference (± 12%), possible errors in the measured transmittance of the plasma jet confining chamber (± 5%), and errors arising in the outer inversion zones from the approximations associated with the numerical inversion technique (± 8%), the maximum uncertainty in the temperatures obtained from the experimentally measured values of line emission coefficients is estimated to be ± 2.5%. The theory is considered accurate to within ± 1%, since the transition probabilities of the argon lines used are only known to within ± 15%. Experimental uncertainties for the continuum

Table I

Comparison of Measured Plasma Temperatures

Transitional Plasma Jet

Argon Flow Rate: 24.0 gm/min Average Input Power: 7.21 kw

Temperature in ^{o}K

	Wavelength of Observed Radiation - $\mathring{A}$						Average
	4158	4181	4259	4300	4510	5330	
Radial Position							
0 ($r/R = 0.000$)	10805	10730	10680	10780	10820	10700	10763
1 ($r/R = 0.239$)	10730	10710	10620	10715	10760	10640	10707
2 ($r/R = 0.479$)	10500	10480	10400	10480	10525	10425	10477
3 ($r/R = 0.718$)	9890	9880	9815	9900	9975	9890	9892
4 ($r/R = 0.957$)	9160	9040	9060	9050	9290	9210	9120

intensity method include variations in the intensity itself ($\pm$ 7%), and the calibration ($\pm$ 12%), transmittance ($\pm$ 5%), and inversion ($\pm$ 8%) errors noted above. As a result, it is estimated that the maximum uncertainty in the electron temperature is $\pm$ 1.7%. The theory of continuum emission is considered accurate to within $\pm$ 0.6%, since the quantuum mechanical correction factor is known to within $\pm$ 10%.

After obtaining temperatures from the radial profiles of the various line emission coefficients, Boltzmann plots were prepared for each radial position to see if a Boltzmann distribution could be assigned to the number densities of the excited states. It will be recalled that for a given temperature, a Boltzmann plot is a semilog plot of $\frac{\epsilon_{line}\lambda}{g_u A_{ul}}$ versus E_u and is a straight line with slope $-\frac{1}{kT}$ if indeed the plasma is in local thermodynamic equilibrium. The argon lines used possess different excitation energies, but these energies are narrowly spaced in the region near 14.50 ev, and somewhat removed from the ionization energy of 15.76 ev. Lines of higher excitation energy were not of sufficient strength to be observed throughout the plasma. Thus, while excitation temperatures were easily obtained and Boltzmann plots readily prepared, it was anticipated that any scatter in the values

of $\frac{\varepsilon_{line}\lambda}{g_u A_{ul}}$ would cause small variations in the slope of the line and result in large variations in the Boltzmann temperature. As expected, this did occur and at each radial position, a least-square straight line fit yielded a slope whose corresponding Boltzmann temperature was significantly lower than the temperatures presented in Table I. To overcome this difficulty, an alternate approach was undertaken. A confidence limit was assigned to each of the five experimental values of $\frac{\varepsilon_{line}\lambda}{g_u A_{ul}}$ at a given radial position, and a straight line with a slope corresponding to the average temperature for that position (from Table I) was passed through the bands defined by the confidence limit. If the line passed through each of the five bands, it was concluded that a Boltzmann distribution existed at that particular position, and the temperature specifying this distribution was essentially the same as the electron temperature and the individual excitation temperatures. It could then be further concluded that the condition of local thermodynamic equilibrium prevailed at that position.

Figure 17 shows the modified Boltzmann plots for the five radial positions investigated. Confidence limits of $\pm$ 10% were assigned to the values of $\frac{\varepsilon_{line}\lambda}{g_u A_{ul}}$ for positions 0, 1, and 2, and limits of $\pm$ 15% were used for positions 3 and 4. Based on the experimental uncertainties associated with ε_{line} which were cited earlier, and the uncertainty in the transition

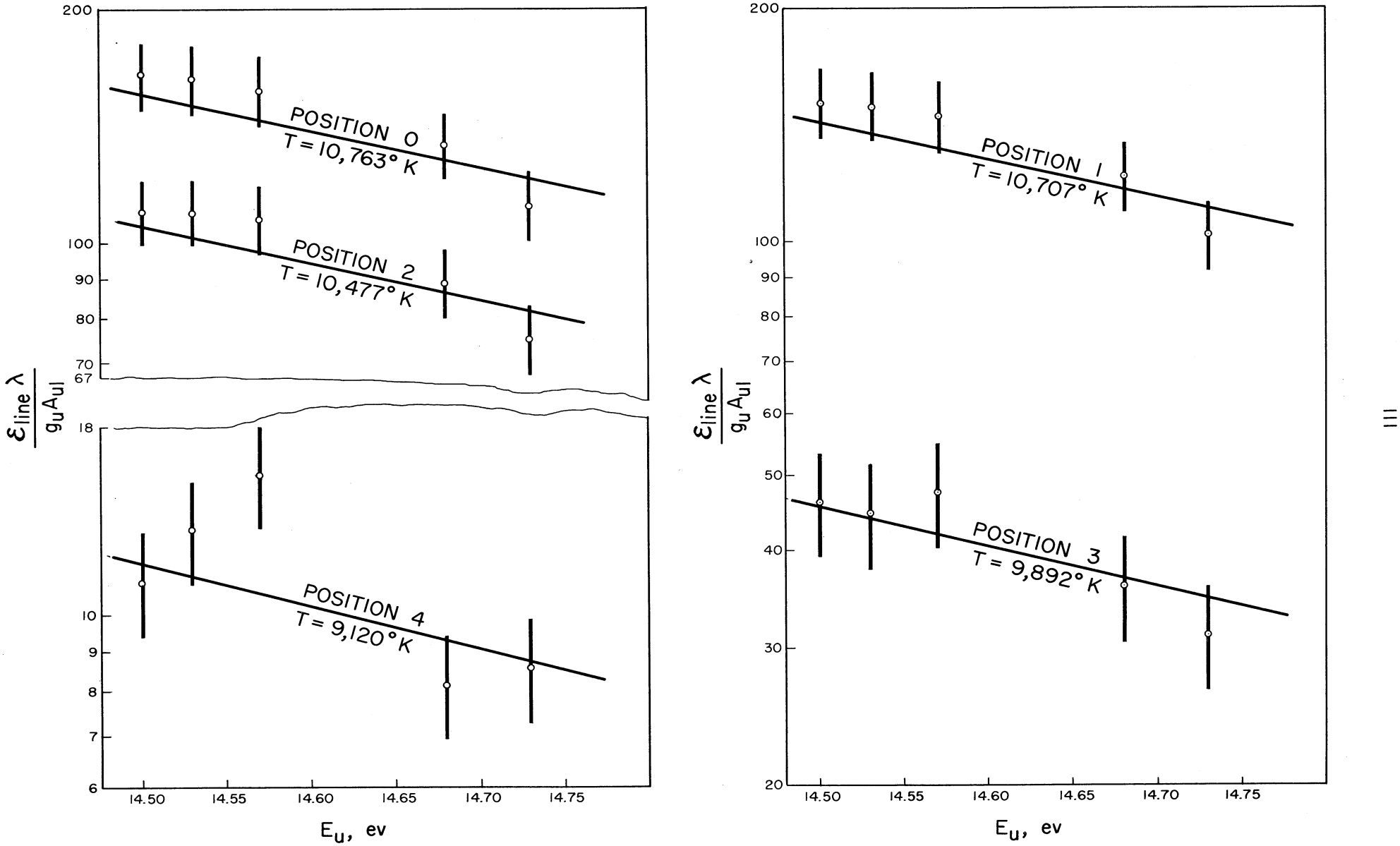

FIG. 17. MODIFIED BOLTZMANN PLOTS AT VARIOUS RADIAL POSITIONS IN THE TRANSITIONAL PLASMA JET

probability which was also noted, these confidence limits are felt to be conservative. In fact at position 0, the value of $\mathcal{E}_{line}$ for the 4300 Å line was measured twice during the run, and the slight variation observed showed the confidence limits chosen to be realistic.

From Figure 17, it can be seen that at the four internal positions in the plasma the line determined by the average temperature passes through each band of $\frac{\mathcal{E}_{line}\lambda}{g_u A_{ul}}$, so that local thermodynamic equilibrium exists at these positions. At the fringe of the jet where fluctuations are most severe, the line determined by the average temperature passes through four of the five bands. Thus thermodynamic equilibrium exists throughout the plasma and any excitation temperature or the electron temperature corresponds to the true plasma temperature. Since the procedure for measuring continuum intensities is the simplest and because there is the least experimental uncertainty in resolving the associated electron temperature, this method was used to obtain the plasma temperature for the remainder of the investigation.

Detailed Velocity Study

Impact pressure distributions and continuum intensity profiles were measured in the plasma jet so that velocities in the jet could be calculated. A series of detailed

measurements was made at an intermediate power level to investigate the effect of argon flow rate on the plasma jet velocities. Measurements were also made in cold flow to demonstrate the effect of flow rate on velocities.

The water-cooled probe was used to measure pressures in the plasma jet. It will be recalled that the lateral drive of the three dimensional traversing mechanism used to position the probe had been coupled with an electric motor so that continuous pressure profiles could be obtained in the jet along a diameter or chord. Continuum chord intensities could be measured spectrographically and inverted numerically to obtain the radial distribution of emission coefficients, from which the temperature profile could be determined. The probe was also used to measure pressure profiles in the jet during cold flow. Temperature measurements were not necessary in this case.

Scope of Measurements The detailed measurements of impact pressures and continuum chord intensities in the plasma jet were made at an intermediate power level for flow rates corresponding to the turbulent and transitional operating modes. For the laminar mode, detailed measurements were not made because at the low flow rate corresponding to this mode, a stable operation could not be maintained for the length of time required to obtain the necessary data. A run of 1½ to

2 hours duration was required for each mode. Only shorter runs to investigate the effect of power (to be discussed later) could be made for the laminar mode. Smith (52) and Sherman (49) encountered similar difficulty with stability while operating in the laminar mode.

For the fixed flow rate corresponding to a specified operating mode, the detailed measurements consisted of obtaining the pressure at the confining chamber wall, continuous diametrical and chord profiles of impact pressure, and a profile of the continuum chord intensity at four vertical positions in the plasma. The procedures required to obtain the data have been described previously. It will be recalled that the impact pressure profiles were begun at a reference position outside the region of measurable pressures on one side of the jet flame, and continued to a second reference position outside the pressure region on the opposite side. This same approach was used in measuring "step" chord profiles of the continuum intensity. Four equidistant chord profiles of impact pressure were obtained at each level, two on each side of the diameter. In making the step measurements of the continuum chord intensity, the luminous portion of the jet was divided into 32 segments. The four vertical positions were at distances 1, 2, 3, and 4 nozzle radii downstream of the plasma generator exit plane. Although pressures could have been measured closer to the exit plane,

the initial position represented the point at which the luminous region upstream of the probe tip was of sufficient volume that its image on the slit of the spectrograph covered the entire slit. A smaller slit height could have been used so that a position nearer the exit plane could have been investigated, but this would have eliminated a position of observation in the less luminous regions of the tail flame. Beyond 4 nozzle radii downstream of the exit plane, the intensity of emitted radiation had decayed to the extent that meaningful measurements could not be obtained. A set of diametrical and chord impact pressure profiles was obtained beyond the luminous region of the jet, at a downstream position of 8 nozzle radii. Diametrical and chord profiles of impact pressure and the wall pressure were also obtained in cold flow at the flow rates corresponding to the transitional and turbulent plasma jets, and at the flow rate corresponding to a laminar plasma jet. These cold flow measurements were made at the same four positions downstream of the generator exit plane as were the plasma measurements - i.e, 1, 2, 3, and 4 nozzle radii. As noted previously, no temperature measurements were required in this case.

Methods of Data Resolution Several important aspects in the resolution of the raw data into temperatures and velocities should be mentioned before considering the specific results.

Abel Inversion

When reconstructing the "step" chord profiles of the continuum intensity for inversion into the radial distribution of emission coefficents, the chord profiles in most cases were found to be asymmetric. While this was not always a serious problem since symmetry could be assumed upon smoothing the chord profiles, a method had to be established to handle the cases where asymmetry was serious. For consistency this method was used in inverting all chord profiles.

The chord profile was divided into two sections at the point of maximum intensity, and each section inverted as if it corresponded to a symmetric radial distribution. Whenever the position of the maximum was removed from the nozzle centerline, a separate radius and hence a different number of inversion zones was used in inverting each section. The combined number of inversion zones used for both sections was 32 as previously noted, and most often the split was 17-15. The two "radial" distributions obtained by numerically inverting each section were matched, with the average value being used at the common point. A diametrical (though not necessarily symmetric) profile of the continuum emission coefficient resulted, from which the diametrical temperature profile was determined using Figure 41 in Appendix B.

The diameter of the luminous zone at the first downstream position was found to be 0.978 cm. This compares with a

diameter of 0.988 cm measured during the equilibrium runs by observing the 4300 Å argon line rather than the continuum at 5330 Å. The luminous diameter is defined as the region over which the continuum intensity can be distinguished from the photomultiplier dark current, i.e. the region over which the photomultiplier signal is greater than the photomultiplier dark current. The luminous diameters observed are slightly less than the nozzle diameter of 1.031 cm, as would be expected. The diameter of the luminous zone remained constant or decreased when moving to positions further downstream. These variations (if any) were measured at each level, and taken into account when inverting the two sections of the chord intensity profile.

Velocity Computation

Knowledge of the difference in impact and free stream pressure ($P_o - P_\infty$) and the free stream temperature T_∞ at any point in the plasma jet permitted calculation of the velocity at that point using equation (4-33). The calculation was performed numerically. At any vertical position the pressure at the confining chamber wall was used as the free stream pressure for every point along the diametrical pressure profile. Since the viscous term in equation (4-33) must be evaluated at the reference temperature, the probe wall temperature was estimated to be constant at 980 °F (800 °K). The insensitivity of the

reference temperature to the wall temperature was noted previously. This particular wall temperature was chosen since it is slightly less than the melting temperature of the solder used in sealing the probe tip. From the constant wall temperature and the given free stream temperature, the computer program internally calculated the reference temperature and evaluated the viscosity and density at this temperature. A polynomial temperature fit of Sherman's viscosity values (48) was included in the program. The density at both the free stream and reference temperatures was obtained using equation (A-29) and the Saha equation. Atmospheric pressure was assumed in computing the density. The heat capacity ratio at the free stream temperature was the only external variable required in addition to the pressure difference and free stream temperature. This was obtained from the tabulated values of Drellishak (20).

The output from the velocity calculation included the actual velocity, the ideal or Bernoulli velocity, the Reynolds number for flow around the probe, and the contribution of each of the three terms in equation (4-33) to the measured impact pressure. The computations were made at twenty equally spaced positions along the diametrical pressure profile.

Equation (4-33) was also used in computing the cold flow velocity from the difference impact and free stream (wall) pressure. The calculation was significantly simplified,

however, since the jet was isothermal at essentially 60 ^{o}F. Thus, physical properties in each term of the equation were constant. These calculations were also performed numerically, with the same output information being obtained.

Experimental Conditions The specific experimental conditions under which the two plasma operating modes were investigated are listed in Table II. As mentioned previously, a run exceeding two hours in duration was required. As a result during the time interval of the run, there was a slight drift in input power and energy transfer efficiency, so that a range of values is indicated for these parameters. The time average values are also indicated. It can be seen that fluctuations are not severe, but relatively, are of larger magnitude at the lower flow rate. This is in line with the general observation of a less stable operation at lower flow rates.

For the cold flow measurements, argon flow rates identical to those listed in Table II were used for the transitional and turbulent cases, while a flow rate of 18.8 gm/min was used for the laminar case.

Results Cold flow velocity profiles, dimensionless plasma velocity plots, temperature profiles, a "map" of the jet, and temperature and velocity decays are presented for the detailed studies of the transitional and turbulent operating modes.

Table II

Experimental Plasma Conditions for the Detailed Velocity Study

		Operating Mode	
		Transitional	Turbulent
Argon Flow Rate	gm/min	25.0	36.1
Input Energy	kw	7.00-7.26	7.33-7.58
Average	kw	7.15	7.46
Energy Transfer Efficiency	%	28.6-32.6	35.8-37.2
Average	%	30.1	36.6

Cold flow velocity profiles for the laminar mode are also presented.

Cold Flow

Since cold flow velocities are used as reference velocities in a later analysis, the cold flow profiles of axial velocity are considered first. These profiles are shown in dimensionless form in Figures 18, 19, and 20 for flow rates corresponding to the laminar, transitional, and turbulent plasma modes respectively. In each case, the reference velocity is the centerline velocity at the initial position (1 nozzle radii) downstream of the exit plane. The unit radius is the radius of the nozzle. The reference velocities are listed in Table III. Also listed in Table III is the corresponding ideal or Bernoulli velocity calculated for the same difference in impact pressure and wall pressure. The slight variation between the actual velocity and the Bernoulli velocity can be attributed to the viscosity effect, since the contribution of the compressibility term to the impact pressure amounts to only 0.01%. For comparison, the actual velocity profiles at the initial downstream position for the three flow rates are shown in Figure 21 as a function of dimensionless radius. It must be emphasized that in Figures 18 through 21 the labels "laminar", "transitional", and "turbulent" are used only to identify the corresponding flow rates, and in no way are

U_{ref} = 325 cm/sec
R = 0.516 cm

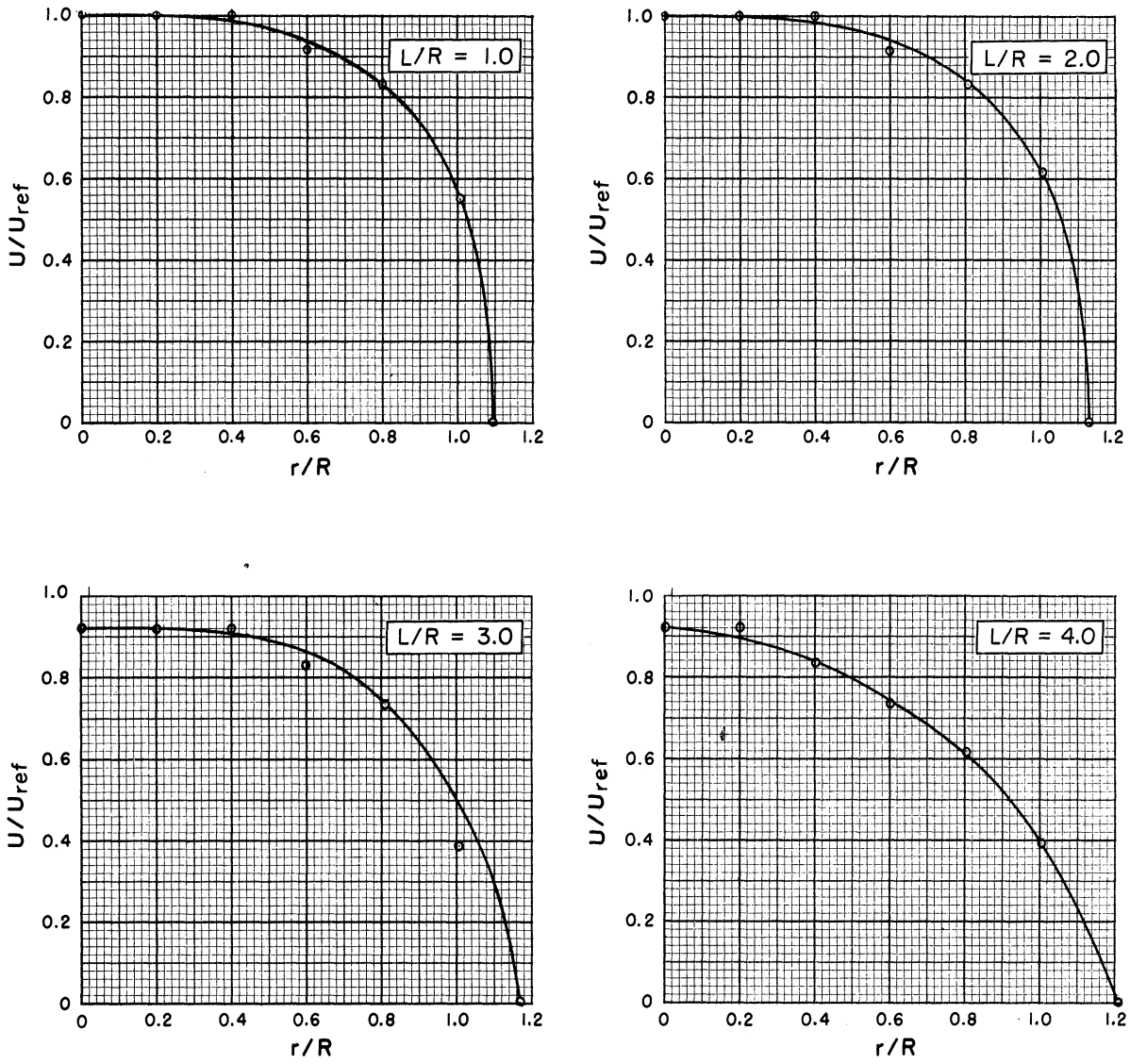

FIG. 18. DIMENSIONLESS PROFILES OF THE AXIAL VELOCITY FOR THE LAMINAR MODE IN COLD FLOW

U_{ref} = 360 cm/sec
R = 0.516 cm

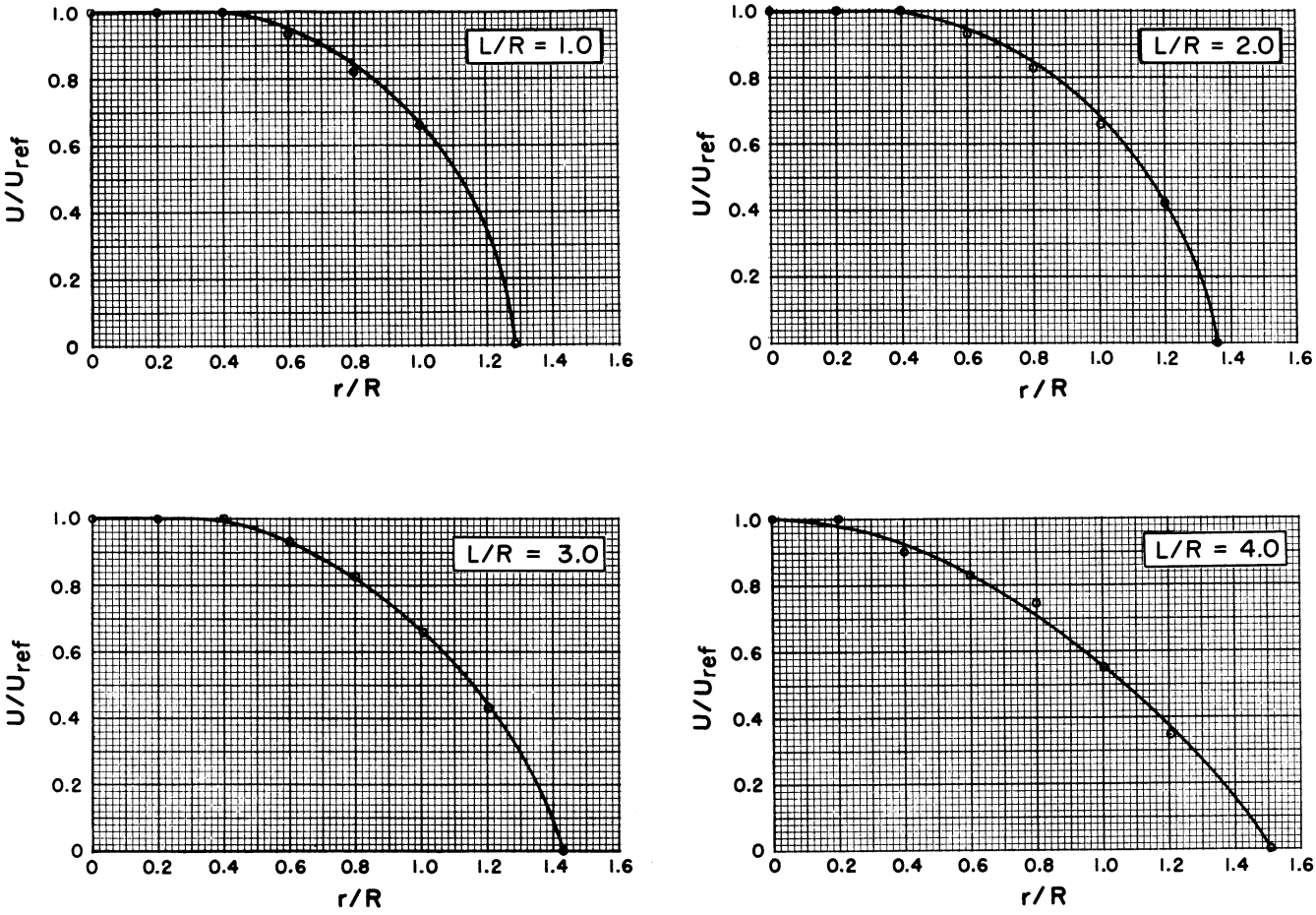

FIG. 19. DIMENSIONLESS PROFILES OF THE AXIAL VELOCITY FOR THE TRANSITIONAL MODE IN COLD FLOW

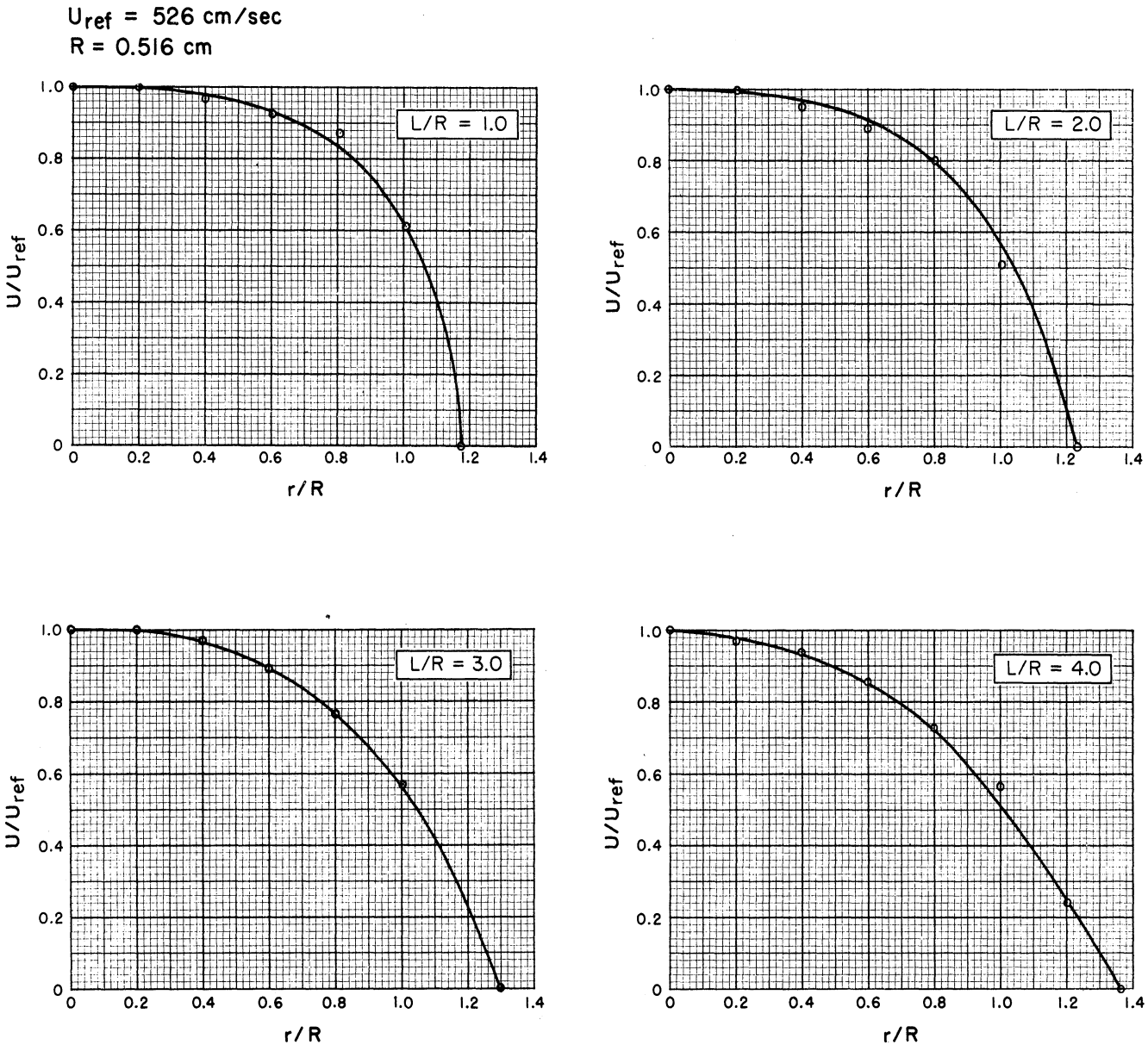

FIG. 20. DIMENSIONLESS PROFILES OF THE AXIAL VELOCITY FOR THE TURBULENT MODE IN COLD FLOW

Table III

Cold Flow Reference Velocities

Flow Rate gm/min	Reference Velocity cm/sec	Bernoulli Velocity cm/sec
18.8	325	326
25.0	360	362
36.1	526	527

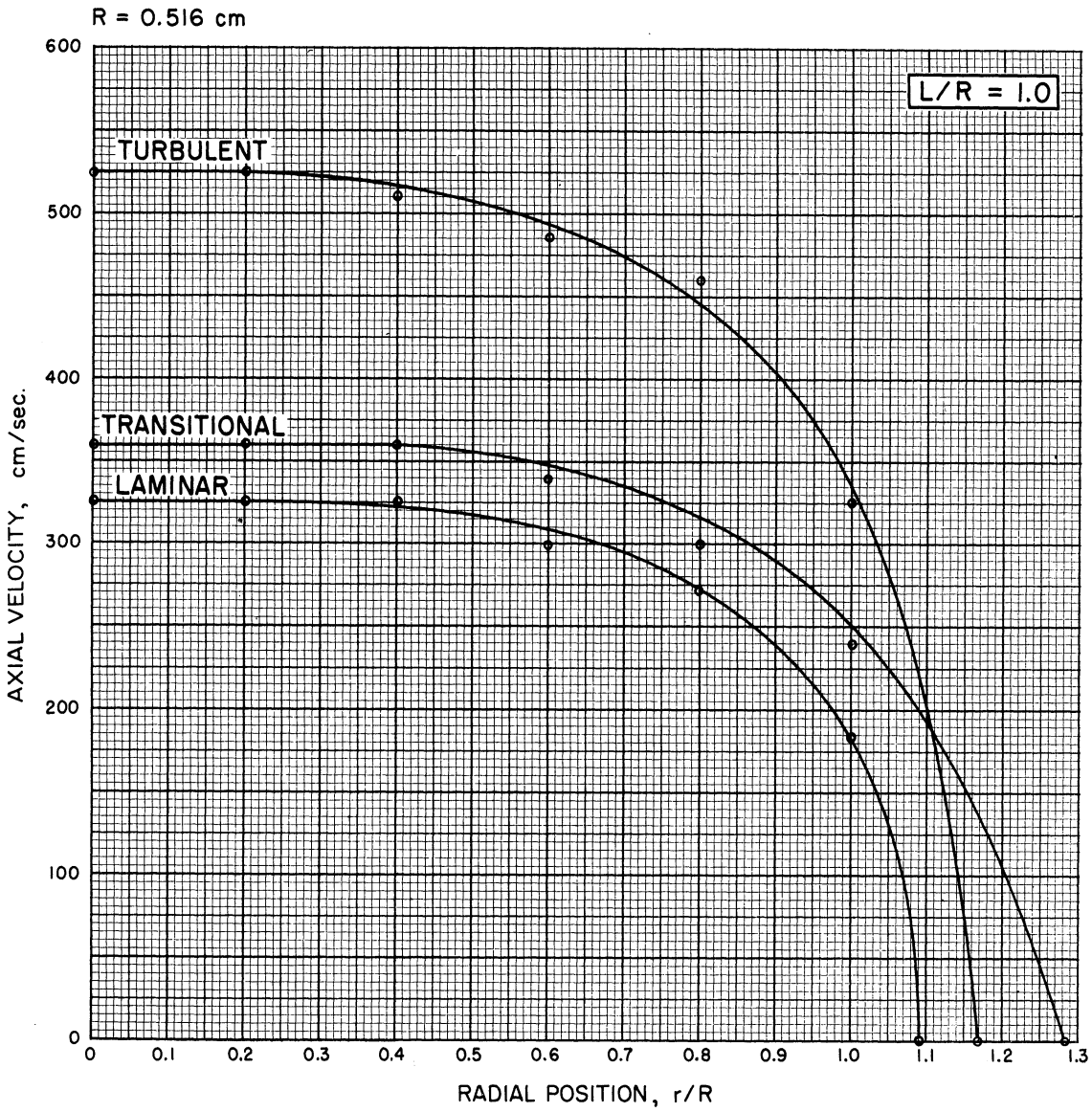

FIG. 21. COMPARISON OF THE AXIAL VELOCITY PROFILES AT THE INITIAL DOWNSTREAM POSITION IN COLD FLOW

intended to imply that three distinct types of jet exist in cold flow, although this possibility is discussed later.

In Figures 18 through 21 it is only necessary to show the right half of the profiles because the cold jets were found to be symmetrical about the central axis. Symmetry was ascertained by comparing chord pressure profiles obtained equidistant about the diametrical profile, and by folding the diametrical profile at the point coinciding with the nozzle axis and comparing each half.

At positions in the fringes (beyond $r/R = 1.0$), velocities were difficult to determine due to lack of sensitivity in the probe-transducer system in detecting small pressure differences. These differences were on the order of 0.0002 psi, and corresponded to a recorder chart deflection of less than 0.1%. The velocity was considered to be 0 at the position where the impact pressure could not be distinguished from the wall pressures. No negative pressures were observed either at the wall or along the pressure traverse.

From the sequence of dimensionless profiles for each flow rate, it can be seen that the velocity decays only gradually with increasing downstream distance, but that the momentum exchange region spreads noticeably in the radial direction with each increase in downstream position. The momentum exchange region is the region over which the impact pressure can be

distinguished from the free stream (wall) pressure. The fact that the velocity profiles for the intermediate flow rate extend to a greater radial position than do the profiles for the high flow rate is not readily resolved. A possible explanation is that in cold flow as in plasma flow, this flow rate corresponded to a transitional flow regime. The Reynolds numbers for the bulk flow through the nozzle would indicate that this is a possibility. For the intermediate flow rate, the Reynolds number was 2370. At the low flow rate, it was 1780; at the high flow rate, 3420. Thus, at the intermediate flow rate the flow in the nozzle could have been in a transition region between laminar and turbulent flow, which could in turn affect the flow patterns in the jet.

Plasma Flow

Dimensionless velocity profiles for the transitional plasma jet are shown in Figure 22 as a function of dimensionless lateral position. The corresponding temperature profiles are shown in Figure 23. The reference velocity used in computing the dimensionless velocity is the cold flow reference velocity, 360 cm/sec. Again, the unit distance is the nozzle radius. The limiting data points on the velocity profiles are determined by the limiting points on the temperature profiles, which in turn are established by the luminous diameters of the jet. Beyond these positions impact pressures could be measured but temperatures could not.

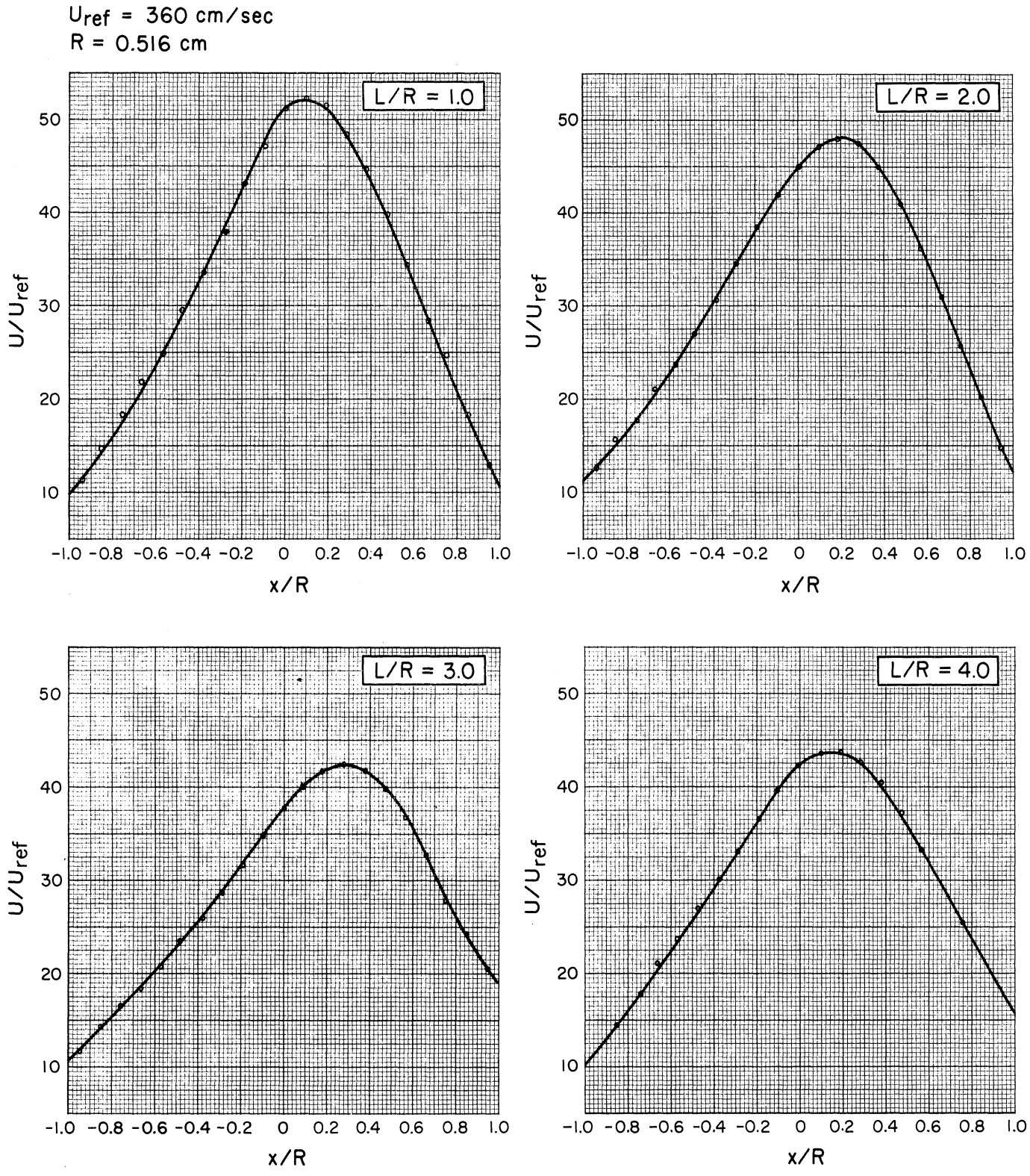

FIG. 22. DIMENSIONLESS PROFILES OF THE AXIAL VELOCITY IN THE TRANSITIONAL PLASMA JET

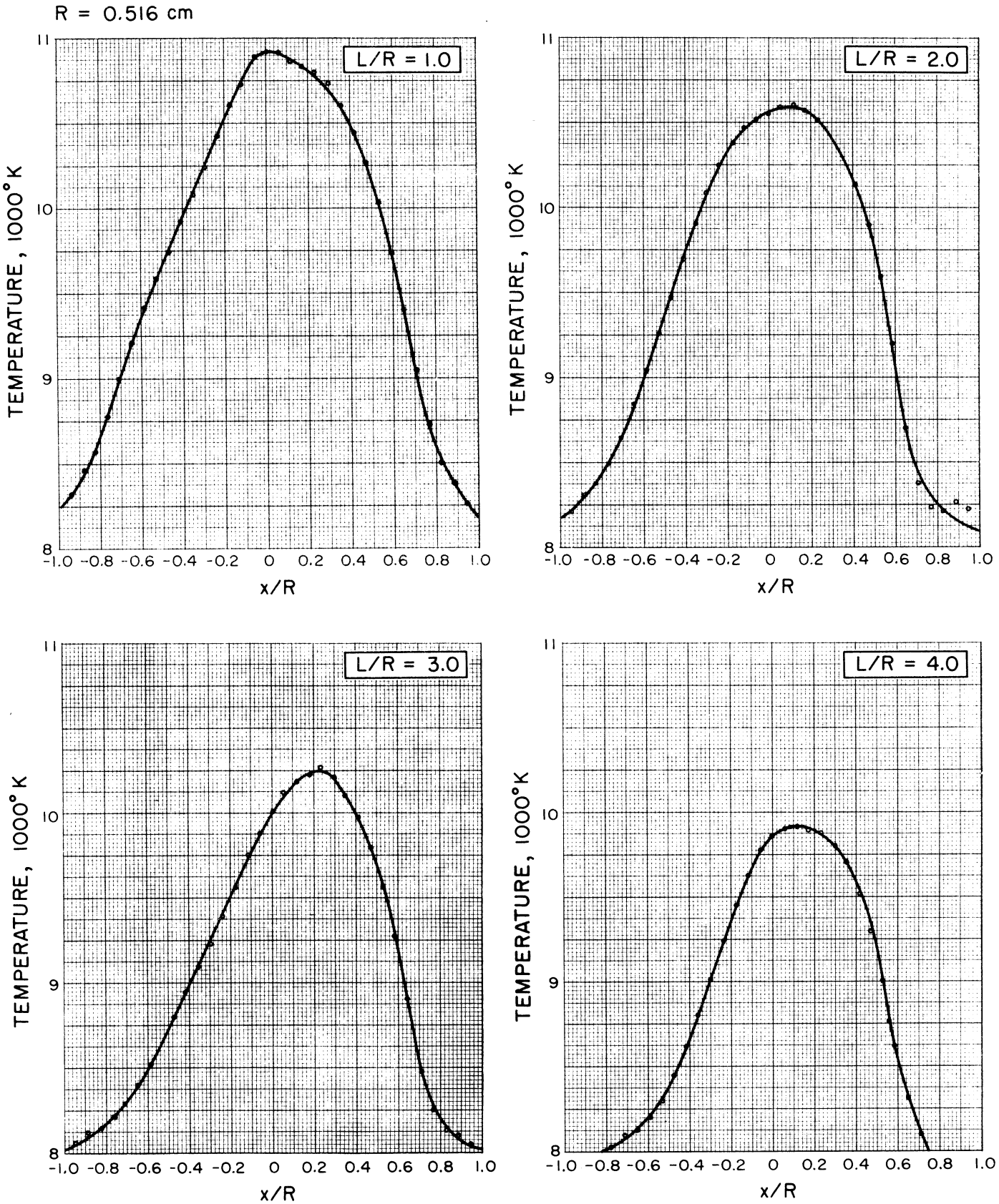

FIG. 23. TEMPERATURE PROFILES IN THE TRANSITIONAL PLASMA JET

It can be seen that both velocity and temperature profiles are asymmetric. This asymmetry is further illustrated by comparing the impact pressure profiles obtained at the initial downstream position. Traces of the actual diametrical and chord profiles are shown in Figure 24. The sequence of profiles from top to bottom represents a back to front progression through the plasma, the middle profile being the diametrical traverse. Because the jet is asymmetric, a "map" of the jet was prepared. This "map", which is shown in Figure 25, indicates the positions of maximum temperature, maximum impact pressure, and maximum velocity, and the momentum exchange zone at each of the four downstream positions. The momentum exchange zone at a downstream position of 8 nozzle radii is also shown. As in cold flow, no negative pressures were detected in the jet.

For the turbulent operating mode, the corresponding results are presented in Figures 26 through 29. The dimensionless velocity profiles are shown in Figure 26. Temperature profiles are presented in Figure 27. Traces of the five impact pressure profiles obtained at the first downstream position are indicated in Figure 28, and the "map" of the turbulent jet is shown in Figure 29. In Figure 28, the top to bottom sequence again represents a back to front progression through the plasma. The maximum dimensionless velocities are of smaller magnitude in the turbulent mode than in the transitional mode because the cold

R = 0.516 cm.

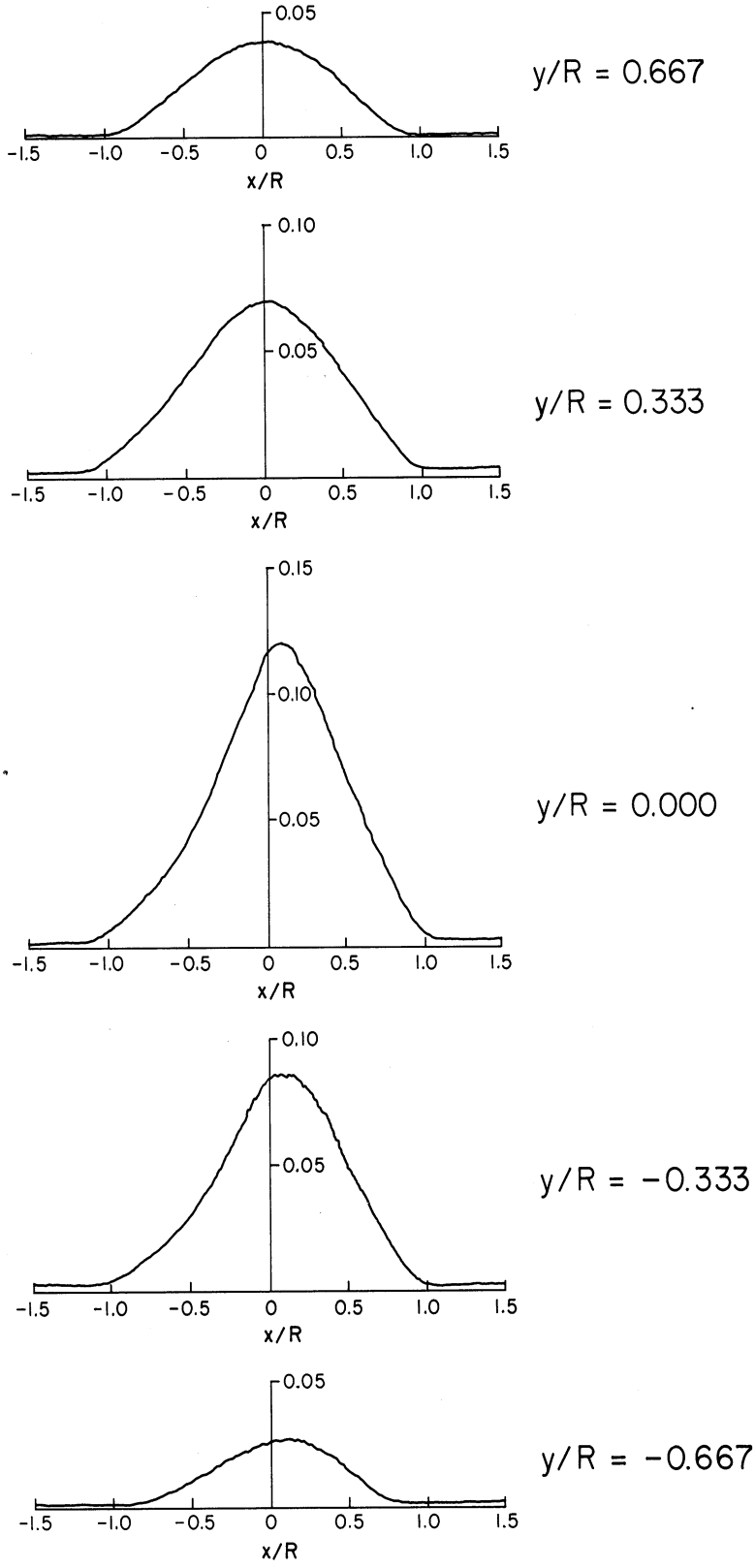

FIG. 24. COMPARISON OF THE IMPACT PRESSURE PROFILES AT THE INITIAL DOWNSTREAM POSITION IN THE TRANSITIONAL PLASMA JET

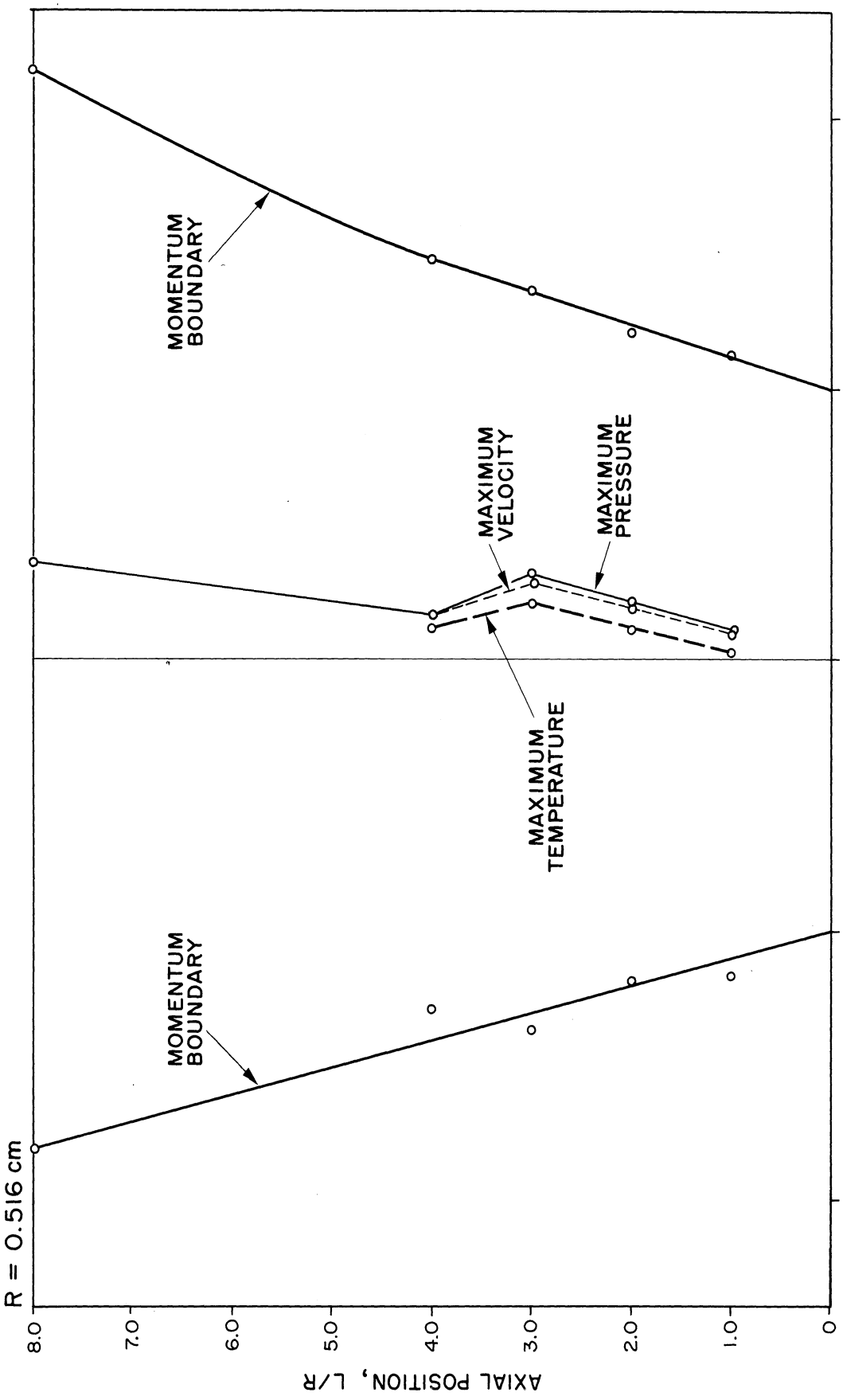

FIG. 25. MAP OF THE TRANSITIONAL PLASMA JET

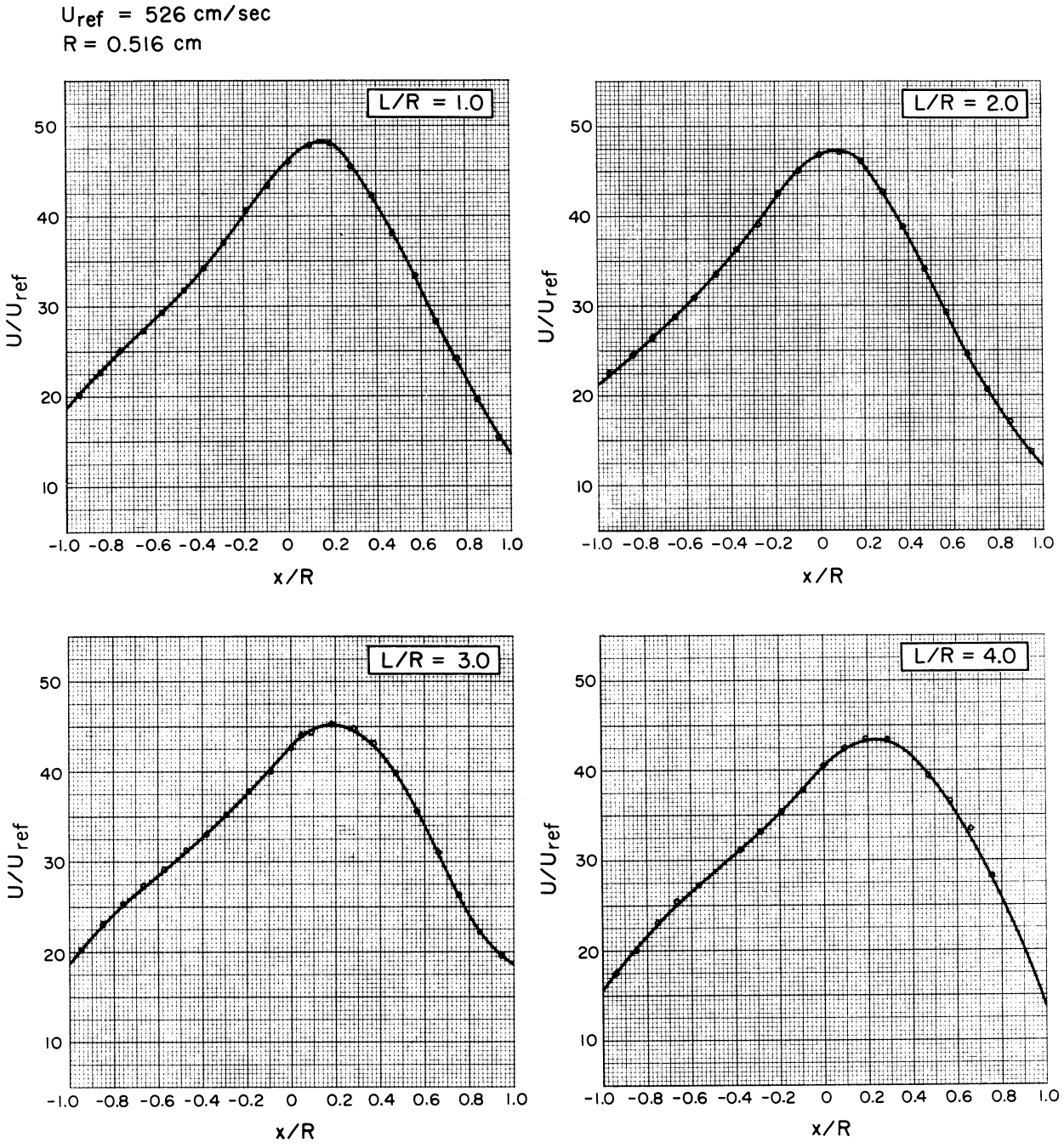

FIG. 26. DIMENSIONLESS PROFILES OF THE AXIAL VELOCITY IN THE TURBULENT PLASMA JET

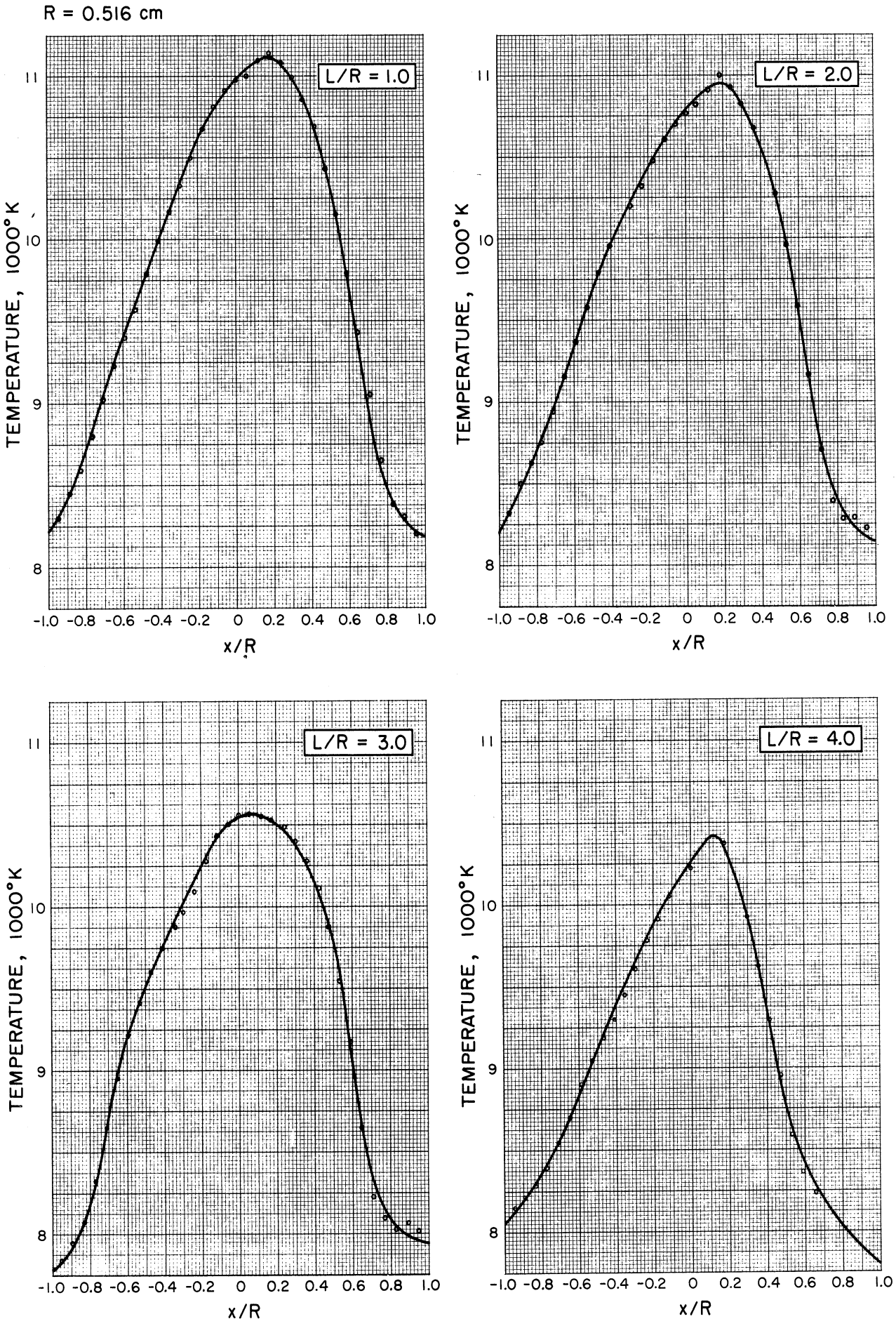

FIG. 27. TEMPERATURE PROFILES IN THE TURBULENT PLASMA JET

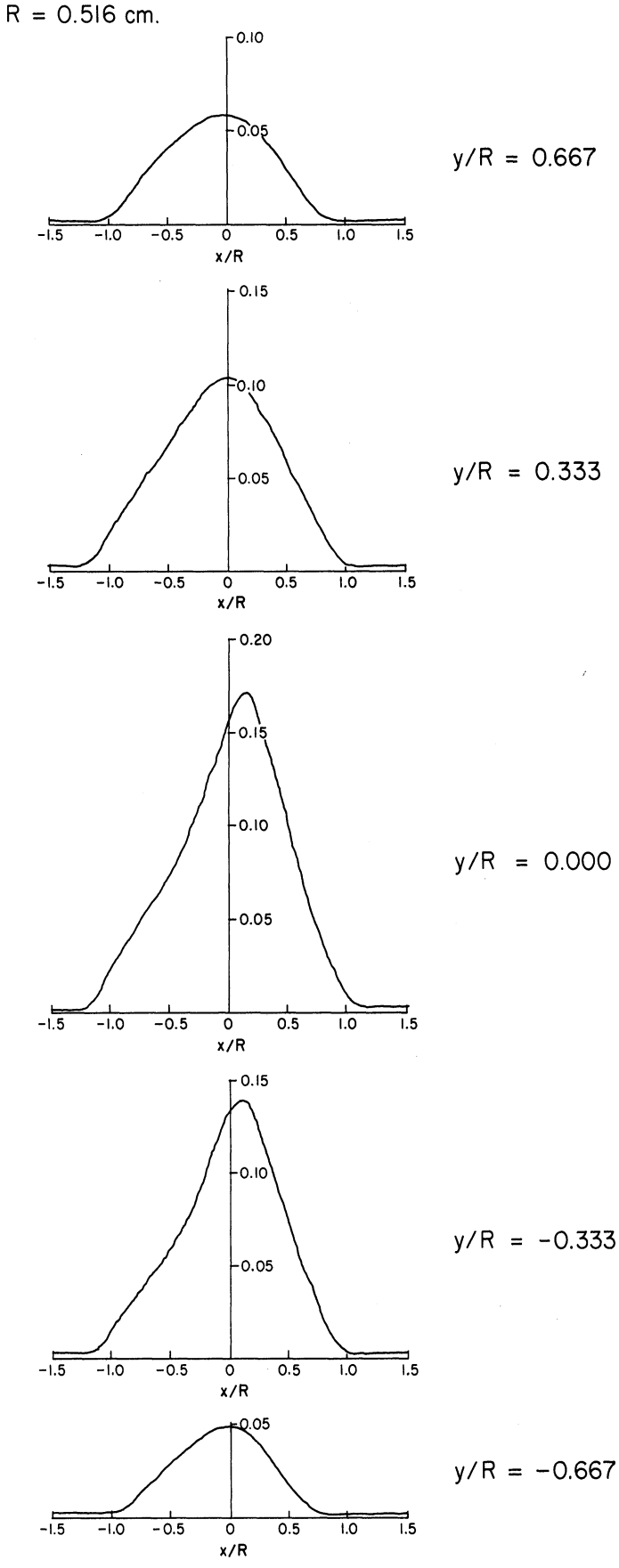

FIG. 28. COMPARISON OF THE IMPACT PRESSURE PROFILES AT THE INITIAL DOWNSTREAM POSITION IN THE TURBULENT PLASMA JET

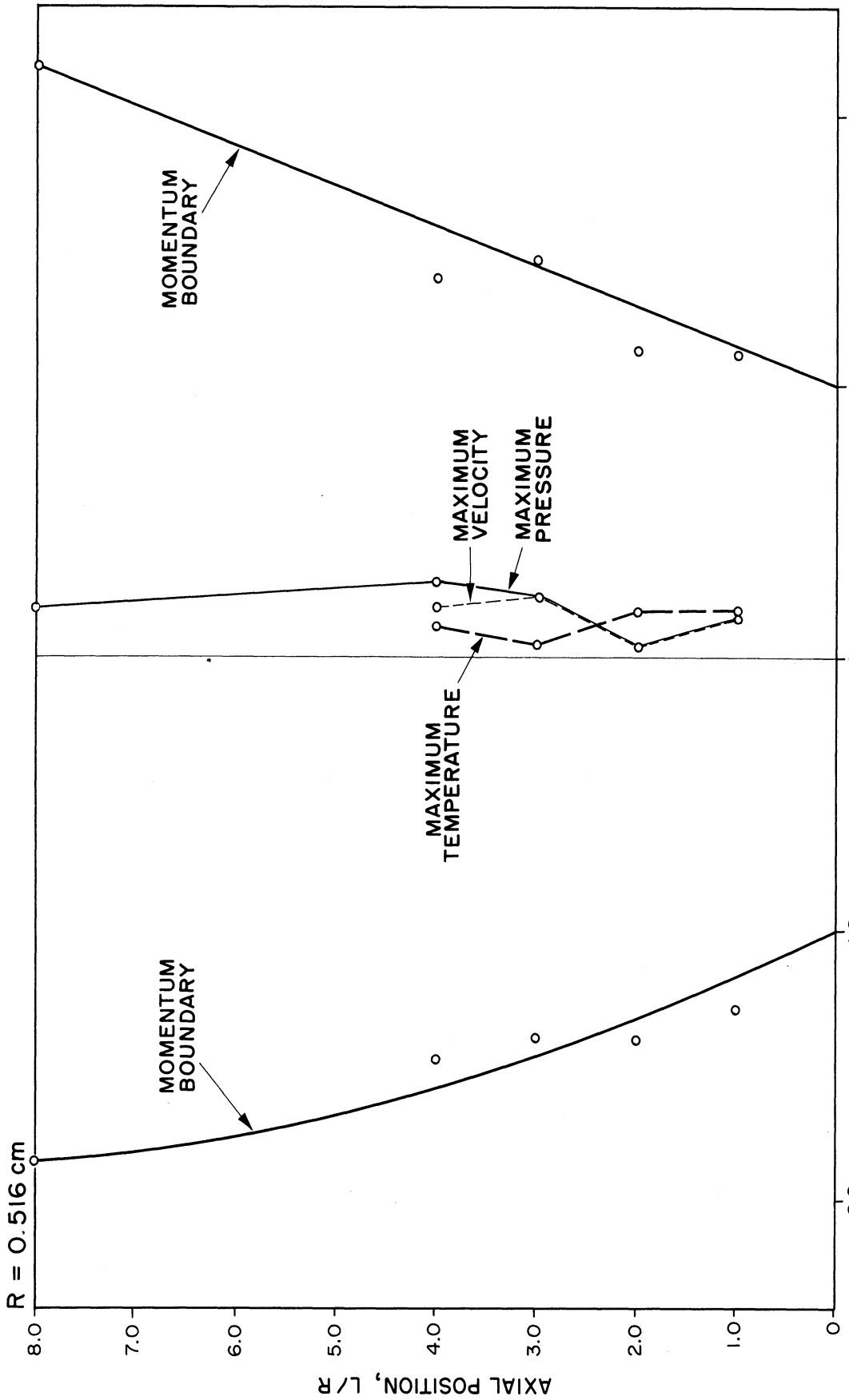

FIG. 29. MAP OF THE TURBULENT PLASMA JET

flow reference velocity is 526 cm/sec rather than 360 cm/sec. Actual velocities for the turbulent jet are greater than those in the transitional jet, as expected. It can be seen from Figures 27 and 28 that temperatures and impact pressures are also greater in the turbulent mode. Again, no negative pressures were detected in the plasma jet.

Several comparisons between the transitional and turbulent jets can be made. Actual velocity profiles at the first downstream level are shown in Figure 30. As noted above, the velocities in the turbulent jet exceed those in the transitional jet. The decay in maximum temperature with increasing downstream position is indicated for each mode in Figure 31. The decay in maximum velocity for each jet is presented in Figure 32. It can be seen in these figures that both temperature and velocity decay more rapidly in the transitional jet than in the turbulent jet.

The velocities obtained for the turbulent operating mode are somewhat greater than those indicated by Grey (26) and Smith (52). Grey reports a centerline velocity of 12000 cm/sec and a temperature of 12000 ^{o}K at a position 1.3 nozzle radii downstream of the nozzle exit plane for a larger input power level than used in this study. Smith reports a centerline velocity of 14500 cm/sec and a temperature of 9400 ^{o}K at a downstream distance of 0.8 nozzle radii for essentially the

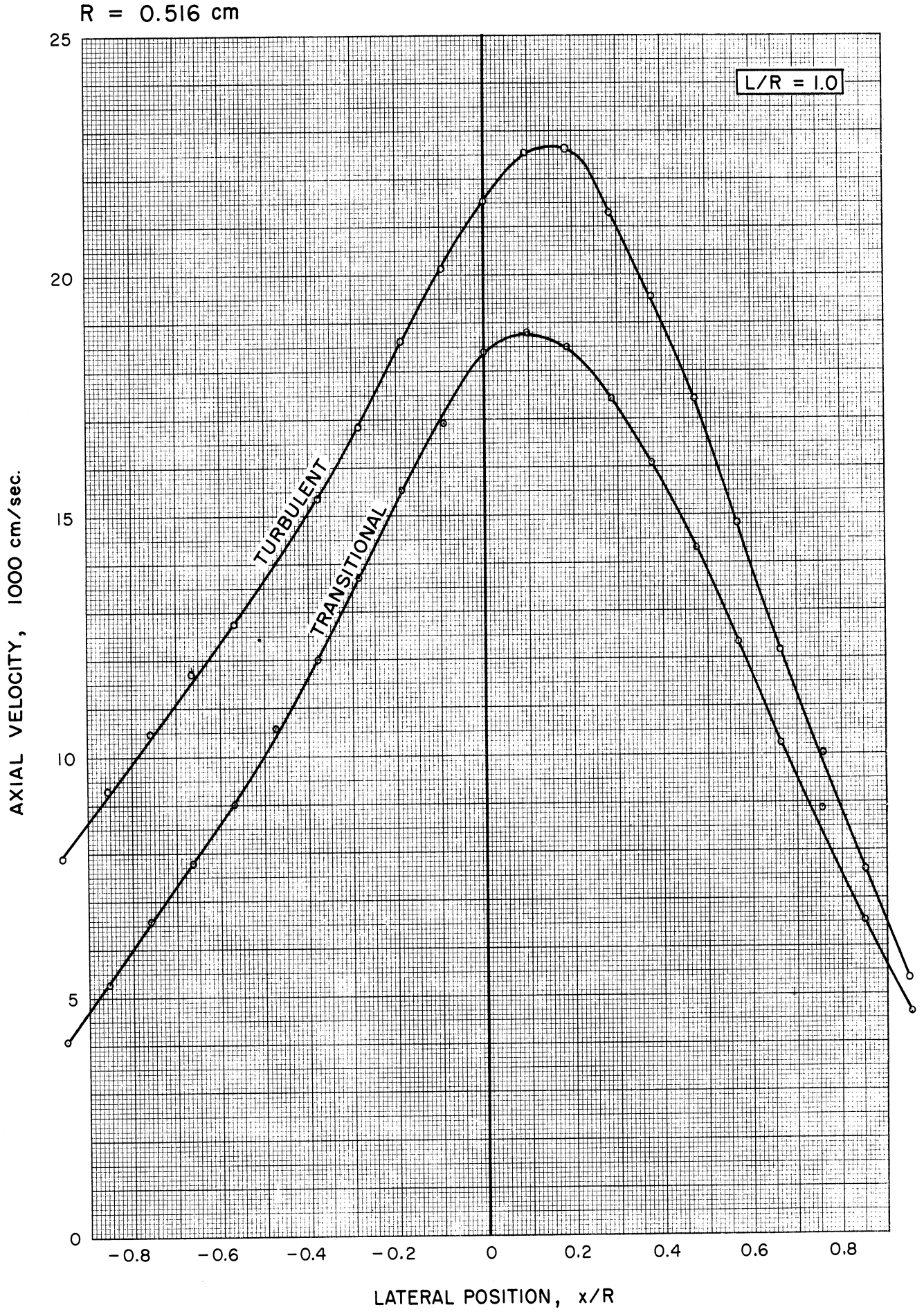

FIG. 30. COMPARISON OF THE AXIAL VELOCITY PROFILES AT THE INITIAL DOWNSTREAM POSITION IN THE TRANSITIONAL AND TURBULENT PLASMA JETS

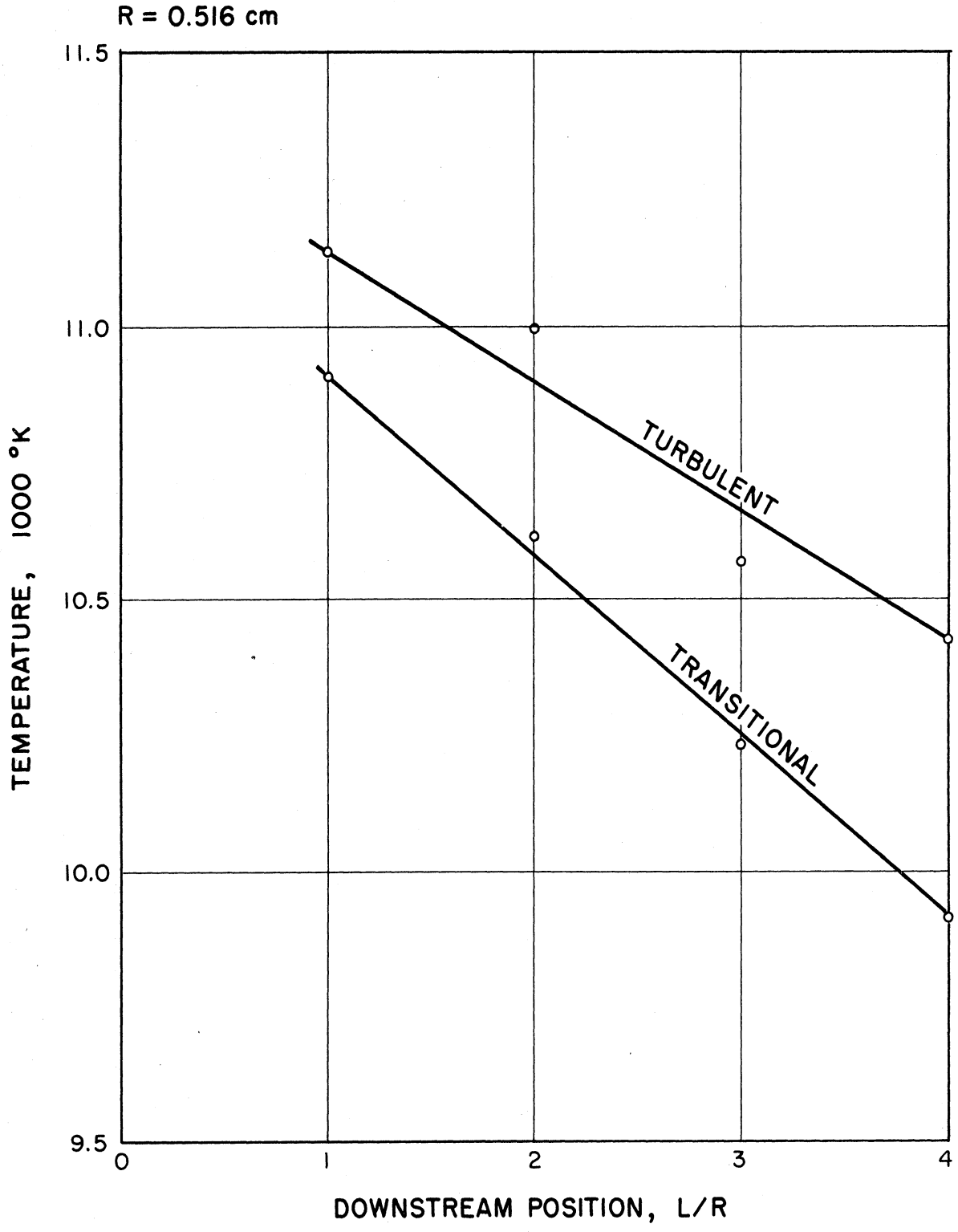

FIG. 31. MAXIMUM TEMPERATURE VERSUS DOWNSTREAM POSITION FOR THE TRANSITIONAL AND TURBULENT PLASMA JETS

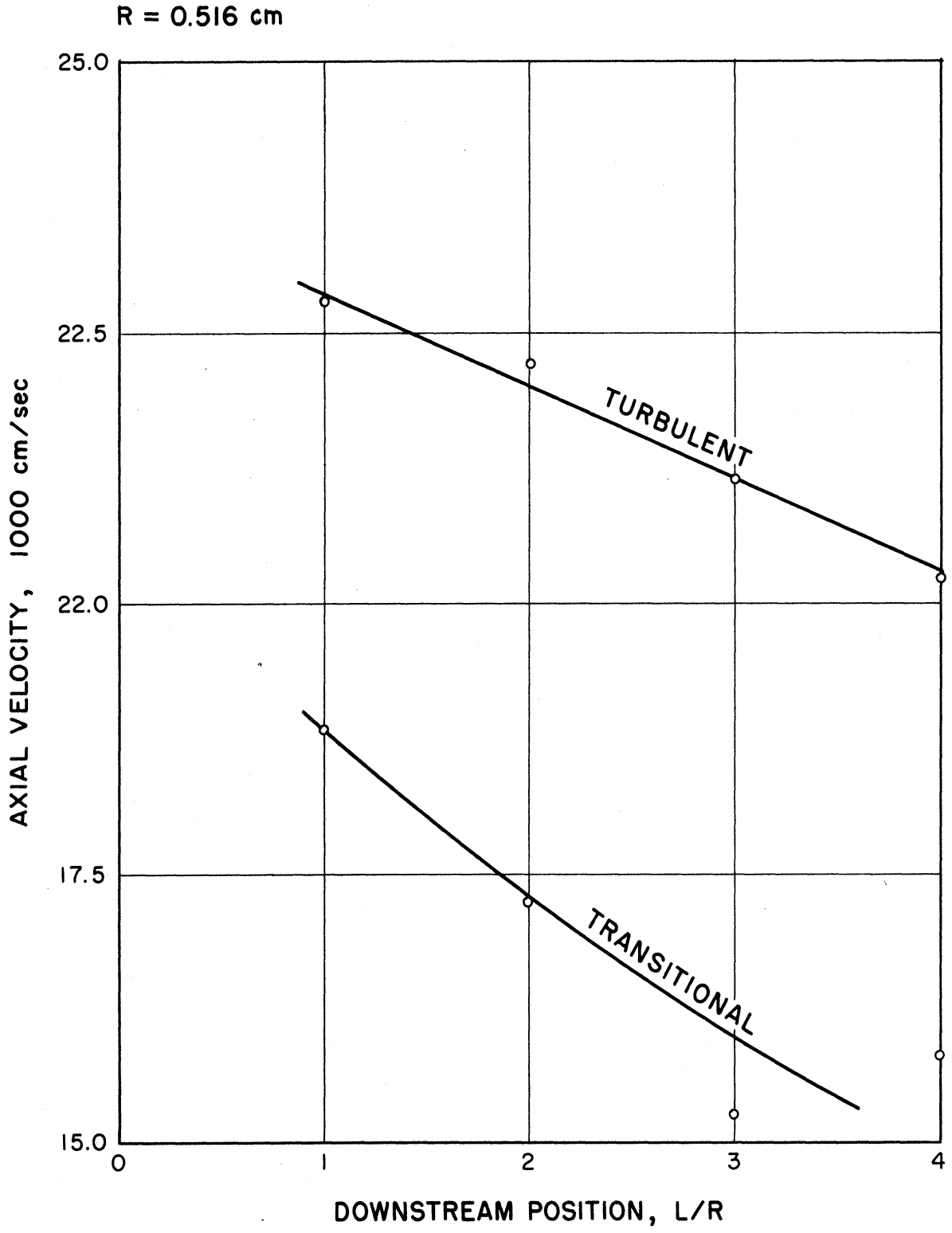

FIG. 32. MAXIMUM AXIAL VELOCITY VERSUS DOWNSTREAM POSITION FOR THE TRANSITIONAL AND TURBULENT PLASMA JETS

same input power as in this investigation. Smith's velocity values were expected to be approximately half of the corresponding values of this study because of the over-compensation for the effect of heat transfer. The velocities obtained for the transitional operating mode cannot be compared to other reported values for this mode because such information has not appeared in the literature, as noted previously. It is worthwhile however, to note values reported for the laminar operating mode. Gottschlich (25) calculated a centerline velocity of 76000 cm/sec at a downstream location of 1.8 nozzle radii by graphical differentiation of the temperature profiles. The corresponding temperature was 14000 ^{o}K. Cabannes (12) indicates an exit plane velocity of 70000 cm/sec and a temperature of 13000 ^{o}K for approximately the same input power as used to obtain the transitional and turbulent jets in this study. Sherman (49) reports a centerline velocity of 37000 cm/sec and corresponding temperature of 13000 ^{o}K at a downstream distance of 1.3 nozzle radii. Each of these values of velocity and temperature for the laminar mode are significantly higher than values obtained for either the turbulent or transitional modes in this study.

All of the investigators cited above with the exception of Sherman report values obtained in symmetrical plasma jets. The plasma jets in this investigation were found definitely to be

asymmetric, as shown previously. Since the cold flow profiles were perfectly symmetrical, the asymmetry was probably due to preferential attachment of the arc at the anode, which would cause the arc to deviate from the centerline of the nozzle and in turn result in non-uniform heating of the argon stream. This supposition is supported by the fact that when a cold flow profile was obtained at the exit plane prior to startup of the plasma generator and again after shutdown, both cold flow profiles were symmetric while the plasma profiles obtained during the run were not.

The decays in temperature and velocity observed in the transitional and turbulent plasma jets can be analyzed further. If the velocity decay is primarily due to cooling of the jet and the associated density increase rather than momentum transport, the continuity equation along the central axis of the jet can be approximated by

$$\rho_i u_i = c_1 \quad , \qquad (7\text{-}1)$$

where ρ_i = density on the central axis at level i

u_i = axial velocity on the central axis at level i

c_1 = a constant .

Rigorously, the continuity equation along the centerline would reduce to

$$\frac{\partial}{\partial z}(\rho_i u_i) + 2\rho_i \frac{\partial v_i}{\partial r} = 0 \quad , \qquad (7\text{-}2)$$

where v_i is the radial component of velocity. Continuing with the approximation, however, the degree of ionization of the argon is 5% or less for the temperatures achieved in these plasma jets and the pressure is essentially constant. Thus, the density which is expressed by equation (A-29) can be approximated by

$$\rho_i = \frac{c_2}{T_i} \quad , \qquad (7\text{-}3)$$

where T_i = temperature on the central axis at level i

c_2 = a constant .

Combining equations (7-1) and (7-3)

$$u_i = \frac{c_1}{c_2} T_i \quad , \qquad (7\text{-}4)$$

so that for a given jet, the centerline velocity at any level should be proportional to the centerline temperature. For both the transitional and turbulent jets, the centerline velocities

at each vertical level are plotted as a function of the corresponding temperatures in Figure 33. It should be pointed out that the centerline temperatures and velocities are not the maximum values indicated in Figures 31 and 32 respectively. It can be seen from Figure 33 that a straight line can be drawn through the data. Therefore, the approximation in equation (7-1) is valid and the primary reason for the velocity decay is the density increase arising from the cooling of the jet rather than the spreading of the jet due to momentum transfer.

A check on the values obtained for the velocities in the transitional and turbulent plasma jets is obtained by integrating the initial downstream profiles to determine the mass flow rate. The calculated value can then be compared with the metered argon flow rate to the plasma generator. For the transitional and turbulent jets, the velocities at each point on the initial profile shown in Figure 30 were multiplied by the corresponding density and area, and summed. The area used for each velocity zone was that of a half annular shell of the appropriate mean radius. Since the velocities were indicated only for the luminous zone which is slightly smaller than the zone of momentum exchange, the temperature profiles were extrapolated linearly to calculate velocities at the fringes of the impact pressure profiles. Two additional values were obtained in this manner at each edge. The results are presented in Table IV. The agreement between

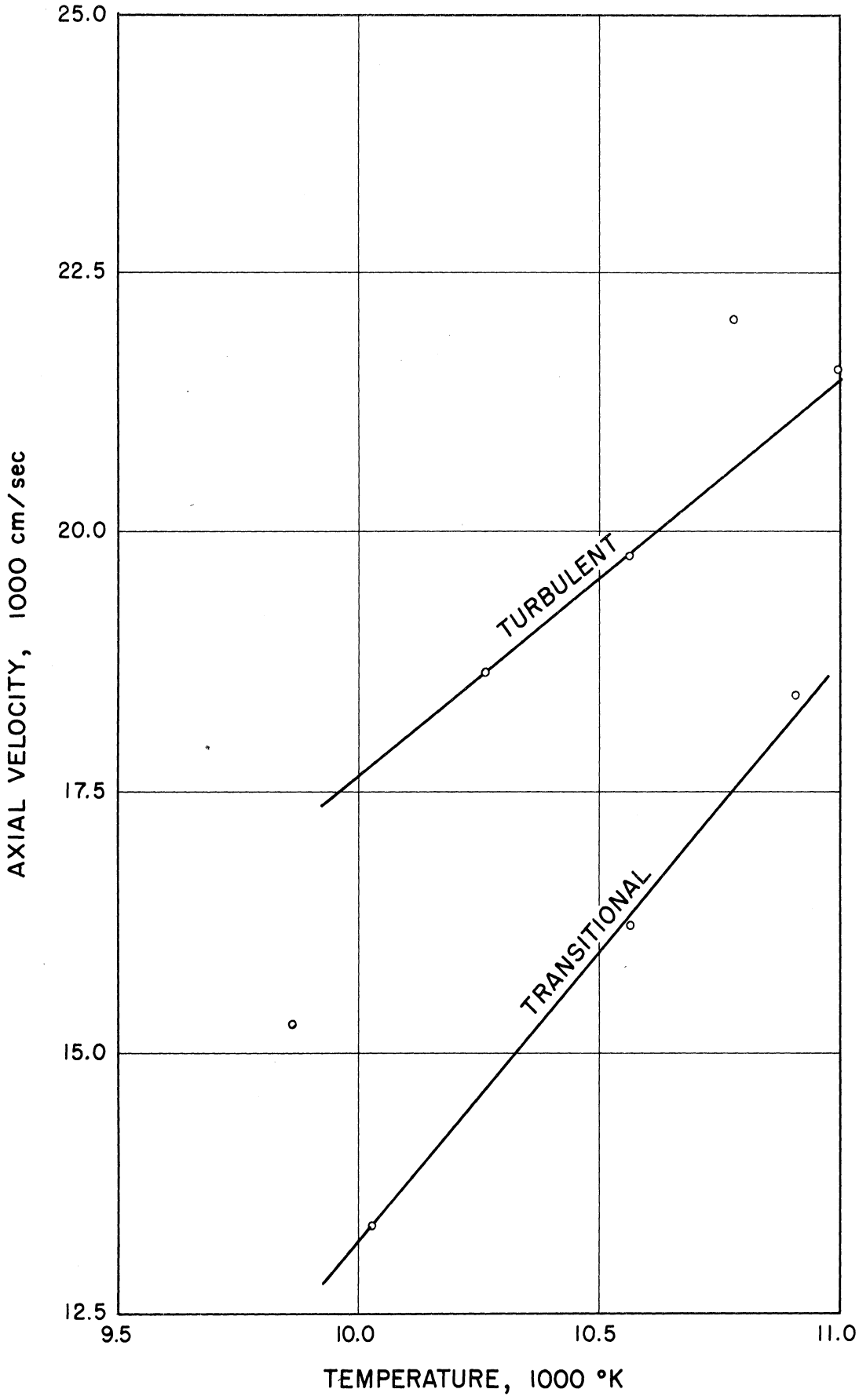

FIG. 33. CENTERLINE AXIAL VELOCITY VERSUS CENTERLINE TEMPERATURE FOR THE TRANSITIONAL AND TURBULENT PLASMA JETS

metered flow rate and calculated flow rate is considered excellent.

Table IV

Comparison of Metered and Calculated Flow Rates

Operating Mode	Metered Flow Rate gm/min	Calculated Flow Rate gm/min
Transitional	25.0	26.3
Turbulent	36.1	36.0

To complete this discussion of the detailed plasma velocity measurements, it is interesting to delineate and compare the non-ideal effects of compressibility and viscosity on the velocity measurements in each plasma jet. For five locations at the first downstream level, this information is indicated in Table V for both operating modes. The impact pressure, the temperature, the actual velocity, the ideal or Bernoulli velocity, and the contributions of the viscosity and compressibility terms of equation (4-33) to the measured impact pressure are listed. For the particular modes, the actual velocity at each location is that shown in Figure 30. From Table V it can be seen that

Table V

Effect of Viscosity and Compressibility
on Plasma Velocities

Position x/R	P psi	T ^{o}K	U cm/sec	U_B cm/sec	Vis %	Com %
			Transitional Mode L/R = 1.0			
-0.948	0.0082	8320	4080	4400	14.1	0.1
-0.474	0.0442	9730	10600	11120	8.4	0.8
0.000	0.1152	10910	18440	19320	6.8	2.1
0.474	0.0754	10260	14340	15000	7.3	1.4
0.948	0.0106	8260	4660	4990	12.5	0.1
			Turbulent Mode L/R = 1.0			
-0.948	0.0291	8300	7930	8290	7.9	0.5
-0.474	0.0766	9780	14100	14690	6.6	1.4
0.000	0.1554	11000	21560	22580	6.0	2.8
0.474	0.1082	10470	17430	18210	6.4	2.0
0.948	0.0140	8200	5380	5710	10.9	0.2

the viscous effect is of greatest magnitude at the edge of the jet, while the compressibility effect is of greatest magnitude near the center of the jet. In both modes, the viscous contribution to the impact pressure is more significant than the compressibility contribution. The effect of viscosity on impact pressure is greater in the transitional jet than in the turbulent jet, while the opposite is true for the compressibility effect. The sum of the two contributions is greatest near the edge of the jet, so that maximum deviation of the actual velocity from the ideal or Bernoulli velocity occurs at the edge of the jet. This same pattern of behavior is followed at each downstream position although at the farthest downstream positions, the deviation of actual velocity from ideal velocity becomes nearly uniform across the jet. Overall, the minimum observed viscous contribution to impact pressure was 5.3%, while the maximum observed compressibility contribution was 3.0%. Reynolds numbers for the flow around the probe based on the reference temperature were in the range of 40 to 100 for the transitional mode, and 40 to 150 for the turbulent mode.

Experimental Uncertainties

Uncertainties in the velocities obtained for the plasma jets arise from uncertainties both in the measured impact pressures and in the temperatures calculated from the measured continuum emission coefficients. The

possible errors in the calculation of plasma temperatures were discussed previously. It will be recalled that the maximum uncertainty in plasma temperature was estimated to be $\pm$ 1.7%. Uncertainties in the measured impact pressures occur because of possible errors in the calibration of the probe-transducer system, small variations in the impact pressure itself, and the error induced by the time lag of the probe. The maximum error in the calibration of the probe-transducer unit with the water manometer is $\pm$ 0.0003 psi. Fluctuations in the impact pressure occur because of the drift in the input power to the plasma generator and the random movements of the arc about its point of attachment. The maximum uncertainty associated with these variations is estimated to be $\pm$ 7%. Since the probe moves through the plasma jet, there is a dynamic error in the measured impact pressure because of the time lag in the response of the probe-transducer unit. The time constant of the probe was determined as explained in Appendix E, and found to be 0.25 sec. With the 5.6 rpm motor speed, the dynamic error is 0.6% of the maximum pressure on the profile. This error is negative along the ascending segment of the profile, and positive along the descending seqment. The cumulative effect of the uncertainties cited is most significant in the fringes of the jet and least significant near the jet centerline. Thus, in the transitional jet, the maximum uncertainty

in the calculated velocity ranges from ± 5.0% in the vicinity of the centerline to ± 8.4% in the fringes. For the turbulent jet, the maximum uncertainty is ± 4.9% near the central axis, and ± 7.1% in the fringes. In cold flow, the variations in the impact pressure and uncertainties in the temperature do not occur. Also, the dynamic error is insignificant. However, another possible error arises in trying to distinguish small changes in the pressure along the profile as noted previously. The maximum uncertainty arising from this is ± 0.0002 psi. Thus for the cold laminar jet, the maximum uncertainty in the calculated velocity is ± 20% near the centerline and ± 71% in the fringes. For the transitional jet, the range of maximum uncertainty is ± 16% to ± 39%; for the turbulent jet, ± 7.7% to ± 24%.

Effect of Power

To investigate the effect of input power level on the operation of the plasma generator and the flow patterns in the plasma jet, centerline velocities and temperatures were determined at three power levels for each of the three operating modes. The techniques involved in obtaining the data and resolving this information into the desired temperatures and velocities have been described previously.

Scope of Measurements The measurements for each operating mode were made using a flow rate identical to that employed in the detailed study of cold flow and plasma jet velocities. A diametrical impact pressure profile and a continuum emission profile were obtained at two vertical positions in the jet for each power level. Three power levels were investigated for each operating mode. The two vertical positions were 1 and 3 nozzle radii downstream of the nozzle exit plane. The procedures involved were the same as those used for the detailed velocity study, with the lone exception that in obtaining the "step" chord profile of the continuum intensity, the luminous portion of the jet was divided into 8 rather than 32 segments. This did not affect the accuracy of the centerline temperature, although it would have affected the accuracy of any temperatures desired in the fringes. A single run was used to obtain the necessary data for the transitional and turbulent modes, while a separate run was required for the laminar mode.

Experimental Conditions The specific experimental conditions under which the effect of power was investigated are listed in Table VI. For each mode of operation the argon flow rate is indicated along with the three power levels which were labeled "low", "intermediate", and "high". These power levels corresponded approximately to currents of 200 amps, 300 amps,

Table VI

Experimental Plasma Conditions for
Investigation of the Effect of Power

	Operating Mode		
	Laminar	Transitional	Turbulent
Argon Flow Rate · gm/min	18.8	25.0	36.1
Input Energy kw			
Low Power	4.56	4.61	4.66
Intermediate Power	6.85	7.43	7.45
High Power	9.12	10.10	10.17

and 400 amps respectively, and are the average of several instantaneous values.

Results The effect of input power level on the overall operation of the plasma generator is indicated, and the variations of centerline velocity and temperature with power are presented for each operating mode.

Plasma Generator Operation The effect of power on the characteristic operating conditions of the plasma generator is considered first, so that these results can be used in correlating the variations in temperature and velocity. Figure 34 shows the dependence of arc voltage on current for each mode of operation. Figure 35 shows the dependence of the efficiency of energy transfer to the gas on arc current for each mode. The values shown in both figures are averages of several instantaneous readings. It can be seen that for a given current, both arc voltage and energy transfer efficiency increase with argon flow rate as postulated previously. While the trends indicated for the variations in voltage and efficiency with increasing current and/or flow rate were consistent and reproducible from run to run, the exact values could not be duplicated from one run to the next. The maximum deviations observed for identical operating conditions were approximately $\pm$ 10%, although in most cases these deviations were $\pm$ 5% or less.

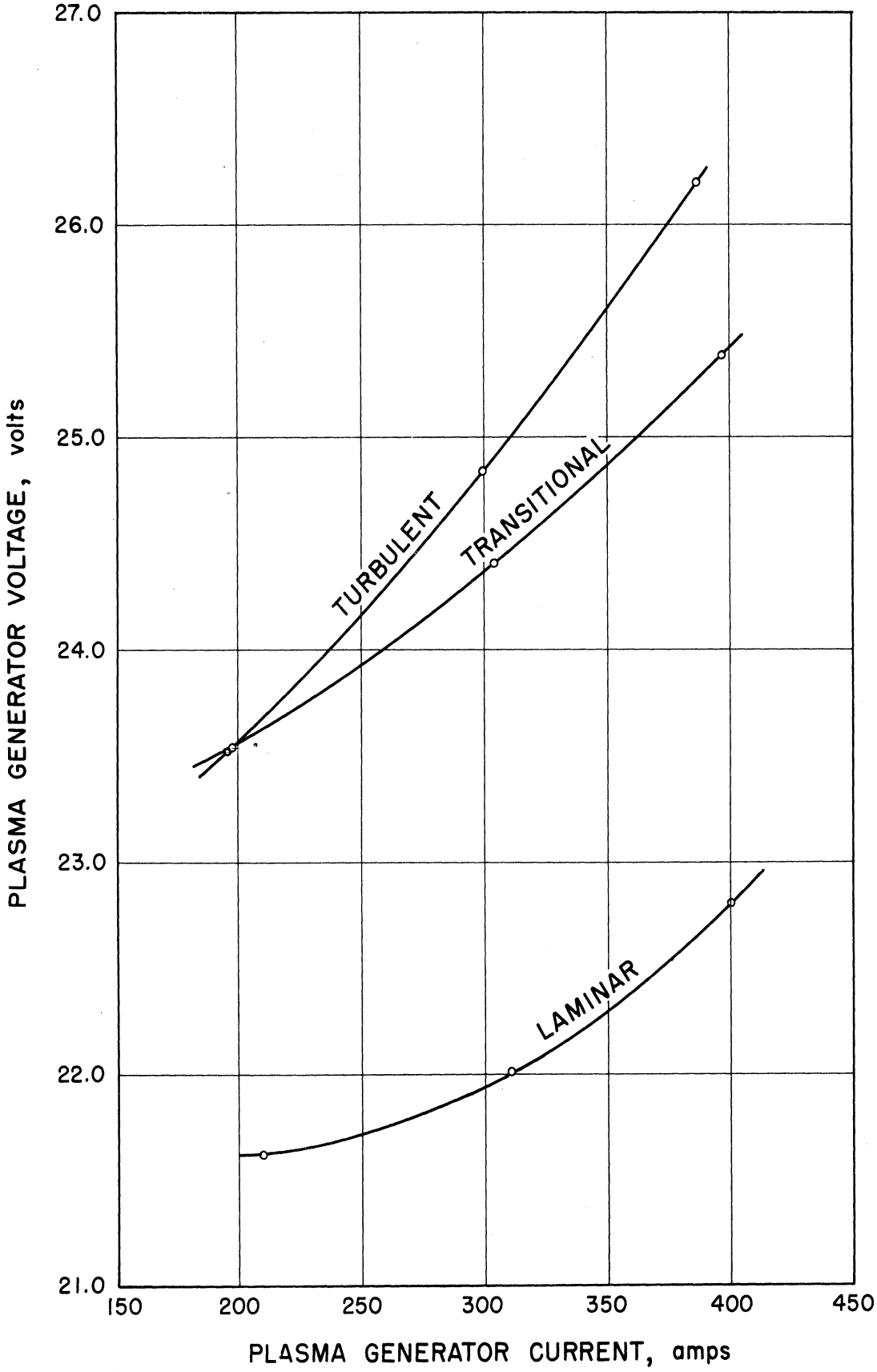

FIG. 34. OPERATING CHARACTERISTICS OF THE PLASMA GENERATOR FOR THE LAMINAR, TRANSITIONAL, AND TURBULENT MODES

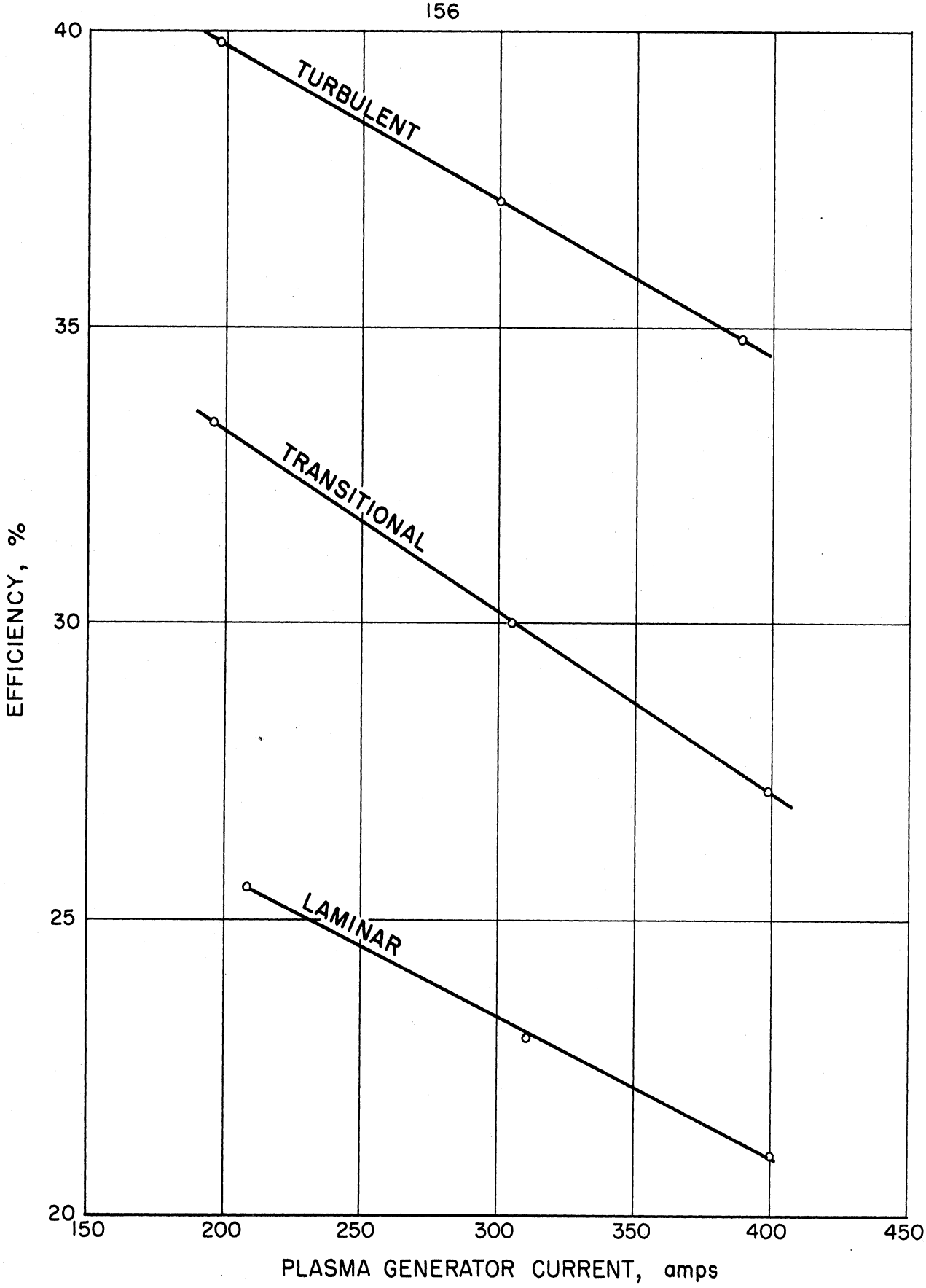

FIG. 35. EFFICIENCY OF ENERGY TRANSFER TO THE ARGON AS A FUNCTION OF THE PLASMA GENERATOR CURRENT FOR THE LAMINAR, TRANSITIONAL, AND TURBULENT MODES

Flow Patterns

The effect of input power level on the flow patterns in the plasma jet is demonstrated by analyzing impact pressure profiles, and centerline velocities and temperatures. In general, at any position in the jet an increase in input power for a given flow rate (operating mode) caused the impact pressure, the temperature, and the resulting velocity to increase also. Qualitatively, this behavior was anticipated although no quantitative predictions could be made. In addition, an increase in power caused the impact pressure profile to become more asymmetric. A typical example is shown in Figure 36, which presents the impact pressure profiles at a position 3 nozzle radii downstream of the exit plane in the turbulent operating mode for the three input power levels. It can be seen that with each increase in power, the pressure profile becomes more asymmetric and the point of maximum pressure becomes further removed from the nozzle centerline. This behavior while not anticipated, is consistent with the suggestion that asymmetry was caused by the arc deviating from the nozzle centerline, since an increase in power level would result in an even more severe non-uniformity in the heating of the argon stream. It should also be noted that no negative impact pressures were observed along any of the pressure profiles for the three operating modes, although

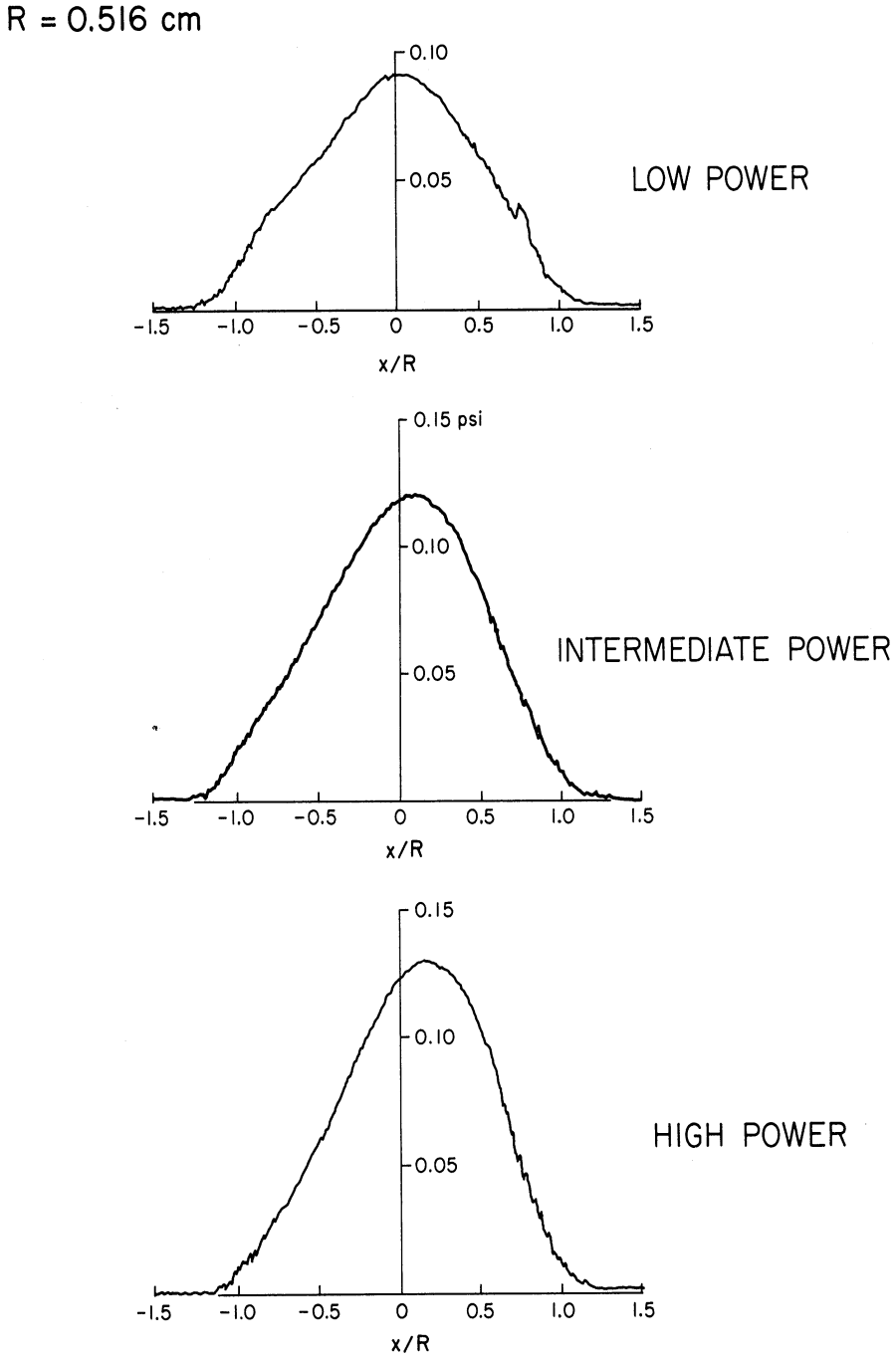

FIG. 36. EFFECT OF POWER LEVEL ON THE IMPACT PRESSURE PROFILES AT A DOWNSTREAM POSITION OF 3 NOZZLE RADII IN THE TURBULENT PLASMA JET

slightly negative wall pressures were detected at both downstream positions when operating with the high input power level in the turbulent mode.

The centerline temperatures and velocities were correlated in the same manner employed to analyze the decay of centerline velocities and temperatures in the detailed study at the intermediate power level. It will be recalled that for a given argon flow rate, the mass flux along the centerline of the jet was shown to be essentially constant. This same conclusion should remain valid for variations in the input power level at a fixed flow rate. Thus, for the specified flow rate, all centerline velocities should be proportional to the corresponding temperature as indicated by equation (7-4), regardless of either downstream position or input power level. In Figure 37 for each of the three operating modes, the centerline velocities at both vertical positions for each of the three input power levels are shown as a function of the corresponding centerline temperature. As expected, a straight line again can be drawn through the data for each mode. The line obtained in the turbulent case corresponds essentially to the one obtained in the detailed study at the intermediate power level. In the transitional case, the line shown in Figure 37 differs somewhat from the one previously obtained.

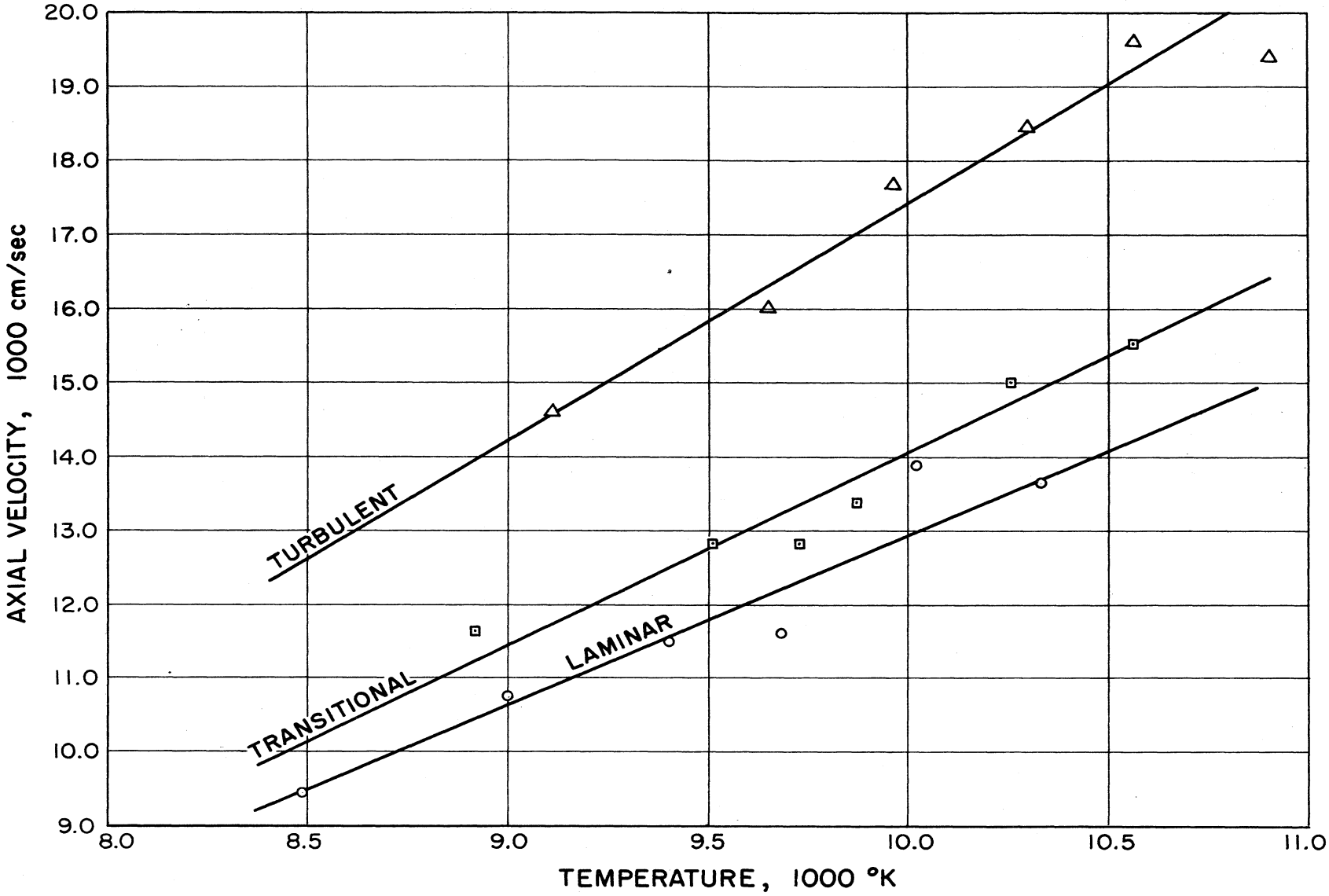

FIG. 37. CENTERLINE AXIAL VELOCITY VERSUS CENTERLINE TEMPERATURE FOR THE LAMINAR, TRANSITIONAL, AND TURBULENT PLASMA JETS

In order to relate the variations in the centerline velocity and temperature to the variations in input power level, the net input electrical energy transferred to a unit mass of gas was calculated for each value of centerline temperature. The net input electrical energy was calculated from values of voltage, current, and efficiency obtained both before and after each "step" chord profile of the continuum intensity. Thus, the net input energy per gram of argon represents the average bulk value over the time period of the spectrographic measurement. The centerline temperature of course was obtained from the continuum intensity profile. At a given downstream position in the jet, the centerline temperatures were plotted as a function of the logarithms of the corresponding net input energy per gram of argon for each of the three operating modes. The results at 1 nozzle radii downstream of the exit plane are shown in Figure 38. Figure 39 presents the results at 3 nozzle radii downstream. It can be seen that at both downstream positions, the values for a given mode lie on a straight line. The fact that the values obtained for each mode at a given vertical position are on separate lines rather than a single line indicates that a different mechanism for energy transfer to the gas may be associated with each operating mode. Corroboration of this was beyond the scope of the present study.

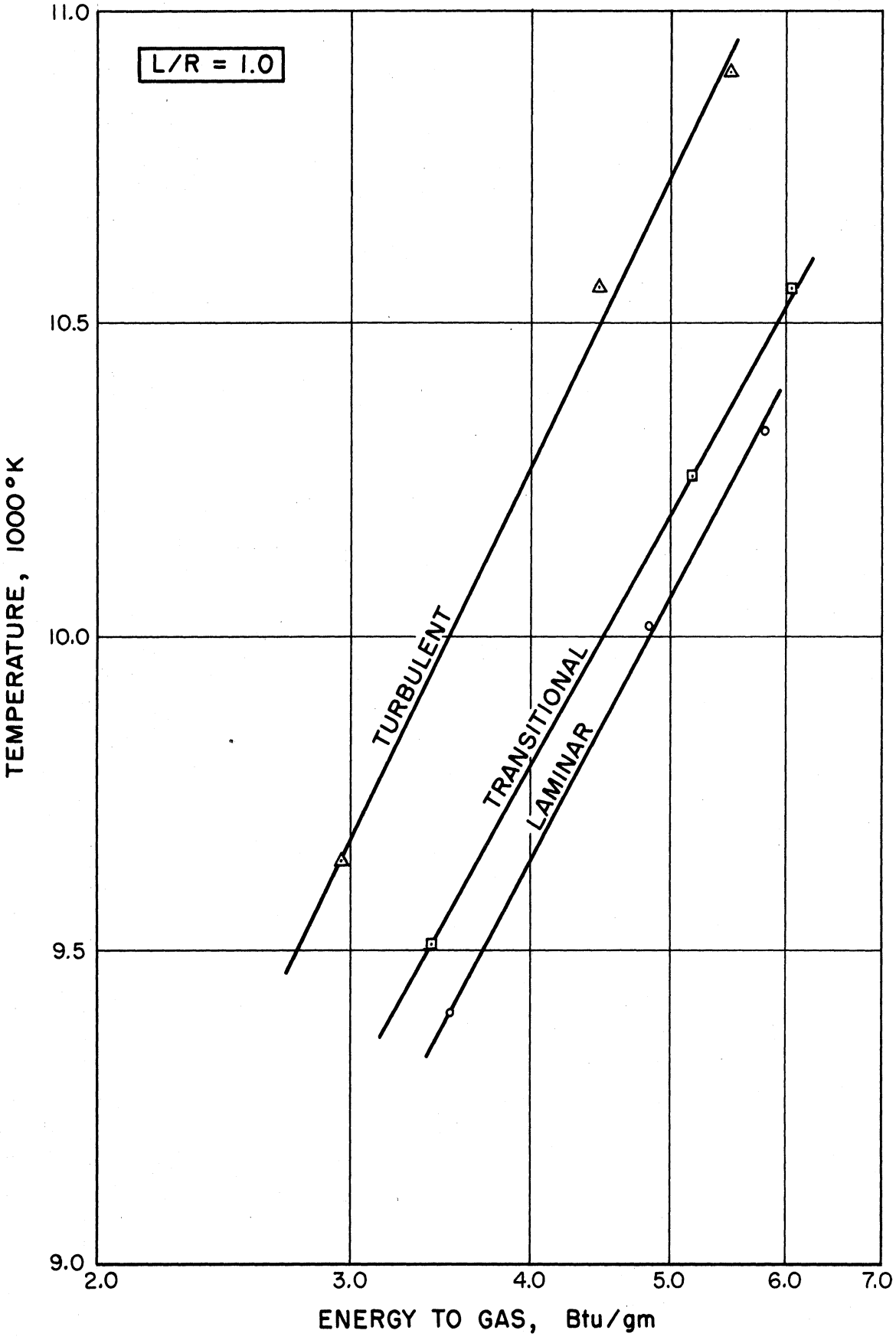

FIG. 38. CENTERLINE TEMPERATURE AT L/R = 1.0 VERSUS THE NET INPUT ENERGY PER GRAM OF ARGON FOR THE LAMINAR, TRANSITIONAL, AND TURBULENT PLASMA JETS

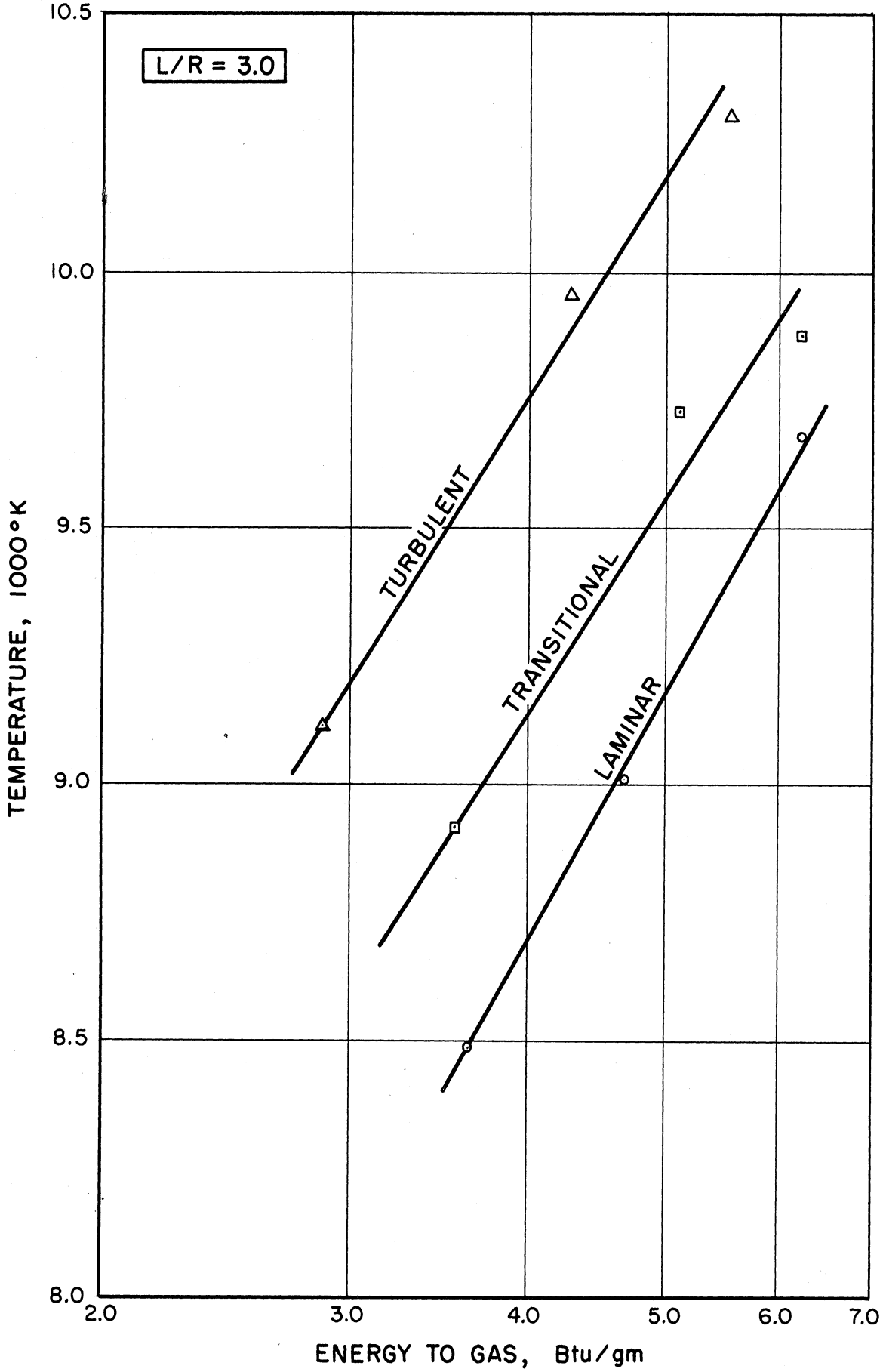

FIG. 39. CENTERLINE TEMPERATURE AT L/R = 3.0 VERSUS THE NET INPUT ENERGY PER GRAM OF ARGON FOR THE LAMINAR, TRANSITIONAL, AND TURBULENT PLASMA JETS

As a result of Figures 38 and 39, the voltage-current and efficiency-current relationships for a particular flow rate can be used to obtain the net input energy per gram of argon, which in turn can be used for the specified flow rate to obtain the centerline temperature at either of the downstream positions. This centerline temperature for the flow rate of interest can then be related to the centerline velocity using Figure 37. It must be cautioned that the correlations presented are only applicable to the plasma generator used in this investigation. The method of analysis, however, should be applicable to any plasma generator employing axial flow. Thus, the effect of input power on the operating parameters of the plasma generator has been demonstrated, and variations in these parameters have been related to variations of centerline velocity and temperature in the plasma jet.

Critical Reynolds Number

The investigation was completed by calculating and analyzing bulk jet Reynolds numbers in an attempt to establish critical values for distinguishing plasma operating modes. The values obtained were compared to previously reported critical values in free plasma jets.

It was noted earlier that Incropera (31) determined critical Reynolds numbers for the operating regimes in a free

plasma jet. The Reynolds number Re was based on bulk jet properties at the temperature obtained by making an overall energy balance on the plasma generator. The reported conditions under which each regime occurs are:

1.	Laminar	$Re < 110$ to 250
2.	Transitional	110 to 250 $< Re <$ 300 to 800
3.	Turbulent	$Re >$ 300 to 800

Likewise, Cabannes (12) observed the turbulent operating regime to occur in a free plasma jet at a bulk Reynolds number of 500. For the experimental conditions employed in the measurements of voltage-current fluctuations, detailed velocities, and the effects of power during this investigation, bulk Reynolds numbers were calculated for each observation of a particular operating mode. The bulk Reynolds number is given by

$$Re = \frac{4m}{\pi D \mu} \quad , \qquad (7\text{-}5)$$

where m = mass flow rate of argon

D = diameter of the anode (1.031 cm)

μ = viscosity of argon at the bulk temperature

The bulk temperature of the jet was determined from the bulk

enthalpy of the jet, which in turn, was obtained from the net electrical energy to the argon.

Results The results of the calculations are presented in Table VII. Reynolds numbers are indicated for each mode and are grouped according to the phase of the investigation in which they were observed. The power level at which the Reynolds number was obtained is also shown using a general classification of low, intermediate, or high. It can be seen that the values for the laminar jets are below 160; the values for the transitional jets are in the range 170 to 210; and the values for the turbulent jets are above 240. Thus, for this particular plasma generator, the critical bulk Reynolds number for the transition from the laminar to transitional operating mode is between 160 and 170, while the critical bulk Reynolds number for the transition from the transitional mode to the turbulent mode is between 210 and 240.

Comparing these results to those obtained for a free plasma jet, it can be seen that the values of the bulk Reynolds number for the laminar and transitional modes cited in Table VII fall within the ranges given by Incropera. The values for the turbulent mode in Table VII generally fall slightly below the least critical value indicated by Incropera, and significantly below that given by Cabannes. It should be noted that

Table VII

Bulk Reynolds Numbers

Power Level	Operating Mode		
	Laminar	Transitional	Turbulent
1. Voltage-Current Fluctuations			
Low	-	183	259
Intermediate	73	188	352
Intermediate	126	174	289
High	103	-	294
2. Detailed Velocity Study			
Intermediate	-	175	266
3. Effect of Power Runs			
Low	155	207	335
Intermediate	133	173	264
High	126	165	244

in the Incropera study, argon flow rate, arc current, and nozzle exit diameter were all varied while in this study, only the flow rate and arc current were varied.

8. SUMMARY AND CONCLUSIONS

The flow patterns in a confined argon plasma jet at atmospheric pressure were studied experimentally. The argon flow rate and the input power to the plasma generator were the independent variables whose effects were investigated. By proper adjustment of flow rate and power level, three distinct types of jet could be obtained. These jets were labeled laminar, transitional, and turbulent, and at a fixed power level they occurred in the above sequence with increasing argon flow rate. Stable operation in the laminar mode was difficult to maintain, while operation in the transitional and turbulent modes presented no problems.

With each type of jet, the plasma generator voltage exhibited a characteristic waveform. However, in passing from one operating mode to another, the change in the waveform was so gradual that exact transition points could not be isolated. To obtain a direct measurement of velocities in the plasma jet a trace gas technique was studied. An attempt was made to spectrographically measure time delays as the trace gas passed from one position to another in the jet. Krypton was found to be a suitable trace gas, but while passage of the krypton through the plasma could be

detected spectrographically, the output signals were of such low magnitude that inherent random noise prevented resolution of the data into meaningful information.

The thermal condition of the plasma was analyzed by measuring temperatures corresponding to several excitation states and the electron temperature. It was found that the plasma was in local thermodynamic equilibrium and that the electron temperature obtained by observing the continuum intensity at 5330 $\mathring{A}$ could be used as the plasma temperature. The maximum uncertainty in the plasma temperature was estimated to be $\pm$ 1.7%.

Detailed sets of velocity profiles were determined for the transitional and turbulent plasma jets at an intermediate power level. Velocity profiles were calculated from the temperature profiles which were obtained spectrographically and the impact pressure profiles which were measured with a water-cooled probe. To relate the impact pressure measured with the cool probe to the plasma velocity, a model was developed which considered both viscous and heat transfer effects. The resulting relationship is

$$P_o - P_\infty = \frac{\rho_\infty U^2}{2} + \frac{\rho_\infty U^4}{8\gamma P_\infty} + \frac{2\bar{\mu} U}{R\left(1 + \frac{0.5576}{\sqrt{Re}}\right)} \quad , \qquad (8\text{-}1)$$

where P_o is the measured impact pressure, P_∞ is free stream pressure, U is the free stream plasma velocity, and R is

the radius of the probe. In the above equation physical properties in the Bernoulli and compressibility terms are evaluated at the free stream temperature, while those in the viscous term are evaluated at the temperature corresponding to the arithmetic mean of the wall and free stream enthalpies. The model was extended to calculate stagnation point heat transfer coefficients, and the theoretical values agreed quite well with experimental values obtained during an earlier study. Velocity profiles were also determined in cold flow from measured profiles of impact pressure.

The velocity, temperature, and impact pressure profiles for the plasma jets were found to be asymmetric while the corresponding cold flow profiles of velocity and impact pressure were symmetric. Generally, the velocities and temperatures were greater in the turbulent plasma jet than in the transitional jet at corresponding positions. Maximum temperatures and velocities decayed more rapidly with increasing downstream position in the transitional jet than in the turbulent jet. Centerline velocities were shown to vary linearly with centerline temperatures in both jets, which indicated that the primary reason for the velocity decay was the cooling of the jet and the associated density increase. Integration of the velocity profile nearest the plasma generator exit plane for both jets yielded mass flow rates which agreed closely with the metered

argon flow rates. The maximum uncertainty in the plasma velocities was estimated to be $\pm$ 8.4% in the transitional jet, and $\pm$ 7.1% in the turbulent jets.

The effect of input power level on the operation of the plasma generator was demonstrated. Variations in the generator voltage and the efficiency of energy transfer to the gas with arc current were indicated for each mode of operation. Centerline velocities again varied linearly with centerline temperatures in each of the three plasma jets, regardless of input power level. The centerline temperature at a fixed downstream position in a given jet was correlated with the net input energy per gram of argon, which could be calculated from the voltage-current and efficiency-current relationships for that jet.

Bulk Reynolds numbers were calculated for all of the various operating conditions. The values for the laminar plasma jets were below 160; those for the transitional jets were in the range of 170 to 210; the values for the turbulent jets were above 240.

APPENDIX A

Ambipolar Diffusion

Consider a system of charged particles (ions and electrons) moving together through neutral particles (atoms) in such a way that there is no net charge density and no net current flow at any point. Since the electrons have much greater mobilities than the ions, they tend to move much faster and leave a void of electrons. The tendency of ions and electrons to separate creates a self-induced electric field, which retards the flow of electrons and in effect, "pulls the ions" by increasing the ion mobility, so that there is no net current flow. In this development equilibrium of the ion-electron-atom system is assumed, and also, that only single ions and electrons comprise the charged particles.

For no net charge density

$$n_i = n_e \quad , \qquad \text{(A-1)}$$

so that the total number density of the system becomes

$$n = n_a + 2n_i \quad . \qquad \text{(A-2)}$$

In terms of mole fractions

$$1 = x_a + 2x_i \quad . \tag{A-3}$$

For no net current flow

$$\vec{g}_i z_i e + \vec{g}_e z_e e = 0 \quad , \tag{A-4}$$

which reduces

$$\vec{g}_i = \vec{g}_e \quad , \tag{A-5}$$

or

$$\frac{\vec{J}_i}{m_i} = \frac{\vec{J}_e}{m_e} \quad . \tag{A-6}$$

Also, by definition

$$\vec{J}_c = \vec{J}_i + \vec{J}_e \quad , \tag{A-7}$$

and since

$$\sum_k \vec{J}_k = 0 \quad , \tag{A-8}$$

then

$$\vec{J}_c = -\vec{J}_a \quad . \qquad \text{(A-9)}$$

Consider diffusion due only to a concentration gradient and the self-induced electric field. There is no externally applied force field. For any species j, the diffusion mass flux is (28):

$$\vec{J}_j = \frac{n^2}{e} \sum_k m_j m_k D_{jk} \vec{d}_k \quad , \qquad \text{(A-10)}$$

where

$$\vec{d}_k = \vec{\nabla} x_k - \frac{x_k}{kT} \left[\vec{F}_k - \frac{M_k}{M} \sum_i x_i \vec{F}_i \right] . \qquad \text{(A-11)}$$

The quantities d_k represent driving forces for diffusion. Diffusion due to a gradient in total pressure has been neglected, as has thermal diffusion. There are no externally applied body forces although the electric field noted above is included in the body force term. The diffusion driving force is then

$$\vec{d}_k = \vec{\nabla} x_k - \frac{x_k}{kT} \vec{E} e z_k \quad . \qquad \text{(A-12)}$$

since

$$\vec{F}_k = \vec{E} e z_k \quad . \qquad \text{(A-13)}$$

and

$$\sum x_k \vec{F}_k = 0 \quad . \qquad \text{(A-14)}$$

The diffusion flux for species j becomes

$$\vec{J}_j = \frac{n^2}{\rho} \sum_k m_j m_k D_{jk} \left[\vec{\nabla} x_k - \frac{x_k}{kT} \vec{E} e z_k \right] \quad . \qquad \text{(A-15)}$$

From equation (A-3)

$$\vec{\nabla} x_a = -2 \vec{\nabla} x_i \quad . \qquad \text{(A-16)}$$

Expanding equation (A-15) for j = i and j = e, and using equation (A-16)

$$\vec{J}_i = \frac{n^2}{\rho} m_i \left[(m_e D_{ie} - 2 m_a D_{ia}) \vec{\nabla} x_i + \frac{x_i \vec{E} e}{kT} (m_e D_{ie}) \right], \qquad \text{(A-17)}$$

and

$$\vec{J}_e = \frac{n^2}{\rho} m_e \left[m_a (D_{ei} - 2 D_{ea}) \vec{\nabla} x_i - \frac{x_i \vec{E} e}{kT} (m_a D_{ei}) \right] . \qquad \text{(A-18)}$$

In equation (A-18) m_i was replaced by m_a. To eliminate $\frac{x_i \vec{E}e}{kT}$, recall that there is no net current flow, so that

$$\frac{\vec{J}_i}{m_i} = \frac{\vec{J}_e}{m_e} \quad . \qquad \text{(A-6)}$$

Thus, equation (A-17) and (A-18) are combined and rearranged to yield

$$\frac{x_i \vec{E}e}{kT} = \frac{[m_a(D_{ei} - 2D_{ea} + 2D_{ia}) - m_e D_{ie}] \vec{\nabla} x_i}{m_e D_{ie} + m_a D_{ei}} \quad . \qquad \text{(A-19)}$$

It can be assumed that $D_{ei} \approx D_{ea}$ (18), and if terms multiplied by m_e are neglected in comparison with those multiplied by m_a, equation (A-19) can be simplified to obtain

$$\frac{x_i \vec{E}e}{kT} = \left(\frac{2D_{ia}}{D_{ea}} - 1\right) \vec{\nabla} x_i \quad . \qquad \text{(A-20)}$$

Using equation (A-20), equation (A-17) becomes

$$\vec{J}_i = -\frac{n^2 m_i m_a}{\rho} (2D_{ia}) \vec{\nabla} x_i \left[1 - \frac{m_e D_{ie}}{m_a D_{ei}}\right] \quad . \qquad \text{(A-21)}$$

Again neglecting the term multiplied by m_e, J_i can be written

$$\vec{J}_i = -\frac{n^2 m_i m_a}{\rho} (2D_{ia}) \vec{\nabla} x_i \quad . \qquad \text{(A-22)}$$

Likewise, equation (A-20) is used with equation (A-18) to give

$$\vec{J}_e = \frac{n^2 m_e m_a}{\rho}\left[2(D_{ei} - D_{ea}) - 2D_{ia}\right]\vec{\nabla}x_i \quad . \qquad \text{(A-23)}$$

Since $D_{ei} \approx D_{ea}$,

$$\vec{J}_e = -\frac{n^2 m_e m_a}{\rho}(2D_{ia})\vec{\nabla}x_i \quad . \qquad \text{(A-24)}$$

Substituting the expressions in equations (A-22) and (A-24) into equation (A-9) and noting that

$$m_a = m_i + m_e \quad , \qquad \text{(A-25)}$$

yields

$$\vec{J}_a = \frac{n^2 m_a^2}{\rho}(2D_{ia})\vec{\nabla}x_i \quad . \qquad \text{(A-26)}$$

Assuming the system of ions-electrons-atoms behaves as an ideal gas,

$$P = (n_a + n_i + n_e)kT \quad . \qquad \text{(A-27)}$$

Also,

$$\rho = n_a m_a + n_i m_i + n_e m_e \quad . \qquad \text{(A-28)}$$

Then

$$\rho = \frac{P m_a}{kT(1+\alpha)} \quad , \tag{A-29}$$

and

$$\frac{n^2 m_a}{\rho} = \frac{P(1+\alpha)}{kT} \quad , \tag{A-30}$$

where by definition

$$\alpha \equiv \frac{n_i}{n_i + n_a} \quad . \tag{A-31}$$

In terms of the mole fraction of ions or electrons, x_i,

$$\alpha = \frac{x_i}{x_i + x_a} \quad . \tag{A-32}$$

The reciprocal relationship is

$$x_i = \frac{\alpha}{1+\alpha} \quad . \tag{A-33}$$

Using equation (A-30), the desired diffusion fluxes become

$$\vec{J}_i = -\frac{P(1+\alpha)m_i}{kT}(2D_{ia})\vec{\nabla}x_i \quad , \tag{A-34}$$

$$\vec{J}_e = -\frac{P(1+\alpha)m_e}{kT}(2D_{ia})\vec{\nabla}x_i \quad , \qquad \text{(A-35)}$$

and

$$\vec{J}_a = \frac{P(1+\alpha)m_a}{kT}(2D_{ia})\vec{\nabla}x_i \quad . \qquad \text{(A-36)}$$

APPENDIX B

Line and Continuum Emission Coefficients

The emission coefficient for a spectral line given by equation (4-82) is

$$\varepsilon_{line} = \frac{hc}{4\pi\lambda} \frac{g_u A_{ul}}{Z_a} n_a e^{\frac{-E_u}{kT}} \quad . \qquad \text{(B-1)}$$

Table VIII below gives the characteristic constants for the lines observed during this investigation. The values presented were taken from Adcock and Plumtree (1) who summarize the various determinations of argon transition probabilities. Although for many lines, the values of the transition probabilities found by different investigators vary by as much as a factor of 2, the values of Gericke (23) are considered to be the most consistently reliable and are the ones listed below.

Table VIII

Spectral Line Constants

Line	g_u	A_{ul}	$\frac{g_u A_{ul}}{\lambda}$	E_u
$\overset{o}{A}$		$10^5 sec^{-1}$	$10^2 (sec\text{-}\overset{o}{A})^{-1}$	ev
4158.6	5	11.0	13.226	14.53
4181.9	3	4.58	3.286	14.68
4259.4	1	36.0	8.452	14.73
4300.1	5	3.4	3.953	14.50
4510.7	1	10.2	2.261	14.57

Using the constants in Table VIII and the tabulated values of n_a and Z_a as a function of temperature at 1 atmosphere which were prepared by Drellishak et al. (20), the temperature variation of $_{\text{line}}$ was calculated and is shown in Figure 40 for the five lines of interest.

The continuum emission coefficient for argon given by equation (4-84) is

$$\epsilon_\lambda = \frac{73.6c\pi^2e^6}{(6\pi m_e)^{\frac{3}{2}}} \frac{n_e^2}{\lambda^2(kT)^{\frac{1}{2}}} \quad . \qquad \text{(B-2)}$$

For a wavelength of 5330 Å, the tabulated values of n_e cited above were used to calculate the temperature dependency of ϵ_λ which is shown in Figure 41.

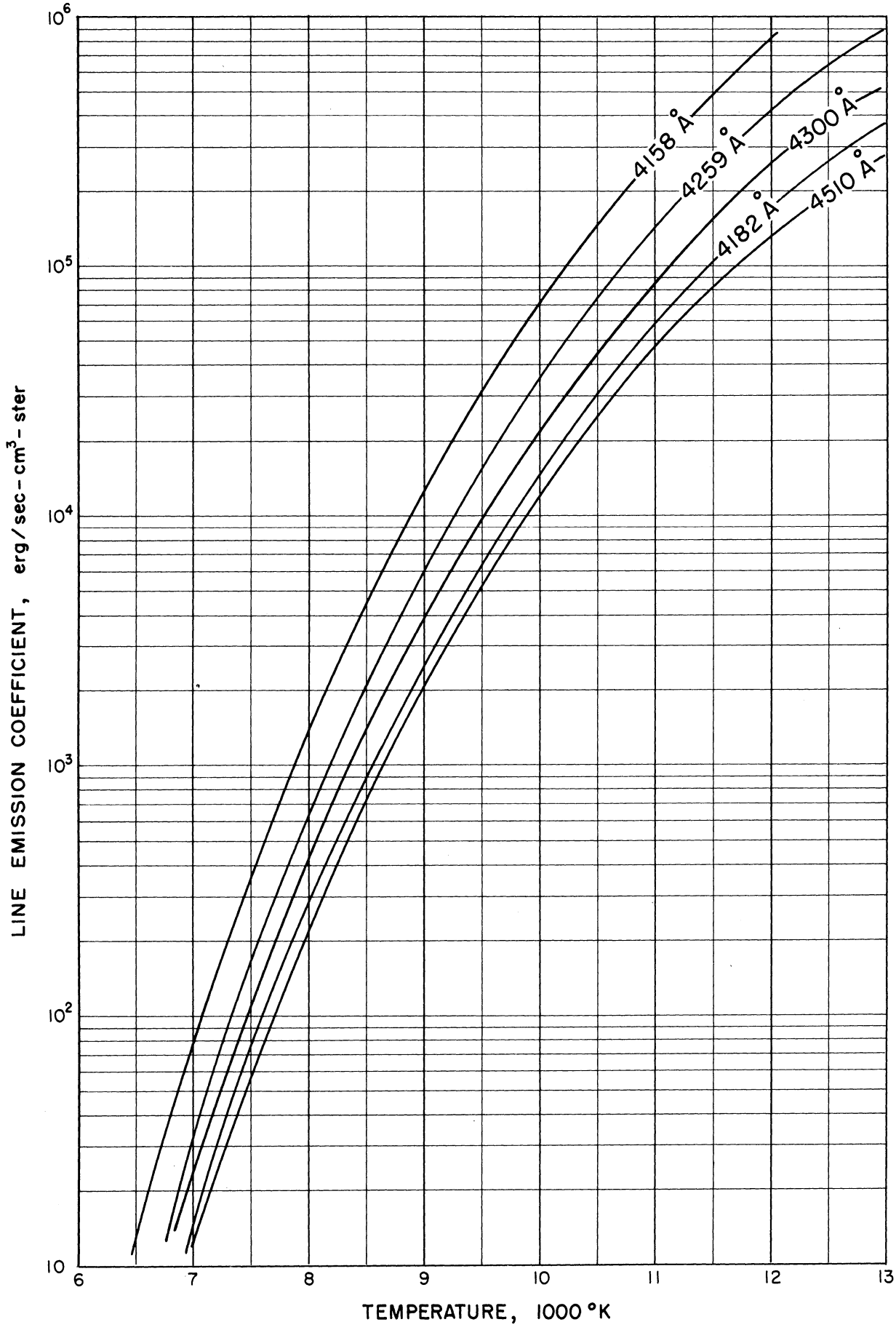

FIG. 40. EMISSION COEFFICIENTS FOR VARIOUS ARGON LINES AS A FUNCTION OF TEMPERATURE

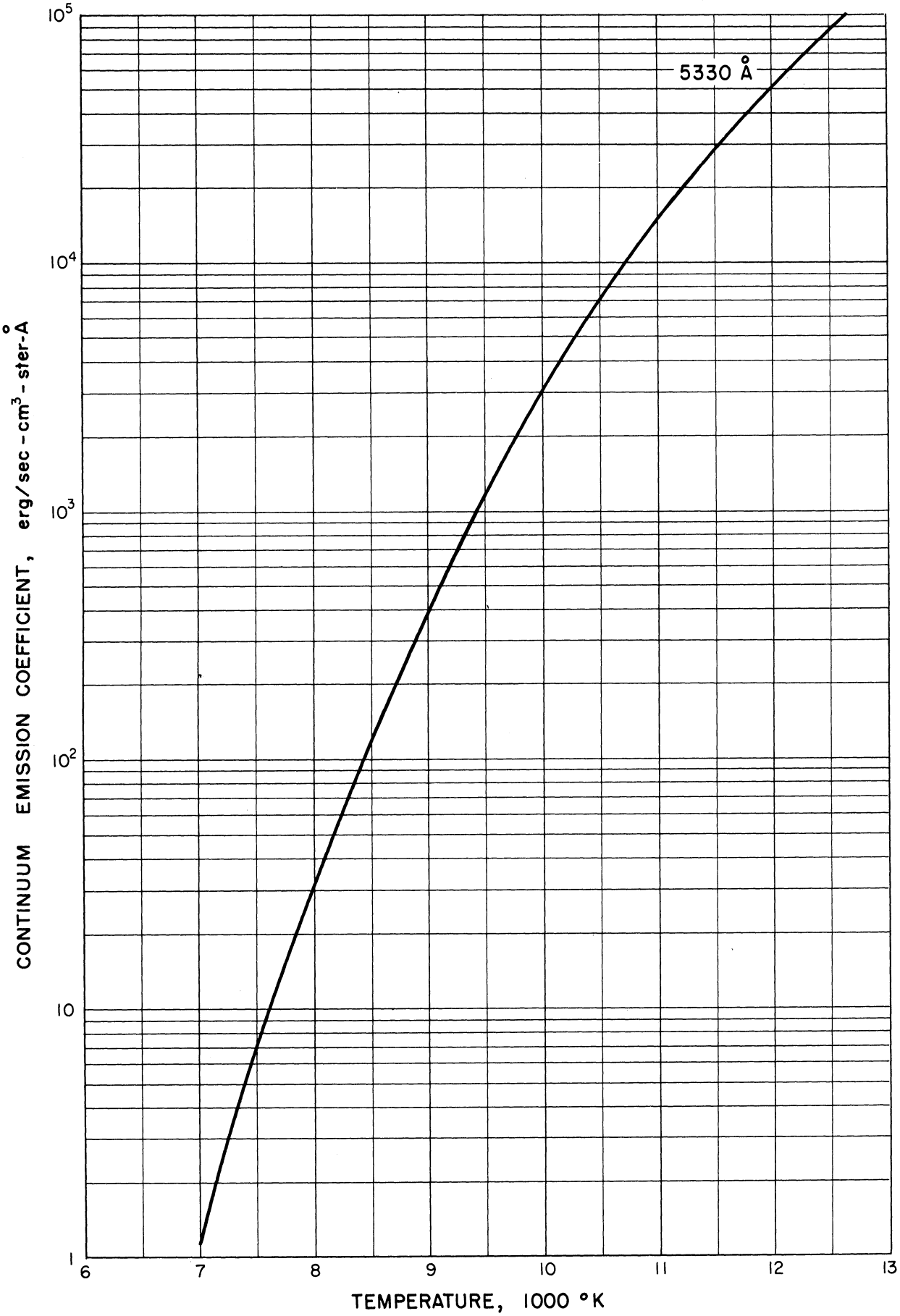

FIG. 41. CONTINUUM EMISSION COEFFICIENT OF ARGON AT 5330 Å AS A FUNCTION OF TEMPERATURE

APPENDIX C

Abel Inversion Technique

The Abel inversion arises whenever data obtained in integral form along a chord segment through an axis-symmetric medium must be resolved into the true radial distribution. The inversion in the case of plasma radiation is expressed analytically by equations (4-97) and (4-98):

$$\epsilon_\lambda(r,z) = -\frac{1}{\pi}\int_r^R \frac{\left(\frac{dI_\lambda}{dx}\right)dx}{(x^2-r^2)^{\frac{1}{2}}} \quad , \tag{C-1}$$

and

$$\epsilon_{line}(r,z) = -\frac{1}{\pi}\int_r^R \frac{\left(\frac{dI_{line}}{dx}\right)dx}{(x^2-r^2)^{\frac{1}{2}}} \quad . \tag{C-2}$$

As noted in Chapter 4, I_λ and I_{line} are obtained as numerical data so that it is somewhat more convenient to use a numerical technique to perform the inversion. The method used for this investigation is that of Barr (4).

Since I_{line} and I_λ are sets of numerical data, it is advantageous to reverse the order of differentiation and integration in equations (C-1) and (C-2) if the functions

are well behaved. This would smooth the data before differentiation and reduce amplification of noise in the data. If the functions are well behaved, equation (C-2) can be written

$$\mathcal{E}_{line}(r,z) = -\frac{1}{2\pi r}\frac{dF(r,z)}{dr} \quad , \qquad (C\text{-}3)$$

where

$$F(r,z) = 2\int_{r}^{R}\frac{I_{line}(x,z)\,x\,dx}{(x^2-r^2)^{\frac{1}{2}}} \quad . \qquad (C\text{-}4)$$

The x axis and hence r is divided into N equal increments Δ , so that

$$x_n = n\Delta \quad , \qquad (C\text{-}5)$$

and

$$r_k = k\Delta \quad , \qquad (C\text{-}6)$$

where

$$\Delta = \frac{R}{N} \quad , \qquad (C\text{-}7)$$

and n and k are integers between and including 0 and N.

In each interval $I_{line}(x,z)$ is approximated by

$$I_{line}(x,z) = a_n + b_n x^2 \quad . \tag{C-8}$$

The coefficients a_n and b_n are determined by requiring that

$$I_{line}(x_n,z) = I_{line}(n,z) \quad , \tag{C-9}$$

and

$$I_{line}(x_{n+1},z) = I_{line}(n+1,z) \quad , \tag{C-10}$$

where $I_{line}(n,z)$ and $I_{line}(n+1,z)$ are the measured numerical values at x_n and x_{n+1} respectively. For

$$r = r_k \quad , \tag{C-11}$$

equation (C-4) can then be written

$$F(k,z) = \frac{R}{N} \sum_{n=k}^{N} \alpha_{kn} I_{line}(n,z) \quad , \tag{C-12}$$

where α_{kn} are positive, slowly varying functions of k and n only. The F(k,z) are relatively insensitive to small errors

in the I_{line} (n,z). In order to perform the differentiation of equation (C-3) a polynomial is fit to each section of the F(k,z) vs. k curve. This process also smoothes the data. Thus, the F(k,z) are represented by

$$F(k,z) = (A_k + B_k k^2 + C_k k^4)\frac{R}{N} \quad . \qquad \text{(C-13)}$$

Equation (C-3) then takes the form

$$\varepsilon_{line}(k,z) = \frac{-N}{2R^2 k}\frac{dF(k,z)}{dk} \quad , \qquad \text{(C-14)}$$

and a least squares technique is used to determine the coefficients. As a result, a new set of coefficients β_{kn} is obtained such that

$$\varepsilon_{line}(k,z) = \frac{N}{\pi R}\sum_{n=k-2}^{N}\beta_{kn} I_{line}(n,z) \quad , \qquad \text{(C-15)}$$

for k > 2, and

$$\varepsilon_{line}(k,z) = \frac{N}{\pi R}\sum_{n=0}^{N}\beta_{kn} I_{line}(n,z) \quad , \qquad \text{(C-16)}$$

for k ≤ 2.

The complete sequence of steps - integration, least squares fit, and differentiation - is included in the β_{kn}, which have been evaluated and tabulated by Barr for N up to 20.

With this table, any number of zones from 2 to 20 can be employed in performing the inversion. Since the data are smoothed automatically, they need not be plotted prior to calculation. The smoothing is achieved at a point where it can be done most efficiently - after integration but before differentiation.

To test the effect of the number of zones on the accuracy of the inversion, a sample analytic distribution for $\varepsilon_{line}(r,z)$ was assumed and an analytic relationship for $I_{line}(x,z)$ determined. Discrete values of $I_{line}(n,z)$ were then calculated and used to evaluate the $\varepsilon_{line}(k,z)$ profile by means of the numerical method. The numerical values $\varepsilon_{line}(k,z)$ are compared with those computed from the analytic function $\varepsilon_{line}(r,z)$ in Table IX for 5, 10, 15, and 20 zone inversions. The assumed analytic distribution was

$$\varepsilon_{line}(r,z) = 1 - 4r^2 \quad , \qquad \text{(C-17)}$$

for which the analytic chord distribution is

$$I_{line}(x,z) = \frac{16}{3}\left(\frac{1}{4} - x^2\right)^{\frac{3}{2}} \quad . \qquad \text{(C-18)}$$

It can be seen that for 10 zone inversions and greater, agreement between analytical and numerical values is excellent at all radial positions except the last.

Table IX

Accuracy Test for Abel Inversion Technique

$\varepsilon_{line}(r,z)$

r	Analytical	5 Zone	10 Zone	15 Zone	20 Zone
0.0	1.000	0.994	1.000	1.000	1.000
0.1	0.960	0.954	0.959	0.958	0.960
0.2	0.840	0.835	0.839	0.840	0.841
0.3	0.640	0.637	0.639	0.639	0.640
0.4	0.360	0.390	0.361	0.360	0.360
0.5	0.000	0.172	0.092	0.062	0.047

APPENDIX D

Spectrograph Calibration

The spectrographic system was calibrated by observing a standard radiation source whose specific intensity could be calculated. The recorded output was compared with the source intensity at 5330 Å, and the integrated output was compared with the integrated source intensity for certain wavelength intervals corresponding to the widths of specific argon lines. From these comparisons the characteristic spectral response of the overall system could be obtained.

A ribbon filament tungsten lamp normally employed as a microscope illuminator was used as the radiation source. This lamp is a 6 volt, 108 watt unit, with power supplied by a 6 volt transformer used in series with a Variac. The lamp was located so that the tungsten filament occupied the same position in the optical system as the plasma jet. In this way its rays followed the same optical path as those from the plasma jet and the solid angle subtended by the slit of the spectrograph was the same for each source.

The apparent temperature of the emitting tungsten filament was measured with a calibrated, disappearing-filament optical pyrometer. The apparent temperature is the temperature of a black body whose specific intensity at a given wavelength is the

same as that of the luminous tungsten ribbon. It is related to the true emitting temperature by

$$B_\lambda(T_{obs}) = \tau_\lambda \epsilon_\lambda(T_{true}) B_\lambda(T_{true}) \quad , \qquad \text{(D-1)}$$

where τ_λ = transmittance of the lamp glass envelope at wavelength λ

$\epsilon_\lambda(T)$ = spectral emissivity of tungsten at wavelength λ and temperature T

$B_\lambda(T)$ = Planck function for black-body radiation at wavelength λ and temperature T

T_{obs} = apparent temperature measured by pyrometer

T_{true} = true ribbon temperature .

The filter in the pyrometer is such that the ribbon is observed in a narrow band around 6500 Å. The transmittance of a typical bulb is 0.92 (9). Equation (D-1) can therefore be simplified to

$$T_{true} = \frac{22135}{\ln\left[1 + 0.92\epsilon\left(e^{\frac{22135}{T_{true}}} - 1\right)\right]} \quad , \qquad \text{(D-2)}$$

where ϵ is the tungsten emissivity at 6500 Å and T_{true}. The tungsten emissivity as a function of temperature and wavelength has been evaluated by DeVos (16). Using this evaluation, T_{true} was calculated as a function of T_{obs} and is shown in Figure 42.

With the true temperature known, the specific intensity of the radiation emitted by the tungsten filament can be calculated

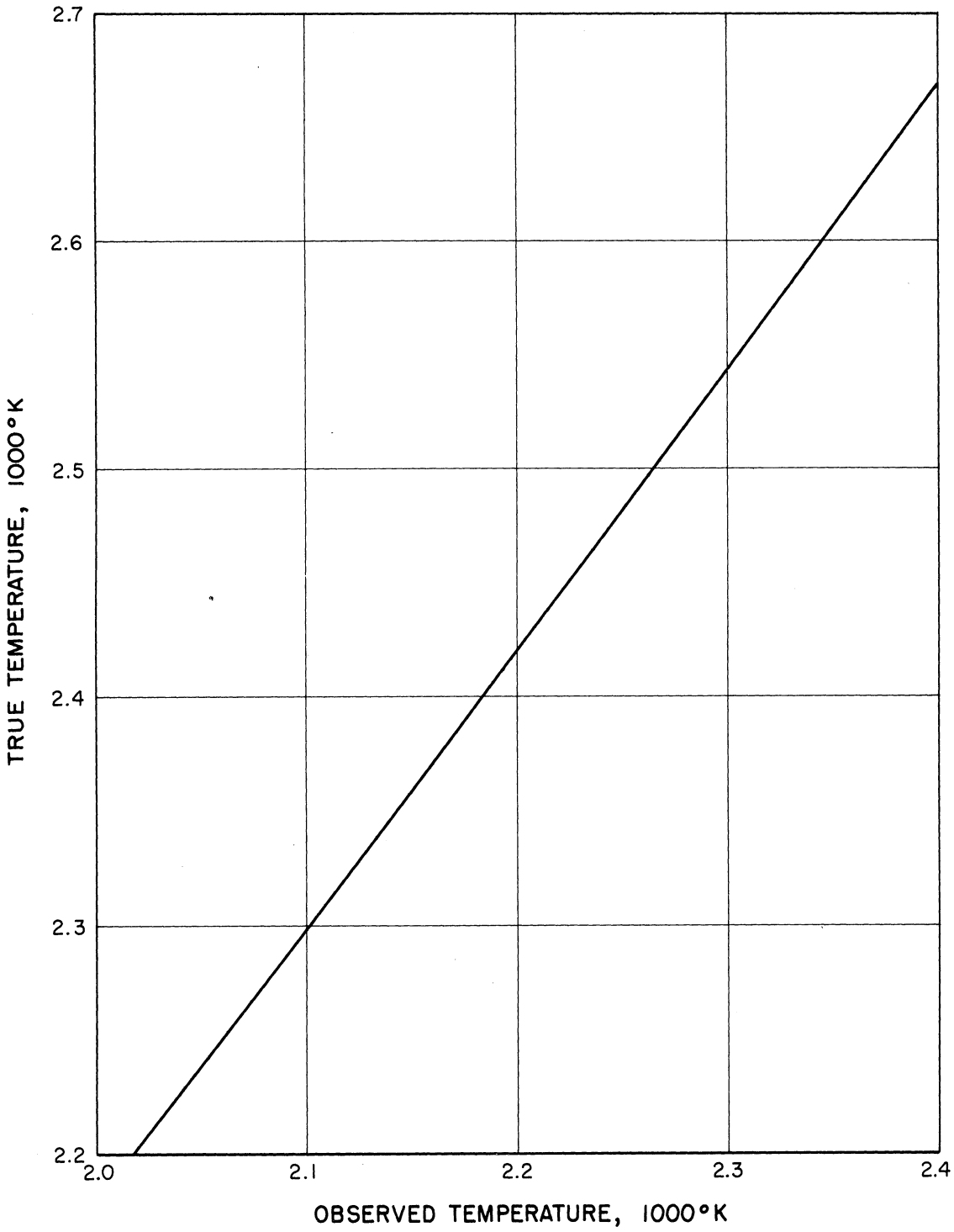

FIG. 42. TRUE TUNGSTEN FILAMENT EMISSION TEMPERATURE AS A FUNCTION OF THE APPARENT TEMPERATURE OBSERVED WITH AN OPTICAL PYROMETER

from the Planck function and the tungsten emissivity, and thus

$$I_\lambda = 0.92\,\epsilon_\lambda(T)\left[\frac{2hc^2}{\lambda^5\left(e^{\frac{hc}{\lambda kT}}-1\right)}\right] \quad . \qquad \text{(D-3)}$$

The photomultiplier current depends on the total power of the radiation seen by the tube. For this type of behavior, the photomultiplier current i_λ is related to the source intensity I_λ at any wavelength λ by

$$i_\lambda = s(\lambda) I_\lambda \quad , \qquad \text{(D-4)}$$

in which $s(\lambda)$ is the overall sensitivity of the complete optical system at wavelength λ .

The overall sensitivity $s(\lambda)$ includes the effects of the transmittance of the scanning and consensing system, the efficiency of the grating, and the actual photomultiplier tube response, and varies only with wavelength as long as the entrance slit is maintained at constant height and width and the photomultiplier tube is operated at a constant voltage. For convenience, the characteristic spectral response $S(\lambda)$ is defined as the inverse of $s(\lambda)$, so that equation (D-4) becomes

$$I_\lambda = i_\lambda S(\lambda) \quad . \qquad \text{(D-5)}$$

If the signal is to be recorded, $S(\lambda)$ can be determined at a given wavelength from the chart deflection incurred in observing the standard source, since

$$i_\lambda = \frac{(\%\ \text{Deflection})(\text{Range})}{R_{sig} \times 10^2} \quad , \qquad \text{(D-6)}$$

and I_λ is calculated from equation (D-3). In equation (D-6) the range is that of the microvolt amplifier and R_{sig} is the resistance of the variable resistance box. The measured chart deflection must be corrected for the contribution of the photomultiplier dark current.

If the signal is to be integrated, equation (D-5) must be integrated. Therefore

$$\int I_\lambda d\lambda = S(L) \int i_\lambda d\lambda \quad , \qquad \text{(D-7)}$$

where S(L) is the characteristic spectral response over the integration range. In practice, the amplified photomultiplier voltage V_λ is integrated with respect to time as the spectrum of the source is scanned, so that

$$\int i_\lambda d\lambda = \frac{(\text{Range})(\text{Scan})}{R_{sig}} \int V_\lambda dt \quad , \qquad \text{(D-8)}$$

where Scan is the wavelength scanning rate. The integrator output V_{out} is given by

$$V_{out} = \frac{1}{t_c} \int V_\lambda \, dt \quad , \qquad \text{(D-9)}$$

in which t_c is the integrator time constant, obtained by integrating a standard constant voltage for a specified time interval. Equation (D-7) can then be written

$$\int I_\lambda \, d\lambda = S(L) \left[\frac{t_c(\text{Range})(\text{Scan})}{R_{sig}} \right] V_{out} \, . \qquad \text{(D-10)}$$

Thus S(L) can be determined if a segment of the spectrum emitted by the tungsten lamp is scanned while the photomultiplier output is integrated. The integration of I_λ given by equation (D-3) is done numerically. No correction for the photomultiplier dark current is required, since its contribution can be subtracted from the signal V_λ before integration.

During the calibration to determine $S(\lambda)$ and S(L), the Variac in the lamp power supply system was adjusted so that the tungsten filament was emitting at a true temperature of 2600 ^{o}K. The temperature was uniform over the central portion of the filament and the image of this portion when focused on the spectrograph slit was much greater in area than the slit itself.

In this way radiation of known constant intensity at wavelength was imposed on the grating of the spectrograph. The characteristic spectral response for the wavelength and wavelength intervals of interest are listed in Table X. Both $S(\lambda)$ and S(L) have units of erg/cm^2-sec-ster-$\mathring{A}$-amp.

Table X

Characteristic Spectral Response
of the Spectrographic System

Wavelength or Range $\mathring{A}$	Characteristic Spectral Response $ergs/cm^2\text{-}sec\text{-}ster\text{-}\mathring{A}\text{-}amp$
4153-4163	3.506×10^{11}
4179-4187	3.402×10^{11}
4256-4264	3.408×10^{11}
4297-4305	3.490×10^{11}
4507-4516	3.652×10^{11}
5330	5.450×10^{11}

APPENDIX E

Probe Calibration

The water-cooled probe - pressure transducer - millivolt recorder system was calibrated with a water manometer. Known pressures were sensed by the probe to obtain the corresponding recorder chart deflection. The pressure source was the free-stream pressure in an air stream, which was monitored with both the probe and the manometer. Pressures in the range of 0.00 to 0.25 psig were generated in this manner. The span of the recorder was adjusted so that 100% chart deflection corresponded to 7.5 millivolts output from the transducer (approximately 0.22 psig). Differences in height in each leg of the water manometer were measured with a cathetometer. Calibration points were obtained for both increasing and decreasing pressure, to insure that no hysteresis effect was involved. The response of the system with pressure was linear. The calibration curve is shown in Figure 43.

The time response of the probe-transducer-recorder system was measured by locating the probe tip at a point maximum impact pressure in a jet of air, and then imposing a step change in pressure by turning off the air flow with a check valve. The response of the system was essentially logarithmic,

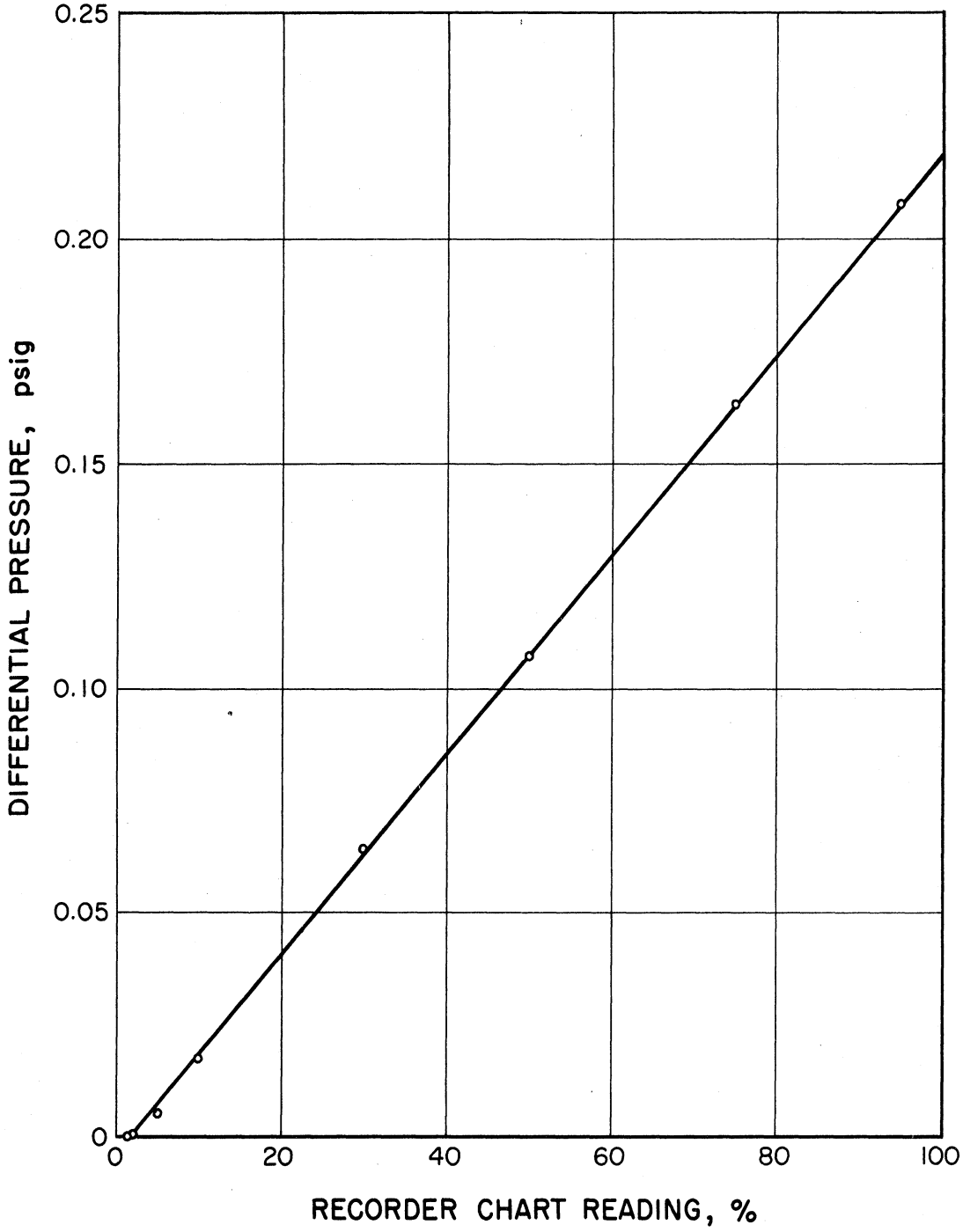

FIG. 43. CALIBRATION CURVE OF THE PROBE-PRESSURE TRANSDUCER SYSTEM

with the steady state value being approached asymtotically. For such a system the time constant is the time required for the response to achieve 63.2% of the steady state value (13). Several determinations were made, and the average value was found to be 0.25 sec.

NOMENCLATURE

Symbol	
a	radius of curvature of a body in a potential flow field - cm
A_{ul}	Einstein transition probability - sec^{-1}
B	Planck function for blackbody radiation - $erg/cm^2\text{-}sec\text{-}ster\text{-}\mathring{A}$
c	weight fraction
c	speed of light - cm/sec
C_p	specific heat capacity at constant pressure - $cal/gm\text{-}^oK$
C_{pr}	reactive heat capacity at constant pressure - $cal/gm\text{-}^oK$
C_v	specific heat at capacity at constant volume - $cal/gm\text{-}^oK$
c_1	a constant (see equation (7-1)) - $gm/cm^2\text{-}sec$
c_2	a constant (see equation (7-2)) - $gm/cm^3\text{-}^oK$
C_1	a constant (see equation (4-84)) - $erg\text{-}\mathring{A}/ster$
C_2	a constant (see equation (4-85)) - $erg\text{-}\mathring{A}/cm^3\text{-}ster$
Com	contribution of the compressibility term in equation (4-33) to the measured impact pressure - %
$\vec{d}$	driving force for diffusion (defined in equation (A-11)) - cm^{-1}
D	diameter of anode nozzle - cm
D_{jk}	multicomponent diffusion coefficient ($D_{jj} \equiv 0$) - cm^2/sec
e	electron charge unit - esu
E	energy - erg
$\vec{E}$	electric field strength - $gm\text{-}cm/sec^2\text{-}esu$

Symbol	
$f(T)$	unspecified function of temperature
$\vec{F}$	body force - $gm\text{-}cm/sec^2$
g	statistical weight
$\bar{g}$	quantuum mechanical correction factor
$\vec{g}$	number diffusion flux - $cm^{-2}sec^{-1}$
h	specific enthalpy - cal/gm
h	heat transfer coefficient - $Btu/hr\text{-}ft^2\text{-}^oF$
h	Planck's constant - erg-sec
Δh	heat of reaction - cal
i_λ	multiplier phototube current - amp
I	ionization energy - cal
I_λ	specific intensity of radiation - $erg/cm^2\text{-}sec\text{-}ster\text{-}\mathring{A}$
I_{line}	integrated line intensity - (defined in equation (4-95)) - $erg/cm^2\text{-}sec\text{-}ster$
J	component of the mass diffusion flux parallel to the stagnation streamline - $gm/cm^2\text{-}sec$
$\vec{J}$	mass diffusion flux - $gm/cm^2\text{-}sec$
k	counting index
k	Boltzmann's constant - $cal/^oK$
K_p	equilibrium constant based on activities for a system at constant pressure.
K	thermal conductivity - $cal/sec\text{-}cm\text{-}^oK$
K_r	reactive thermal conductivity at constant pressure - $cal/sec\text{-}cm\text{-}^oK$
l	length in the direction of observation thru a radiation source - cm

Symbol

L	vertical distance above plasma generator exit plane - cm
m	particle mass - gm
m	mass flow rate of argon - gm/min
M	Mach number
M	molecular weight - gm/gmol
n	number density - cm^{-3}
n	counting index
N	number of Abel inversion zones
P	pressure - psia
ΔP	pressure difference - psi
r	counting index
r	coordinate normal to the stagnation streamline - cm
r	radial coordinate in a radiation source - cm
R	radius of curvature of a spherical half body - cm
R	radius of the radiation source - cm
R	radius of the anode nozzle - cm
R_{sig}	resistance - ohms
Re	Reynolds number
s	sensitivity of optical system - amp-cm^2-sec-ster-Å/erg
S	characteristic spectral response - erg/cm^2-sec-ster-Å-amp
t	time - sec
t_c	time constant of integrator - sec
T	temperature - ^oK

Symbol	
u	component of velocity parallel to the stagnation streamline - cm/sec
U	axial component of the free stream velocity - cm/sec
U_B	Bernoulli velocity - cm/sec
v	component of velocity normal to the stagnation streamline - cm/sec
V	output signal of the microvolt amplifier - volt
Vis	contribution of the viscosity term in equation (4-33) to the measured impact pressure - %
x	mole fraction
x	coordinate normal to the direction of observation of the radiation source (chord coordinate) - cm
y	coordinate parallel to the direction of observation of the radiation source - cm
z	coordinate parallel to the stagnation streamline - cm
z	effective average charge (defined in equation (4-84))
z	coordinate parallel to the axis of the plasma jet (vertical coordinate) - cm
z	number charge (+1 for ion, -1 for electron, 0 for atom)
Z	internal partition function
α	fraction of argon which is ionized
β	defined in equation (4-27)
β_{kn}	numerical constants in the Abel inversion
γ	ratio of specific heats
$-\delta$	position on the stagnation streamline at which the region of compressible, non-viscous flow meets the region of incompressible, viscous flow - cm

Symbol

δ^*	displacement thickness (defined in equation (4-25)) - cm
ϵ_λ	volume emission coefficient of continuum radiation - erg/cm^3-sec-ster-Å
ϵ_λ	emissivity
$\mathcal{E}_\lambda$	spectral line emission profile - erg/cm^3-sec-ster-Å
$\mathcal{E}_{line}$	volume emission coefficient of a spectral line - erg/cm^3-sec-ster
λ	wavelength - Å
ν	viscosity - gm/cm-sec
ρ	mass density - gm/cm^3
γ	transmittance
Φ	potential function for inviscid flow

Subscripts

a	argon atom
c	all charged particles (ions + electrons)
e	electron
i	argon ion
i	counting index for vertical position
k	counting index in the Abel inversion
l	lower energy level
n	counting index in the Abel inversion
ref	reference value
u	upper energy level
0	stagnation conditions
$-\delta$	conditions at position $-\delta$

Subscripts

λ	wavelength
∞	free stream conditions

Superscripts

$-$	mean value
$*$	ideal (inviscid) flow
$*$	reference conditions

REFERENCES

1. Adcock, B. D. and W. E. G. Plumtree, "On Excitation Temperature Measurements in a Plasma Jet, and Transition Probabilities for Argon Lines," Journal of Quantitative Spectroscopy and Radiative Transfer, 4, January-February 1964, 29.

2. Aller, L. H., Astrophysis: The Atmospheres of the Sun and Stars, second edition, The Roland Press Company, New York, 1963.

3. Barker, Muriel, "On the Use of Very Small Pitot Tubes for Measuring Wind Velocity," Proceedings of the Royal Society, Series A, 101, August 1, 1922, 435.

4. Barr, W. L., "Method for Computing the Radial Distribution of Emitters in a Cylindrical Source," Journal of the Optical Society of America, 52, August 1962, 885.

5. Beasley, W. D., J. D. Brooks, and R. L. Barger, "Direct Velocity Measurements In Low-Density Plasma Flows," National Aeronautics and Space Administration Technical Note D-1783, May 1963.

6. Bocher, M., An Introduction to the Study of Integral Equations, Hafner Publishing Company, New York, 1960.

7. Bockasten, K., "Transformation of Observed Radiances into Radial Distribution of the Emission of a Plasma," Journal of the Optical Society of America, 51, September 1961, 943.

8. Bott, J. F., "Spectroscopic Measurement of Temperatures in an Argon Plasma Arc," Physics of Fluids, 9, August 1966, 1540.

9. Bowen, S. W., "A Spectroscopic Study of an Underexpanded Argon Plasma Jet," Ph.D. Thesis, University of Michigan, Ann Arbor, 1966.

10. Browning, J. A., "Techniques for Producing Plasma Jets," pp. 126-138 in Dynamics of Conducting Gases, Proceedings of the Third Biennial Gas Dynamics Symposium, ed. by A. B. Cambel and J. B. Fenn, Northwestern University Press, Evanston, Illinois, 1960.

11. Cabannes, F., J. Chapelle, M. Decroisette, and A. Sy, "Mesure De La Vitesse et De La Temperature Dans Un Jet Laminaire De Plasma D'Argon," Revue des Hautes Temperatures et des Refractures, 2, 1965, 297.

12. Cabannes, F., F. Joubert, and A. Sy, "Etude De Jets Laminares De Plasma D'Argon," Revue des Hautes Temperatures et des Refractures, 1, 1964, 107.

13. Ceaglske, N. H, Automatic Process Control for Chemical Engineers, John Wiley and Sons, New York, 1962.

14. Chambre, T. L., and H. R. Smith, "The Impact Tube in a Viscous Compressible Gas," University of California Engineering Projects Report HE-150-63, August 1949.

15. Chludzinski, G. R., "Energy Transfer to Solids in R. F. Generated Plasmas," Ph.D. Thesis, University of Michigan, Ann Arbor, 1964.

16. De Vos, J. C., "A New Determination of the Emissivity of Tungsten Ribbon," Physica, 20, October 1954, 714.

17. Devoto, R. S., "Transport Coefficients of Partially Ionized Argon," Physics of Fluids, 10, February 1967, 354.

18. Devoto, R. S., "Transport Properties of Ionized Monatomic Gases," Physics of Fluids, 9, June 1966, 1230.

19. Drawin, H.W., and P. Felenbok, Data for Plasmas in Local Thermodynamic Equilibrium, Gauthier-Villars, Paris, 1965.

20. Drellishak, K. S., C. F. Knopp, and A. B. Cambel, "Partition Functions and Thermodynamic Properties of Argon Plasmas," Arnold Engineering Development Center AEDC-TDR-63-146, August 1963.

21. Eckert, E. R. G., "Engineering Relations for Friction and Heat Transfer to Surfaces in High Velocity Flow," Journal of the Aeronautical Sciences, 22, August 1955, 585.

22. Freeman, M. P., S. V. Li, and W. Von Jaskowsky, "Velocity of Propagation and Nature of Luminosity Fluctuations in a Plasma Jet," Journal of Applied Physics, 33, September 1962, 2845.

23. Gericke, W. E., "Messung der Ubergangswahrscheinlichkeit sowie Halbwertsbreite und Verschiebung von AI-Linien in thermisch leuchtenden Plasmen," Zeitschrift fur Astrophysik, 53, July 25, 1961, 68.

24. Goldstein, S., editor, Modern Developments in Fluid Dynamics, vol. II, The Clarendon Press, Oxford, 1938.

25. Gottschlich, C. F., "Measurement of the Velocity Distribution in a Plasma Jet," AIAA Journal, 4, June 1966, 1086.

26. Grey, J., and P. F. Jacobs, "Turbulent Mixing in a Partially Ionized Gas," Princeton University Aeronautical Engineering Laboratory Report No. 625, October 1962.

27. Grey, J., P. F. Jacobs, and M. P. Sherman, "Calorimetric Probe for the Measurement of Extremely High Temperatures," Review of Scientific Instruments, 33, July 1962, 738.

28. Hirschfelder, J. O., C. F. Curtiss, and R. B. Bird, Molecular Theory of Gases and Liquids, John Wiley and Sons, New York, 1954.

29. Homann, F., "The Effect of High Viscosity on the Flow Around a Cylinder and Around a Sphere," National Advisory Committee for Aeronautics TM 1334, June 1952.

30. Hurd, C. W., K. P. Cheskey, and A. H. Shapiro, "Influence of Viscous Effects on Impact Tubes," Journal of Applied Mechanics, 20, June 1953, 253.

31. Incropera, F., and J. Leppert, "Flow Transition Phenomena in a Subsonic Plasma Jet," Stanford University TR 247-9, 1965.

32. John, R. R., and W. L. Bade, "Recent Advances in Electric Arc Plasma Generation Technology, ARS Journal, 31, January 1961, 4.

33. Jordan, G. R., and L. A. King, "The Nature of Fluctuations Present in D.C. Plasma Jets in Argon and Nitrogen," British Journal of Applied Physics, 16, 1965, 431.

34. Kasahara, E., A. Hasui, Y. Emori, and A. Iiyoshi, "Studies on Plasma Jet," Bulletin of the Japanese Society of Mechanical Engineers, 7, August 1964, 590.

35. Kays, W. M., Convective Heat and Mass Transfer, McGraw-Hill, New York, 1966.

36. Kimura, I., and A. Kanzawa, "Measurement of Stream Velocity in an Arc," AIAA Journal, 1, February 1963, 310.

37. Liepmann, H. W., and A. E. Puckett, Introduction to Aerodynamics of a Compressible Fluid, John Wiley and Sons, New York, 1947.

38. MacMillan, F. A., "Viscous Effects on Pitot Tubes at Low Speeds," Journal of the Royal Aeronautical Society, 58, August 1954, 570.

39. Meador, W. E., and L. D. Statton, "Electrical and Thermal Properties of Plasmas," Physics of Fluids, 8, September 1965, 1694.

40. Merrifield, S. E., and D. W. Esker, "Propagation Velocity of Random Light Fluctuations in Arc-Jet Exhausts," Journal of Spacecraft and Rockets, 3, October 1966, 1510.

41. Moskvin, Y. V., and N. N. Chesnokova, "A Spectroscopic Study of an Argon Jet at the Exit from a Plasmatron," Teplofizika Vysokikh Temperatur, 3, May-June 1965, 370.

42. Nestor, O. H., and H. N. Olsen, "Numerical Methods for Reducing Line and Surface Probe Data," SIAM Review, 2, July 1960, 200.

43. Quarderer, G. J., "Photochemical Chlorination of Sulfur Dioxide Utilizing a Plasma Light Source," Ph.D. Thesis, University of Michigan, Ann Arbor, 1967.

44. Reed, T. B., "Determination of Streaming Velocity and the Flow of Heat and Mass in High-Current Arcs," Journal of Applied Physics, 31, November 1960, 2048.

45. Sampson, D. H, Radiative Contributions to Energy and Momentum Transport in a Gas, Interscience Publishers, New York, 1965.

46. Schowalter, W. R., and G. E. Blaker, "On the Behavior of Impact Probes at Low Reynolds Numbers," Journal of Applied Mechanics, 28, March 1961, 136.

47. Sherman, F. S., "New Experiments on Impact-Pressure Interpretation in Supersonic and Subsonic Rarefied Air Streams," National Advisory Committee for Aeronautics TN 2995, September 1953.

48. Sherman, M. P., and J. Grey, "Calculation of Transport Properties for Mixtures of Helium and Partly - Ionized Argon," Princeton University Aeronautical Engineering Laboratory Report No. 673, December 1963.

49. Sherman, M. P., and J. Grey, "Interactions Between a Partly - Ionized Laminar Subsonic Jet and a Cool Stagnant Gas," Princeton University Aeronautical Engineering Laboratory Report No. 707, September 1964.

50. Sibulkin, M., "Heat Transfer Near the Forward Stagnation Point of a Body of Revolution," Journal of the Aeronautical Sciences, 19, August 1952, 570.

51. Skifstad, J. G., "Summary of Published Literature Concerned with Electric Arc Phenomena Pertinent to Plasma Jet Devices Purdue University Jet Propulsion Center Report TM-62-4, August 1962.

52. Smith, D. L., "Mass and Energy Transfer Between a Confined Plasma Jet and a Gaseous Coolant," Ph.D. Thesis, University of Michigan, Ann Arbor, 1965.

53. Sprengel, U., and G. Au, "Kalorimetrische Messungen von oertlichen Temperaturen und Geschwindigkeiten in einem Stickstoff-Plasmastrahl," Zeitschrift fur Flugwissenschaften, 14, April 1966, 188.

54. Streeter, V. L., editor, Handbook of Fluid Dynamics, McGraw-Hill, New York, 1961.

55. Whitman, A., and P. Barkan, "An Uncooled Rapid Response Probe for Measuring Stagnation Pressures in a High Velocity Arc Plasma," Aerospace Research Laboratories ARL 64-192, November 1964.